Terahertz quantum-cascade lasers for spectroscopic applications

vorgelegt von

M. Sc.

Benjamin Malte Röben

geb. in Berlin

von der Fakultät II — Mathematik und Naturwissenschaften

der Technischen Universität Berlin

zur Erlangung des akademischen Grades

Doktor der Naturwissenschaften

— Dr. rer. nat —

genehmigte Dissertation

Promotionsausschuss:

Vorsitzender: Prof. Dr. Michael Kneissl
Gutachterin: Prof. Dr. Ulrike Woggon
Gutachter: Prof. Dr. Holger T. Grahn
Gutachter: Prof. Dr. Manfred Helm

Tag der wissenschaftlichen Aussprache: 23. Juli 2018

Berlin 2018

Abstract

Terahertz (THz) quantum-cascade lasers (QCLs) are unipolar semiconductor heterostructure lasers that emit in the far-infrared spectral range. They are very attractive radiation sources for spectroscopy, since they are very compact and exhibit typical output powers of several mW as well as linewidths in the MHz to kHz range. This thesis presents the development of methods to tailor the emission characteristics of THz QCLs and employ them for spectroscopy with highest resolution and sensitivity. In many cases, these spectroscopic applications require that the far-field distribution of the THz QCLs exhibits only a single lobe. However, multiple lobes in the far-field distribution of THz QCLs were experimentally observed, which were unambiguously attributed to the typically employed mounting geometry and to the cryogenic operation environment such as the optical window. Based on these results, a method to obtain a single-lobed far-field distribution is demonstrated. A critical requirement to employ a THz QCL for high-resolution spectroscopy of a single absorption or emission line is the precise control of its emission frequency. This long-standing problem is solved by a newly developed technique relying on the mechanical polishing of the front facet. A QCL fabricated in this manner allows for spectroscopy at a maximal resolution in the MHz to kHz range, but its accessible bandwidth is usually limited to a few GHz. In contrast, a newly developed method to utilize QCLs as sources for THz Fourier transform spectrometers enables highly sensitive spectroscopy over a significantly larger bandwidth of at least 72 GHz with a maximal resolution of typically 100 MHz. The application of QCLs as sources for THz Fourier transform spectroscopy leads to a signal-to-noise ratio and dynamic range that is substantially increased by a factor of 10 to 100 as compared to conventional sources. The results presented in this thesis pave the way to routinely employ THz QCLs for spectroscopic applications in the near future.

Zusammenfassung

Terahertz-Quantenkaskadenlaser (THz-QCLs) sind unipolare Halbleiterheterostrukturlaser, die im ferninfraroten Spektralbereich emittieren. Sie sind sehr attraktive Strahlungsquellen für die Spektroskopie, da sie kompakt sind und typische Ausgangsleistungen von mehreren mW sowie Linienbreiten im MHz- bis kHz-Bereich aufweisen. Diese Arbeit beschäftigt sich mit der Entwicklung von Methoden, um die Emissionscharakteristika von THz-QCLs maßzuschneidern und sie für die hochauflösende und hochsensitive Spektroskopie zu verwenden. In vielen Fällen werden für diese spektroskopischen Anwendungen Fernfeldverteilungen mit einem einzelnen Maximum benötigt, jedoch wurden mehrere Maxima in den experimentell bestimmten Fernfeldverteilungen beobachtet. Es konnte eindeutig nachgewiesen werden, dass die Ursache für die Entstehung dieser Maxima in der Aufbaugeometrie des Laserchips sowie in der kryogenen Betriebsumgebung wie dem optischen Fenster zu finden ist. Ausgehend von diesen Ergebnissen wird eine Methode vorgestellt, mit der man eine Fernfeldverteilung mit nur einem Maximum erhält. Eine wesentliche Voraussetzung für die Verwendung eines THz-QCLs für die Spektroskopie einer einzelnen Absorptions- oder Emissionslinie ist die präzise Einstellung der Emissionsfrequenz. Dieses bereits lange bestehende Problem kann durch eine neu entwickelte Technik, die auf dem mechanischen Polieren der Frontfacette beruht, gelöst werden. Ein auf diese Weise hergestellter QCL ermöglicht Spektroskopie mit einer maximalen Auflösung im Bereich von MHz bis kHz, aber die zugängliche Bandbreite ist normalerweise auf einige GHz beschränkt. Im Gegensatz dazu erlaubt es eine neu entwickelte Technik, einen QCL als Quelle für ein THz-Fourier-Transform-Spektrometer zu verwenden, wodurch höchst empfindliche Spektroskopie mit einer deutlich größeren Bandbreite von mindestens 72 GHz und einer maximalen Auflösung von typischerweise 100 MHz möglich wird. Die Verwendung von QCLs als Quelle für THz Fourier-Transform-Spektroskopie erlaubt die Erhöhung sowohl des Signal-Rausch-Verhältnisses als auch des dynamischen Bereichs um den Faktor 10 bis 100 im Vergleich zur Verwendung von konventionellen Quellen. Die in dieser Arbeit vorgestellten Ergebnisse ebnen den Weg, um THz-QCLs in der nahen Zukunft routinemäßig für spektroskopische Anwendungen einzusetzen.

Contents

1 Introduction

The study of the interaction between light and matter using spectroscopic techniques has always been of great importance. A striking historic example is the spectroscopy of light from the sun, which essentially consists of a black-body spectrum with dark lines due to the absorption by the elements in the solar atmosphere (Fraunhofer lines). The effort to understand these effects contributed to the development of quantum mechanics, which is now the foundation of semiconductor technology. Prominent examples are microprocessors as well as light-emitting and laser diodes, which are are now part of every day's life through smart phones, solid-state lighting, and fiber-optic communication. Apart from these omnipresent benefits, semiconductor technology enables powerful experimental setups for research and efficient industrial processes. For instance, laser diodes are now being employed as light sources for spectroscopy, the field that was essential for their development.

Spectroscopy relies on the characteristic response of every material to radiation depending on its frequency. While the range from the visible spectrum to x-rays is related to ionization energies in atoms and molecules, the spectral range from the near- to the far-infrared corresponds to vibrational and rotational transitions in molecules as well as fine-structure transitions in atoms. The spectroscopically least explored region is the far-infrared or terahertz (THz) spectral range due to a lack of powerful sources and sensitive detectors. This lack is due to the different technologies employed to generate the radiation in the neighboring spectral regions, i.e., microwaves by electronic means and mid-infrared radiation by optical/photonic techniques. Recently, novel technologies have become available that can be employed for THz spectroscopy. One of these technologies is the THz quantum-cascade laser (QCL)—a unipolar semiconductor heterostructure laser.

The invention of the QCL followed a series of breakthroughs in the field of semiconductor lasers. Conventional laser diodes rely on the recombination of electrons and holes in high-quality semiconductor heterostructures. The emission frequency is determined by the band gap of one of the employed semiconductors so that emission only at material-specific frequencies is possible from conventional laser diodes. In order to overcome this strong dependence on the material-specific band gap of the employed semiconductors, a number of concepts—often summarized under the term *bandstructure engineering*—have been developed, which are based on the confinement of charge carriers in semiconductor quantum wells. In so-called quantum well lasers, the electron energies are increased with respect to the conduction band edge by manufacturing a sufficiently thin heterostructure well, and conversely, the hole energies are decreased with respect to the valence band edge. Consequently, the emission frequencies of quantum well lasers are increased as compared to conventional laser diodes that employ thicker heterostructure wells made from the same material system. Even more importantly, the specific emission frequency can be tailored to some extent via the quantum well thickness. In contrast to this rather straightforward

approach to obtain photon energies that are larger than the band gap, more sophisticated concepts are required to obtain emission frequencies that are smaller than the band gap. In interband cascade lasers, heterostructures based on three materials are employed to obtain a W-shaped conduction (and often also valence) band profile, through which an electron state is bound to the center barrier. Again, by adjusting the layer widths, the energy difference between the relevant electron and hole state is modified so that the emission frequency can be tailored within the near-infrared and short-wavelength mid-infrared spectral region.

While interband cascade lasers rely—just like laser diodes—on electron-hole recombination for the generation of radiation, QCLs are based on optical transitions in only a single band. A major challenge for these unipolar devices is to obtain population inversion between the laser states, which is met by exploiting non-radiative transitions to populate the upper or deplete the lower laser state. This is realized by means of a careful tailoring of the heterostructure sequence, through which the energy states can be controlled. QCLs for emission in the mid-infrared range have been first demonstrated in 1994 [1] and are already commercialized featuring output powers of hundreds of mW in continuous-wave operation at room temperature. The demonstration of QCLs for the THz range has turned out to be more difficult. While, after their first demonstration in 2002 [2], rapid progress was made toward additional emission frequencies and output powers in the mW range, the operating temperatures remain below 200 K in pulsed [3] and below 129 K in continuous-wave [4] operation. Thus, powerful coolers are still required, which impedes widespread commercialization.

Despite the requirement of cryogenic cooling, the enormous spectral brightness of THz QCLs as well as their robustness has triggered significant efforts to employ them for practical spectroscopic applications. For example, gas lasers for the emission in the THz range, which have long been used for research requiring narrow-linewidth radiation, are now being replaced by THz QCLs. Another example for the application of THz QCLs is the German receiver for astronomy at terahertz frequencies (GREAT) on board of the stratospheric observatory for infrared astronomy (SOFIA). Here, a THz QCL with a linewidth in the kHz range and with an output power of several mW emitting at 4.747 THz is employed as a local oscillator in a heterodyne receiver for the high-resolution spectroscopy of a fine-structure transition in atomic oxygen. The fabrication of a QCL for such an application is challenging due to the demanding requirements on the emission frequency, which varies significantly among nominally identical devices. Therefore, one topic of this thesis is the quantitative understanding of this phenomenon and the development of a suitable technology for a reliable fabrication of THz QCLs that emit at a precisely defined, application-specific frequency. While this approach aims at obtaining a very high resolution in the kHz range, but over a limited spectral bandwidth, a larger bandwidth would allow for more experimental flexibility. Therefore, as a second topic, a novel concept was developed in the framework of this thesis to employ QCLs as sources for THz Fourier transform spectrometers. In this way, highly sensitive spectroscopy at a maximal resolution of typically 100 MHz is possible, utilizing the high spectral brightness of THz QCLs. An important prerequisite for applications is a far-field distribution that meets the setup-specific requirements. Therefore, as

a further topic of this thesis, the far-field distribution is investigated, and a method for its improvement is demonstrated.

A century after the development of quantum mechanics, which could explain the results of spectroscopic experiments, this understanding has culminated in major technological advances such as the development of the QCL. These lasers are finally employed for novel spectroscopic techniques in the hardly explored THz spectral range with unprecedented sensitivity and resolution, enabling new discoveries and technological breakthroughs.

This thesis is structured as follows. First, the fundamentals of THz QCLs as well as the employed technological and experimental methods are described in chapters 2 and 3. The subsequent chapters deal with the three topics outlined above. For all experiments, QCLs based on single-plasmon waveguides were selected, since these waveguides are employed in almost all proof-of-principle demonstrations of spectroscopic experiments due to their relatively directional emission as compared to typical QCLs with metal-metal waveguides. Chapter 4 presents the investigation of the far-field distribution and a method for its improvement. In chapter 5, the parameters on which the exact emission frequency of a THz QCL depends are investigated, and a method for its precise control is presented. Chapter 6 deals with the application of a QCL as a source for a THz Fourier transform spectrometer. This replacement gives rise to an increase of the signal-to-noise ratio and dynamic range by a factor of 10 to 100. The thesis concludes with a summary and outlook in chapter 7.

2 Fundamentals of terahertz quantum-cascade lasers

This chapter provides a brief introduction to terahertz quantum-cascade lasers. In section 2.1, the most important properties of THz radiation are described. Furthermore, THz QCLs are compared to other sources of THz radiation. Section 2.2 addresses the fundamentals of the active region of THz QCLs. After a description of the basic principles in subsection 2.2.1, the different types of active-region designs are briefly presented in subsection 2.2.2. In addition, an overview of the different modeling techniques employed to predict the operating parameters of THz QCLs is given in subsection 2.2.3. The section about the active regions closes with subsection 2.2.4, which gives more details on a particular simulation technique. Finally, section 2.3 provides a brief introduction to the waveguide and resonator types usually employed for THz QCLs.

2.1 Terahertz radiation

The THz spectral range refers to the transition region between high-frequency microwaves and long-wavelength infrared radiation. This denotation has been adopted in the 1970s to refer to the short millimeter and sub-millimeter range, which was technologically underdeveloped in terms of sources and detectors [5]. While predominantly earlier literature defines THz frequencies (wavelengths) to range between 0.1 and 30 THz (3 mm and 10 µm), recent literature more often specifies a narrower interval from 0.3 to 10 THz (1 mm to 30 µm). Similarly to the THz spectral range, the assignment of the far-infrared spectral range to a frequency interval is not consistent throughout the literature. However, it always has a large overlap with the definitions of the THz spectral range as given above. Therefore, far-infrared radiation is employed as a synonym to THz radiation in this thesis.

As every spectral range, THz radiation has its own set of unique properties. The photon energies of radiation with frequencies between 0.1 and 30 THz range from 0.4 to 120 meV and therefore correspond to fine-structure transitions in atoms and rotational transitions in molecules. The peak absorbance of many molecules of interest lies in the THz range, allowing for trace gas detection with peak sensitivities. Since water is among the strongly absorbing materials in the THz range, the typical amounts of water vapor in air often render optical setups for THz radiation impossible unless the optical paths are very short or the vapor is removed by flushing or evacuation.

Transitions in the THz range in atoms and molecules can also be exploited to unambiguously determine a certain species, which is sometimes referred to as fingerprint spectroscopy [6]. Furthermore, it can also be used to determine the abundance and other param-

eters of various species. An important example is the measurement of the Doppler shift of atomic oxygen in outer space and in the atmospheres of planets in the solar system [7, 8]. Additional important applications lie in the research on semiconductors and other solids as well as on liquids, gases, and plasmas.

With microwaves, THz radiation shares the high transmission through dry, non-conducting materials such as plastics, but its shorter wavelength allows for a higher resolution in diffraction-limited imaging or in the determination of thicknesses [9]. These properties are already exploited in quality-control applications [10]. The strong absorption of THz radiation by conducting materials can also be utilized via imaging through scanning near-field optical microscopy, which has applications for example in the electronics industry for the quality control of soldering connections [11].

Low-frequency THz radiation can be generated with compact electronic devices and is therefore very interesting for wireless communications, since additional frequency bands are required for the ever-increasing need for more bandwidth [12]. However, due to the large number and strength of atmospheric absorption bands as well as sensitivity issues of THz transceivers, only short-distance line-of-sight systems are readily conceivable.

A large number of possibilities to generate and detect THz radiation have been demonstrated in the last three decades. Here, the focus is placed on sources that can be employed for spectroscopic applications in the THz spectral range. Figure 2.1 provides an overview of sources and spectroscopic techniques in the THz range. An important figure-of-merit for spectroscopy is the resolution. While the resolution of laser-based spectroscopic techniques is determined by the linewidth of the laser emission, the resolution of spectrometers employing broadband sources depends on the parameters of the frequency-dispersive mechanisms. In Fig. 2.1, typical linewidths of THz laser sources and resolutions of THz spectrometers are shown. A technique, which has already been commercialized for decades, is Fourier transform spectroscopy. It employs broadband sources spectrally decomposed by a Michelson interferometer. While tabletop Fourier transform spectrometers have a resolution not better than 2 GHz, larger ones can typically reach 0.1 GHz. Since the spectral brightness of the sources in the THz range is only of the order 1 μW/0.1 GHz, liquid-Helium-cooled bolometers have to be used as detectors for sensitive measurements. Recently, time-domain spectroscopy has been commercialized, which employs short pulses (often in the femtosecond range) of a visible or near-infrared laser focused onto a photoconductive switch in order to create short (usually few-cycles-long) THz pulses. This technique is also employed inversely to coherently sample the pulse in the time domain. A spectrum is obtained via a Fourier transformation. The strength of this technique is the large frequency coverage over more than 3 THz and the possibility to perform time-of-flight measurements of the short pulses. However, the resolution is usually limited to the GHz range as Fig. 2.1 shows. A further commercially available technique is difference-frequency generation by means of two detuned visible or near-infrared lasers. While continuous-wave emission is obtained with this technique, the spectral coverage is restricted to low THz frequencies, and the output powers usually do not exceed 100 μW. The linewidth of THz emission via difference-frequency generation is determined by the employed lasers and typically amounts to about 1 MHz. A similar technique is difference frequency generation by means of mid-infrared

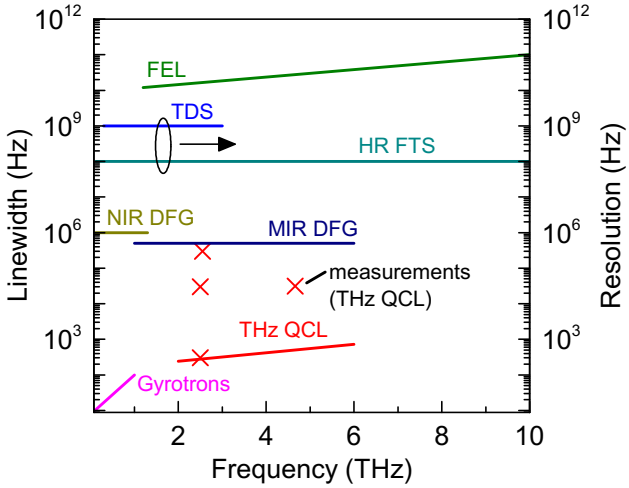

Figure 2.1: Typical linewidth of laser- or gyrotron-based THz sources and typical resolution of THz spectrometers. FEL: Free-electron laser, e.g. *FELBE* or *FELIX* [13]. TDS: Commercially available THz time-domain spectrometer [14]. HR FTS: Commercially available high-resolution Fourier transform spectrometer [15]. NIR DFG: Difference frequency generation by mixing of two near-infrared lasers [16]. MIR DFG: Difference frequency generation by intra-cavity mixing of mid-infrared radiation [17]. THz QCL: Theoretical limit of linewidth [18] and linewidth measurements [19–22]. Gyrotrons may have a linewidth below 100 Hz [23].

QCLs. Here, for the most powerful devices, the difference frequency is created inside the cavity of a two-color QCL and out-coupled via a Cherenkov scheme. In this way, the spectral coverage can be increased toward higher THz frequencies. However, the typical linewidths and power levels are comparable to difference frequency generation from visible or near-infrared light.

The radiation emitted by electronic means such as Schottky diode multiplier chains or gyrotrons usually feature small linewidths and sometimes also a large tunability. However, the output powers of electronic devices are only sufficiently high below 1 THz, while they are usually too low for practical applications above 1 THz. In contrast, a powerful method for tunable THz radiation is the free-electron laser. It employs a linear accelerator for electron packets. Transform-limited THz pulses with ps durations are usually generated employing an undulator integrated with an optical resonator. Because of the short pulses and high average powers in the kW range, THz radiation from free-electron lasers is usually applied for time-resolved measurements or experiments on samples with high absorption. THz radiation from free-electron lasers is not particularly well suited for high-resolution spectroscopy, since the linewidth is quite large due to the short pulse durations. Another accelerator-based

THz source is an electron storage ring, which can generate broadband THz radiation with average powers on the order of 10 mW in the so-called low-alpha mode or by employing external lasers to induce superradiant emission in the electron beam. Since the emission is broadband, the achievable resolution is limited by the employed spectrometer, which is usually of the Fourier transform type. A quite recent development is superradiant emission from newly invented, so-called energy-recovery linear accelerators, which can generate THz radiation over a similar frequency range as storage rings while providing substantially higher output powers [24].

Figure 2.1 shows that THz QCLs are very well suited for high-resolution spectroscopy between 2 and 6 THz. In addition, the routinely achieved average output powers lie above 1 mW so that measurements with high sensitivity are possible. While THz generation based on two mid-infrared QCLs has some advantages such as room temperature operation and large tunability, the linewidth is currently limited to the MHz range. Even more importantly, the output power is mostly below 100 µW. Since in this case the generation of THz radiation relies on a non-linear mechanism, it is not expected that the output power can be substantially increased in the near future. Therefore, THz QCL-based spectroscopy is the method of choice for high-resolution and high-sensitivity measurements in the range from 2 to 6 THz.

2.2 Active region of terahertz quantum-cascade lasers

The operation principle of QCLs is based on a scheme first described by Kazarinov and Suris [25] in 1971. In an even earlier work by Esaki and Tsu, the formation of minibands and minigaps in periodic semiconductor heterostructures was already predicted [26]. It took more than two decades until the first QCL was demonstrated experimentally by Faist *et al.* [1]. The demonstrated QCL emitted in the mid-infrared spectral region, i.e. energetically above the restrahlenbands of the semiconductors it was based on. While the first QCLs for emission above the reststrahlenbands needed cryogenic cooling, rapid progress was made to obtain operation at room temperature [27], high optical powers [28], and emission at additional frequencies [29]. The demonstration of THz QCLs, i.e. QCLs for the emission below the semiconductor reststrahlenbands, was only realized in 2002 by Köhler *et al.* [2]. Although much progress has been made in terms of output power and emission frequencies since then [24, 30], the maximum operation temperature is restricted to values below 200 K in pulsed [3] and 129 K in continuous-wave [4] mode. Moreover, the power conversion efficiency of the best THz QCLs is about 0.1% [31], several orders of magnitude lower than for QCLs that emit above the reststrahlenbands. The physical origins of these unfavorable performance values are only marginally understood so far.

The emission of terahertz radiation is realized by transitions of confined charge carriers in coupled quantum wells. The frequency of the emission can be tailored, since it depends on the energy difference between the involved quantum states, which, in turn, is determined by the quantum well widths as well as the barrier thicknesses and heights. For lasing, a sufficient population inversion must be established, which is achieved by a careful tailoring of non-radiative scattering mechanisms and resonant tunneling. These scattering mechanisms

along with their radiative counterpart are briefly introduced in subsection 2.2.1, which also includes a brief description on the carrier energies in semiconductors. Subsection 2.2.2 provides an introduction to typical active-region designs. The various numerical approaches to predict the properties of THz QCLs are introduced in subsection 2.2.3, while subsection 2.2.4 provides more details of a successful technique for the prediction of the operating properties of THz QCLs. The discussion of the active region has been in part restricted to electrons as charge carriers for simplicity, since THz QCLs based on holes have not been demonstrated so far.

2.2.1 Energy, transport, and transitions of charge carriers in semiconductor heterostructures

The energy of charge carriers in semiconductors is described by the band structure, which can be calculated with various techniques. Very powerful techniques are based on density functional theory and are quite popular nowadays since they have substantially lower computational costs than techniques based on Hartree-Fock theory that directly include electron correlation [32]. Since the employed approximations in density functional theory have been continuously improved throughout the last decades, it provides quite accurate results. Other techniques are based on the tight-binding [33] or on the pseudo-potential [34, 35] model. Of particular significance is the $\mathbf{k} \cdot \mathbf{p}$ perturbation theory [36], since it provides explicit expressions for important quantities such as effective masses and wave functions. In addition, it can be applied to semiconductor heterostructures using the envelope function model. The $\mathbf{k} \cdot \mathbf{p}$ theory is briefly introduced in section 2.2.4.

If a semiconductor heterostructure forms a quantum well, i.e. a planar potential profile with typical dimensions on the order of the de-Broglie wavelength of the considered charge carrier type, subbands are created through the confinement of the carriers in the out-of-plane direction. The subband energies are modified via the coupling of quantum wells so that they can be tailored not only by the quantum well widths, but also by the coupling strengths between the wells. An optical transition between two subbands can lead to the emission and absorption of a photon with an energy according to the energy separation of the subbands. A prerequisite for lasing is population inversion of the states involved in the optical transition. Population inversion via electrical injection is usually preferred in semiconductor lasers. Since the optical transition in QCLs takes place between two states of the same charge carrier instead of electron-hole recombination, population inversion depends very sensitively on the carrier transport through the heterostructure.

Charge carrier transport and transitions in semiconductor heterostructures are mediated by diffusion, tunneling, and scattering. Diffusion due to the momentum of the carriers mainly plays a role in obtaining a distribution in agreement with the chemical potential. Tunneling of charge carriers allows for the transport of carriers in bound states through the barriers of the heterostructure. Scattering may take place between at least two particles, which exchange energy and momentum. Some specific scattering mechanisms can also be understood as single-particle processes, exchanging energy or momentum with a “bath” of other particles. This kind of scattering is often referred to as incoherent and may be ex-

pressed as a potential in the corresponding Hamiltonian of the single particle. In contrast, tunneling and explicit two-particle scattering mechanisms are usually referred to as coherent processes, since the wave nature of the particles play a more important role than for incoherent processes.

One of the most important scattering mechanisms for quantum-cascade lasers is of course the photon-assisted transition, through which a carrier can lose (or gain) energy via the emission (or absorption) of a photon. This emission of a photon may take place spontaneously or in a stimulated way enabling laser operation. To ensure population inversion and hence the dominance of stimulated emission over absorption, the non-radiative scattering mechanisms may be tailored via the heterostructure design. The discussion of these scattering mechanisms will be restricted to the GaAs/(Al,Ga)As material system, since it is employed for the vast majority of THz QCLs.

In order to obtain population inversion, the upper laser level has to be selectively populated or carriers have to be selectively extracted from the lower laser level. One option is to employ the nonradiative transition assisted by the emission of a longitudinal optical (LO) phonon, which is very fast. To populate the upper laser level, the heterostructure is designed such that the upper laser level is separated by the LO phonon energy from a suitable level above it. Conversely, to rapidly extract carriers from the lower laser level, it must be separated by the LO phonon energy from a suitable energy level energetically below.

Another option to achieve population inversion of the laser levels is to employ scattering in quasi-minibands. Analogous to the formation of energy bands in solids due to the periodic arrangement of atoms, minibands are created by periodic heterostructures in semiconductors, i.e. superlattices, so that the obtained states can be viewed as a continuum. In contrast, quasi-minibands in QCLs are formed by only a small number (typically about 10) of coupled wells, which are not strictly periodic. Rather, they either consist of a chirped superlattice or are modified in a more complex way. Although quasi-minibands consist only of a comparably small number of states due to the limited number of coupled wells, they still exhibit a quite small energetic separation, enabling low-energy scattering processes to take place. One of these processes is electron-electron scattering. This scattering process may occur within a subband of one state (intrasubband scattering) or between subbands (intersubband scattering). While intrasubband electron-electron scattering plays a role in the thermalization (obtaining thermal equilibrium) in the subband, intersubband scattering may increase the population of a state in the subband at lower energies. However, since energy and momentum need to be conserved in the scattering process, the temperature of the electrons in the subbands is increased upon scattering to an energetically lower subband. The electron temperature may be reduced by scattering between electrons and acoustic phonons, which exhibit small energies for small momenta. As a consequence, heat is produced, which is removed via the heat sink of the cooling system. Apart from cooling the electrons, emission of acoustic phonons may also directly lead to transitions from the energetically higher subbands to lower subbands. As a result of electron-electron and electron-acoustic-phonon scattering, the carriers are redistributed so that the upper edge of the quasi-miniband is less populated than its lower edge. Therefore, a quasi-miniband can be employed to extract carriers from the lower laser level and to populate the upper laser level. For that purpose, the

upper (lower) edge of the quasi-miniband directly represents the lower (upper) laser level or is coupled to a corresponding bound state by resonant tunneling.

Apart from electron-electron and electron-phonon scattering, which have been put to good use via ingenious active-region designs, there are further non-radiative scattering mechanisms that are largely considered to be only detrimental. Interface roughness scattering is a mechanism that depends strongly on the structural quality of the heterostructure. A special case is the interface grading, which occurs for the vastly used GaAs/(Al,Ga)As material system and which can be reduced by only a limited amount due to the finite shutter times of the effusion cells in molecular beam epitaxy. However, interface grading is not necessarily a detrimental effect, since it can be experimentally determined by, for example, transmission electron microscopy [37, 38] and taken into account for the design of the active region [39].

Alloy disorder scattering is inherent to all alloys such as (Al,Ga)As. Since the alloy (Al,Ga)As is usually only employed for the quite thin barriers of the quantum wells, the detrimental effect remains limited. Alloy disorder scattering can be further reduced by employing a non-alloy barrier material such as pure AlAs so that it is restricted to the regions exhibiting interface grading [31].

Scattering at ionized impurities is usually considered as a further detrimental mechanism. The impurities are primarily represented by dopants. Since a reduction of the doping density would lead to a substantial self-charging of the active region upon biasing and would thus result in a detrimental band bending, ionized impurity scattering cannot be completely eliminated.

2.2.2 Active-region designs

Laser operation in QCLs relies on tailoring non-radiative scattering mechanisms to achieve population inversion of the laser levels. These mechanisms have been described in the previous subsection. In this subsection, the important active region designs from the literature are described.

A general feature of the QCL active regions is the cascading scheme, which means that the active region consists of several repetitions of a specific layer sequence, usually referred to as stage or period. When an appropriate bias is applied to the heterostructure, electrons may pass the first stage emitting one photon per electron, after which they are injected into the next stage so that additional photons may be emitted. In this way, electrons injected into the active region are “recycled” several times and may give rise to the emission of several photons per electron corresponding to the number of stages. Although in the literature this recycling is sometimes interpreted as a quantum efficiency larger than 1, it does not constitute a principal advantage, since the generation of a photon in every stage is linked to a corresponding energy loss via the non-radiative scattering mechanisms. In fact, the application of the cascading scheme is rather of photonic origin and aims at increasing the confinement factor and decreasing the optical losses. This relationship will be elucidated in section 2.3.

Figure 2.2 illustrates the most important designs for one period of the active regions as described in the literature. One of the first designs for THz QCLs is referred to as chirped-

superlattice design [2], which is depicted in Fig. 2.2(a). In every stage, two quasi-minibands are created, between which an optical transition and thus photon emission may take place. Through electron-electron and acoustic-phonon-electron scattering, each quasi-miniband is thermalized so that their upper edges are substantially less populated than their lower edges. Thus, population inversion is created between the lower edge of the subband at higher energies and the upper edge of the energetically lower subband. Figure 2.2(b) shows

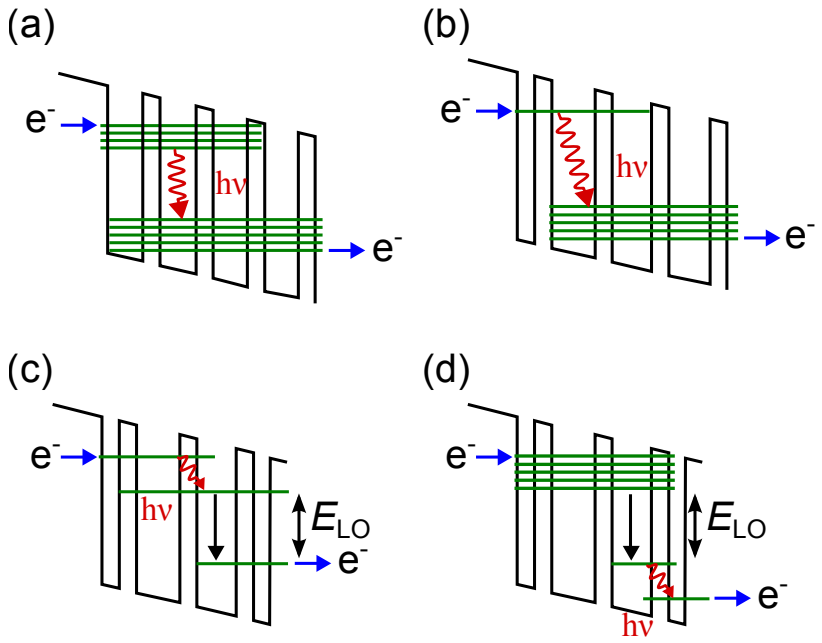

Figure 2.2: Illustrations of the most important active region designs for THz QCLs. The black lines depict the conduction band edges and the green horizontal lines the subband edges. The red, wavy arrows mark the transitions mediated by photon emission ($h\nu$). Transitions that are in resonance with the LO phonon energy (E_{LO}) are marked with black arrows. (a) Chirped-superlattice design; (b) bound-to-continuum design; (c) LO phonon extraction design; (d) hybrid design.

a design in which the laser transition takes place between a quasi-bound state and the upper edge of a quasi-miniband [40]. Since a quasi-miniband can be viewed as a quasi-continuum of states, the design is referred to in the literature as bound-to-continuum design. The active-region design illustrated in Figure 2.2(c) employs two quasi-bound states as the laser levels. The layer sequence is designed such that the energy separation between the lower laser level and an additional bound state is in resonance with the LO phonon energy [41]. In this way, the lower laser level is rapidly depopulated through the emission of an LO phonon. This kind of active region is referred to in the literature as resonant-phonon design.

THz QCLs with active regions based on chirped-superlattice and bound-to-continuum designs exhibit a relatively low self-heating. In contrast, QCLs based on the resonant-phonon design may have higher output powers for the same device dimensions due to the

higher gain values of this design type. However, the self-heating is also increased, which impairs continuous-wave operation. As a compromise between these two schemes a hybrid design as illustrated in Fig. 2.2(d) can be applied [42]. THz QCLs based on the hybrid design exhibit high power levels while the dissipated heat is sufficiently low to achieve continuous-wave operation so that record-high operating temperatures in continuous-wave mode could be achieved [4]. The hybrid design employs a resonant-phonon transition for the population of the upper laser level and a quasi-miniband for the extraction of carriers from the lower laser level.

As the current applied to a QCL is increased, the optical output power increases substantially once the threshold current has been reached. However, there are several mechanisms that limit the attainable output power. An effect well known for semiconductor superlattices is negative differential resistance, which has been shown to also occur in the more complex QCL active regions [43]. For some active-region designs, the onset of negative differential resistance determines the maximal current for which lasing is observed, since electric-field domains are formed that substantially alter the population of the states. This population is generally also modified as the voltage applied to the QCL is increased. Depending on the specific design of the QCL active region, significant population inversion is only generated within a limited range of applied voltages so that no lasing is observed beyond the corresponding current range. This is often the limiting mechanism for bound-to-continuum designs. The population inversion can also be reduced by parasitic scattering channels that open up at higher temperatures. This temperature dependence is an issue especially for THz QCLs in continuous-wave operation due to the substantial self-heating. As the current is increased in continuous-wave mode, the optical output power usually first increases after threshold, but then it often reaches a maximum and gradually decreases, since the temperature within the active region has attained values that lead to a reduction of the population inversion and to an increase of the waveguide losses. This behavior is often referred to as thermal roll-over. Therefore, active regions with a good power conversion efficiency are necessary for high output powers in continuous-wave operation [31].

Laser operation of THz QCLs is limited to temperatures below 200 K [3]. Several mechanisms may contribute to this limitation. First, a higher lattice temperature corresponds to phonons being present at various energies and momenta. These phonons may be absorbed to excite electrons to parasitic states or the continuum so that the optical transitions are bypassed. In addition, a high electron temperature opens up a channel for a reduction of the population inversion via an LO phonon-assisted diagonal (k-space) transition [44]. Furthermore, active regions based on transitions assisted by LO phonon emission may suffer from back-filling of carriers through absorption of LO phonons that are abundant at high temperatures. Moreover, similar to what was discussed for continuous-wave operation, the waveguide losses also increase for higher temperatures so that higher gain values are necessary to obtain lasing. The relative impact of each mechanism on the temperature behavior of THz QCLs is hitherto unknown.

The power conversion efficiency, i.e., the generated optical power versus the applied electrical power, amounts to usually below 0.1% for THz QCLs even at low temperatures. This low value of the conversion efficiency may have various origins. First, the purely parasitic

scattering mechanisms such as alloy disorder, charged impurity, and interface roughness scattering may play a role. In addition, the fact that the energy of THz radiation is below the restrahlenband of the semiconductors that are employed to manufacture THz QCLs may be important. The energy that is lost upon the emission of LO phonons in active regions based on LO phonon-mediated extraction is substantially higher than the energies of the emitted photons. In addition, the energies of acoustic phonons cover a quite large range in the GaAs/(Al,Ga)As material system. Thus, parasitic transitions assisted by acoustic-phonon emission may also reduce the power conversion efficiency. The relative impact of the described mechanisms on the conversion efficiency is so far unknown, and additional, hitherto undiscovered parasitic mechanisms may exist.

2.2.3 Overview of modeling techniques

The active region of a THz QCL is essentially a set of coupled quantum wells, on which an external electric field is applied. The most important purpose of an appropriate computational model is to predict the optical gain and the current density as a function of the field strength applied to the active region. In addition, the change of the refractive index as a function of the gain is interesting, since it influences inherent tuning capabilities of THz QCLs. As the externally applied field strength can usually be considered as constant for fixed operating conditions, the time dependence of the wave functions is purely harmonic so that it suffices to solve the time-independent Schrödinger equation. In addition, the Poisson equation should also be considered, since the charge distribution within an active region period also affects the states and hence the scattering rates. Therefore, the time-independent Schrödinger equation and the Poisson equation must be solved self-consistently.

Using the non-equilibrium Green's function theory, the Schrödinger and Poisson equations can be solved with the full Hamiltonian including all scattering mechanisms to calculate the energies and occupation numbers of the electronic states [45–47]. However, the computational costs are very large so that some simplifications have usually to be made such as restricting the number of considered states. As an alternative, one may consider the transport mechanisms as a perturbation so that transport is considered between the eigenstates of the unperturbed Hamiltonian (without transport mechanisms). The treatment of the transport mechanisms may be carried out quantum mechanically using the density matrix approach [3, 48, 49]. The density matrix is a representation of the quantum mechanical density operator for a specific set of states. In the picture of quantum statistics, a system of particles, here a system of electrons, occupies each pure state with a certain probability, giving rise to mixed states. This situation is expressed as a superposition of the pure states (more precisely the ket-bra operator of the states) weighted by the probability of their occupation, which constitutes the density operator. The density matrix approach is especially well suited to include coherent transport mechanisms such as tunneling, but may also include the incoherent scattering mechanisms. Since the computational effort for density matrix calculations is still quite high, semi-classical methods with their relatively small computation times are very well suited, especially for the purpose of designing active regions for specific applications. Carrier transport is usually modeled via a Boltzmann rate equation, which links the time derivative of the carrier occupation number of a specific state

with the scattering rates [50, 51]. The scattering rates are either determined empirically [52] or calculated from the corresponding interaction Hamiltonians [53]. Especially if the time evolution and also the in-plane momentum distribution of the electrons are to be calculated, Monte Carlo methods for the solution of the Boltzmann equation are most suitable, since in this case large multidimensional sums have to be computed [54]. The calculations are carried out over randomly selected elements according to an appropriate distribution (importance sampling) instead of explicitly calculating every combination of the sums. The advantage of the Monte-Carlo approach is based on the fact that—independently of the dimension of the sum—the numerical error is inversely proportional to the square root of the number of considered particles. However, especially the determination of the time evolution of the occupation number of the states is usually not necessary for the design of active regions so that the computational effort of the Monte Carlo method is still unnecessarily high.

The steady state of the occupation numbers can be calculated by requiring their time derivative to be zero so that the Boltzmann equation can be transformed via the neutrality condition into a system of linear equations, which can be solved at low computational cost [55]. Due to the scattering of the charge carriers, the charge distribution over a period is altered with respect to the initial situation. This effect may be accounted for by a self-consistent approach. Starting from an initial carrier distribution, the scattering rates (and wavefunctions) are calculated. The carrier distribution is corrected according to the scattering rates, and the problem is solved again until the changes are negligible. This approach turned out to yield quite accurate results and is well suited especially for the design of active regions, for which a large number of potential design candidates have to be simulated. This approach is described in more detail in subsection 2.2.4.

The photon-assisted scattering plays a special role not only because it is the basis for the generation of radiation, but also because it represents the channel for the interaction between the electron system and the radiation field. Within a simple model of a laser device, the population inversion increases with the pump power until the lasing threshold is reached. Upon a further increase of the pump power, the population inversion and therefore the optical gain remains constant, which is usually referred to as gain clamping. In order to account for this and further effects, the Maxwell-Bloch equations may be employed, which describe the interaction between electronic states and an electromagnetic field in a quite rigorous way [56]. However, including this interaction within the calculation of the QCL characteristics adds another degree of complexity, again increasing the computational cost, which is why an efficient treatment is subject of current research [57].

2.2.4 Self-consistent simulation of the gain and the transport properties

In this subsection, a very successful technique to simulate the gain and transport properties of THz QCLs is presented [52, 55]. It is based on the $\mathbf{k} \cdot \mathbf{p}$ theory for the electronic states in semiconductor quantum wells and on the self-consistent solution of the Schrödinger and Poisson equation in Fourier space.

Electronic states in semiconductor quantum wells based on $\mathbf{k}\cdot\mathbf{p}$ theory

The electronic states in semiconductor quantum wells can be calculated starting from the $\mathbf{k}\cdot\mathbf{p}$ approximation. The $\mathbf{k}\cdot\mathbf{p}$ approximation is a local description of the electronic dispersion relation for small values of the electron wave vector $\mathbf{k}$ around the band extrema. Its advantage in contrast to methods such as the tight-binding model is that it provides explicit expressions for important quantities such as effective masses, wave functions etc. The ansatz of the $\mathbf{k}\cdot\mathbf{p}$ method is to separate the Hamiltonian into a $\mathbf{k}$-independent part, here at $\mathbf{k}=0$, and a $\mathbf{k}$-dependent part:

$$H(\mathbf{k}) = H(\mathbf{k}=0) + W(\mathbf{k}) \; . \tag{2.1}$$

The $\mathbf{k}$-dependent part $W(\mathbf{k})$ of the Hamiltonian is treated in a first-order perturbative approach employing the Bloch wave functions at $\mathbf{k}=0$, i.e.

$$u_{n,\mathbf{k}=\mathbf{0}}(\mathbf{r}) \; , \tag{2.2}$$

where n denotes the number of the energy band and $\mathbf{r}$ the coordinate in real space. As a result, a quadratic approximation of the $\mathbf{k}$-dependent energy bands resulting in a constant effective mass of the considered charge carrier is obtained. An improvement of this approximation via a straightforward second-order perturbative treatment of $W(\mathbf{k})$ turns out to be quite cumbersome. Kane proposed in a celebrated paper an elegant way to simplify the second-order perturbative treatment [58]. First, $W(\mathbf{k})$ is *exactly* diagonalized within a limited set of band edges, and afterwards the coupling between the considered and so far neglected bands is treated within a second-order perturbative approach. In this way, the non-parabolicity of the energy bands or equivalently an energy-dependent effective mass is taken into account.

A heterostructure of two lattice-matched materials A and B can be treated within the envelope function model. Within this model, it is postulated that the wave functions of the heterostructure can be expanded as

$$\Psi(\mathbf{r}) = \sum_l f_l^{(A,B)}(\mathbf{r}) u_{l,\mathbf{k}_0}(\mathbf{r}) \; , \tag{2.3}$$

where the functions $f_l^{(A,B)}(\mathbf{r})$ are slowly varying on the scale of the variations of the Bloch functions $u_{l,\mathbf{k}_0}(\mathbf{r})$. Due to the in-plane translational invariance of the heterostructures, $f_l^{(A,B)}(\mathbf{r})$ can be factorized into

$$f_l^{(A,B)}(\mathbf{r}) = \frac{1}{\sqrt{S}} \exp\left(i\mathbf{k}_\perp \cdot \mathbf{r}_\perp\right) \chi_l^{(A,B)}(z) \; , \tag{2.4}$$

where S is the sample area, $\exp\left(i\mathbf{k}_\perp \cdot \mathbf{r}_\perp\right)$ the in-plane and $\chi_l^{(A,B)}(z)$ the out-of-plane wavefunction. Employing this ansatz for the Schrödinger equation leads—after appropriate transformations—to a diagonal block matrix whose eigenfunctions and eigenvalues represent the wave functions and energies of the electronic states in the heterostructure.

Scattering rates and self-consistent calculation of occupation numbers

The scattering rates T_{ij} between two states i and j may be approximated by a product of a function τ that depends only on the energy difference ΔE between the two states and the modulus squared of the transition dipole moment D_{ij} [52] so that T_{ij} may be expressed as

$$T_{ij} = \tau(\Delta E)|D_{ij}|^2 \,. \tag{2.5}$$

The factor $|D_{ij}|^2$ represents an approximate form factor for the scattering processes. The wave functions obtained from the solution of the Schrödinger (and Poisson) equation are employed to calculate T_{ij}. The calculation of the wave functions and their energies is based on the envelope function approach within the Kane model in the framework of the $\mathbf{k}\cdot\mathbf{p}$ theory, which was introduced in the previous subsubsection. The block matrix is reduced to a 2×2 matrix by restricting the treatment to electrons as charge carriers and neglecting spin degeneracy. The effects of the valence bands on the electrons are lumped into a single pseudo valence band so that an effective 2-band model for electrons in semiconductor heterostructures is obtained.

The effect of the charge distribution on the band structure is described by Poisson's equation

$$\nabla^2\phi = -\frac{\rho}{\varepsilon_0\varepsilon}, \tag{2.6}$$

where ϕ is the electric potential, ρ the charge carrier distribution, ε_0 the permittivity of the vacuum, and ε the relative permittivity. The potential due to the charge carrier distribution leads to a band bending and therefore modifies the energies of the electronic states. Since the scattering processes alter the charge carrier distribution so that the energies of the wavefunctions and therefore the scattering rates are modified, the wavefunctions and scattering rates are calculated alternatingly. This iterative scheme is terminated once self-consistency is achieved, i.e., if the modification of the occupation numbers by the scattering processes with respect to the previous iteration is negligible.

The function $\tau(\Delta E)$ in equation (2.5) is crucial for the accurate calculation of the scattering rates. It may be determined semi-empirically by considering the asymptotic behavior of approximations for a set of energy ranges (especially for small and large ΔE) [52].

As an alternative to the approach described so far, one may calculate the scattering rates more rigorously by considering the interaction Hamiltonian of the scattering mechanisms [53]. The increased computation time of the more rigorous approach is unproblematic, if the total computation time is substantially reduced by solving for the states and scattering rates in the Fourier domain and if efficient numerical procedures are employed for the numerical integrations [53, 55, 59].

The solution of the Schrödinger equation may be performed either in real or in Fourier space. The computational cost of the calculation in Fourier space is typically lower than in real space, since the wave functions can be expanded into a Fourier series with a smaller number of components than in real space. Furthermore, the Fourier approach is well-suited to include periodic boundary conditions. An additional advantage of the Fourier approach is that the interface grading can readily be taken into account [60]. A challenge of the Fourier

transform-based approach is the necessary transformation of the scattering rates to Fourier space and their fast numerical calculation [53, 59].

2.3 Waveguides and resonators

In addition to the active region, the waveguide and the resonator are vital elements of a THz QCL. A ridge waveguide is characterized by an inhomogeneous spatial profile of the (complex) refractive index in two directions, which gives rise to a localized waveguide mode. The waveguide mode propagates in the third, translationally invariant direction. In contrast to ridge waveguides, planar waveguides are characterized by a one-dimensional heterogeneous profile of the refractive index and therefore exhibit translational invariance in two directions.

In conventional semiconductor lasers, the active region is typically sandwiched between two layers of lower refractive index. These layers are doped to allow for the electrical injection into the active region. While the free carriers due to the doping do not significantly affect the generated light in the visible to mid-infrared range, they lead to strong absorption in the THz region, since the absorbance by free carriers increases with the wavelength squared. Therefore, novel types of waveguides with low losses in the THz range were developed to obtain laser emission from THz QCLs [2, 41].

Figure 2.3(a) schematically shows the design of a single-plasmon waveguide for the ridge-type THz QCL. Directly on top of the active-region heterostructure, a metal layer—usually gold—is deposited, which limits the waveguide mode on the top. In addition, the electrical injection takes place through that layer. The extraction of charge carriers is realized with a highly doped semiconductor layer underneath the active region. Since this layer is thin (about 0.7 µm) as compared to the wavelength in the material (about 30 µm), the losses due to free carriers are limited. The highly doped layer plays the additional role of confining the waveguide mode via the excitation of surface plasmon-polaritons. However, the waveguide mode penetrates substantially into the substrate, since the refractive

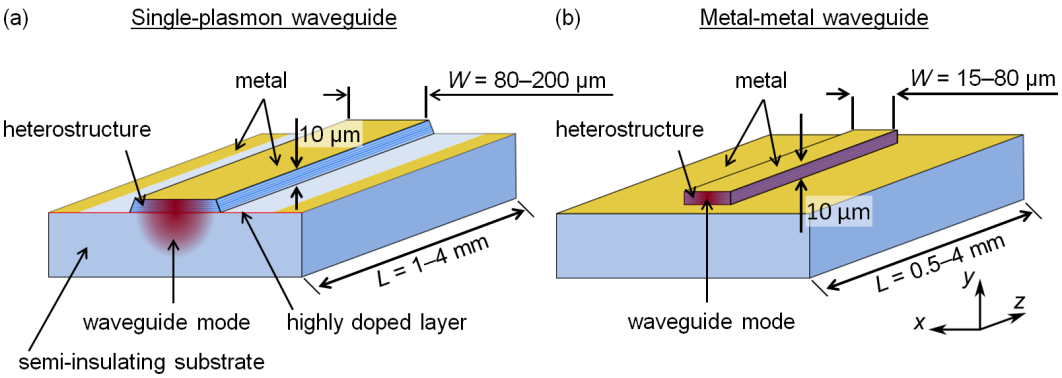

Figure 2.3: Schematic diagram of (a) the single-plasmon and (b) the metal-metal waveguide.

indexes of the active region and the substrate are similar. Therefore, semi-insulating (i.e. undoped) substrates are employed to avoid losses due to free carriers. The reduced overlap of the waveguide mode with the active region can be expressed in terms of the confinement factor Γ, which may be defined as

$$\Gamma = \frac{\int_{\mathrm{AR}} |E_y|^2 dA}{\int |E_y|^2 dA} \,. \tag{2.7}$$

The nominator represents the fraction of the waveguide mode that overlaps with the active region (AR) and the denominator the total power of the mode. Only the y-component of the electric field is taken into account, since radiative intersubband transitions dictate a vertical (y-direction) polarization of the waveguide mode, which is therefore similar to the well-known transverse-magnetic (TM) modes in planar waveguides. The confinement factors of single-plasmon waveguides typically amount to only about 30%. The typical width of a ridge based on the single-plasmon waveguide ranges between 80 and 200 µm. For narrower waveguides, the waveguide mode is pushed further into the substrate so that the confinement factor is reduced. Only the zeroth-order lateral (i.e. waveguide) mode builds up for ridge widths below 200 µm, while additional lateral modes may appear for wider waveguides.

The height of the waveguides is determined by the thickness of the semiconductor heterostructure and amounts to usually 10 µm. For single-plasmon waveguides with lower heights, the waveguide mode is further pushed into the substrate so that the confinement factor is reduced, while for metal-metal waveguides with lower heights than 10 µm, the waveguide losses are usually increased. Conversely, waveguides with larger heights would be beneficial in terms of confinement factor and losses, but their fabrication would require a thicker semiconductor heterostructure. Since the reliable growth of heterostructures with the typical thicknesses of 10 µm is already very challenging and takes 12–18 hours, the effort to further increase the thickness is not justified by the expected benefit.

The front and back facets of the most basic ridge-type THz QCL represent the mirrors of a Fabry-Pérot resonator. Typically, multiple, equally spaced frequency modes are obtained for this kind of resonator. Since the waveguide mode penetrates into the substrate, the facets are defined via cleaving so that the facet of the heterostructure lies in the same plane as the facet of the substrate. The fabrication of THz QCLs is described in more detail in section 3.1.

Figure 2.3(b) shows a schematic diagram of a ridge-type QCL based on the metal-metal waveguide. The active region is limited at the top and bottom by metal so that the waveguide mode is strongly confined to a sub-wavelength size. Since metals are highly reflective in the THz range, the waveguide mode penetrates only little into the metal layers so that the losses by free carriers are still quite low. The confinement factor is close to one even for ridge widths as low as 15 to 20 µm. For narrower ridges, a significant fraction of the waveguide mode leaks out of the sides of the waveguides so that the confinement factor is reduced. Higher-order lateral modes build up for ridge widths already above 15 to 20 µm, unless special techniques such as side absorbers are employed [61, 62]. The simplest type of resonator for THz QCLs with metal-metal waveguides is also the Fabry-Pérot type. In addition to cleaving, it can also be defined by dry-etching.

Apart from the Fabry-Pérot resonator, there are many other types of resonators employed for THz QCLs. First, there are additional resonator types based on the ridge geometry. For example, periodic structures may be applied to the ridge, giving rise to a distributed-feedback grating [4, 63]. This grating may be employed to obtain single-mode operation or to enhance the outcoupling of the generated radiation. A further technique to obtain single-mode emission is to separate the single ridge into two parts so that two longitudinally coupled Fabry-Pérot resonators are obtained [64, 65]. In addition to the modification of the ridge with a strictly periodic grating, quasi-periodic and graded periodic structures have been demonstrated, which can lead for example to enhanced side-mode suppression for single-mode operation [66, 67]. Apart from resonators based on the ridge geometry, THz QCLs with other types of resonators have been demonstrated. Examples are ring and disk resonators as well as photonic crystals [68–70].

THz QCLs with single-plasmon and metal-metal waveguides differ in their typical operating parameters. The low confinement factors of single-plasmon waveguides amounting to typically about 30% generally lead to higher threshold current densities and thus to larger excess heat. However, the large penetration depth into the substrate also has the advantage that it leads to an emission with good directionality and outcoupling efficiency. Narrow ridges with widths of about 80 µm are usually preferred for continuous-wave operation to limit excess heat, although they have the disadvantage of a further reduced confinement factor. In case of metal-metal waveguides, the confinement factor is also reduced for narrow ridges, but this occurs only—as already mentioned—for widths below 15 to 20 µm. The strong sub-wavelength confinement in metal-metal waveguides leads to substantially increased facet reflectivities and to an emission with a large divergence [71]. Excessive fields at the top metal edge of the front facet even lead to radiation directed backwards [72]. The high facet reflectivities enable lasing from short ridges, but impede high-power emission for long ones.

The recent records for high-temperature operation have all been realized by employing metal-metal waveguides, which shows that these waveguides are favorable for high-temperature operation [73–77]. The highest reported operating temperatures amount to 129 K for continuous-wave and about 200 K for pulsed mode [3, 4]. The main reasons for this superior performance of metal-metal waveguides are probably the high confinement factor and facet reflectivities, which can result in lower threshold current densities. In addition, ridges based on metal-metal waveguides can be made short and narrow, thus minimizing the total excess heat, which determines the active-region temperature in thermal equilibrium along with the thermal conductances of the employed materials. The usually inferior maximum operating temperatures of single-plasmon waveguides can in part be compensated by employing carefully designed active regions for low power dissipation and high optical gain [31]. In fact, QCLs based on single-plasmon waveguides were successfully employed in most proof-of-principle and the first real-world applications, which are enabled by their rather simple fabrication and their good beam profile [7, 20, 78, 79].

3 Technological and experimental methods

This chapter addresses the technological and experimental methods that were employed to obtain the results presented in this work. Section 3.1 covers the growth of the active region of THz QCLs, the lithographic processes for their fabrication, the mounting of a QCL chip on a heat spreader (submount), and the wire bonding to provide the electrical injection and extraction. Section 3.2 introduces the systems employed to cool the THz QCLs to temperatures usually well below 200 K. In section 3.3, the experimental methods to determine the output power, the far-field distribution, and the electrical characteristics are described. Finally, section 3.4 provides an introduction to Fourier transform spectrometers, which are employed to determine the emission spectra of THz QCLs.

3.1 Growth, fabrication, and mounting of terahertz quantum-cascade lasers

The vast majority of THz QCLs is based on the GaAs/(Al,Ga)As material system grown by molecular beam epitaxy. While there are a few demonstrations of THz QCLs based on other material systems such as (In,Ga)As/(In,Al)As, the performance of devices based on the GaAs/(Al,Ga)As material system is unmatched [80].

The challenge for the epitaxial growth of THz QCLs is the large heterostructure thickness of about 10 µm with well above 1,000 precisely defined layers. This large thickness is required to obtain low optical losses and a large confinement factor, i.e., a large overlap of the waveguide mode with the active region. Details on the waveguides are given in section 2.3. Since the growth time amounts to 12–18 hours and a control of the layer thicknesses with single-monolayer precision is required, additional measures have to be taken to compensate for the depletion of the effusion cells, through which the growth rate is reduced. This compensation is realized by a continuous in-situ thickness measurement via the optical reflectance of the epilayer, which allows for a feedback to adjust the effusion cell temperatures so that a constant growth rate is obtained [81].

Below and above the heterostructure, highly doped GaAs:Si layers are grown to provide a well-conducting ohmic contact with the subsequently evaporated gold layers. The thickness of the bottom (top) highly-doped layer typically amounts to 0.7 (0.08) µm. After growth, the wafers (or part of them) are further processed to obtain either single-plasmon or metal-metal ridge waveguides (see also section 2.3). In case of single-plasmon waveguides, the wafer can be directly processed by means of photolithography and etching. In case of metal-metal waveguides, which are not subject of this work, a wafer bonding and two substrate removal steps have to be performed first.

The fabrication of THz QCLs into ridges of single-plasmon waveguides is realized with two photolithograpic steps. In the first step, a mask defines the ridges, which are then created usually by wet chemical etching using $H_2SO_4 : H_2O_2 : H_2O$ (1 : 1 : 8). The etch depth is time-controlled and may be verified afterwards by a tactile profilometer. In a second step, the top and bottom Ni/AuGe (10/250 nm) layers are deposited via evaporation and subsequent mask lift-off. In addition, a Ti/Au layer with the same thickness is applied to the backside of the wafer to allow for soldering. Finally, Fabry-Pérot resonators are formed via cleaving. This step is also very important, since it defines the resonator length.

In order to provide for heat extraction and easy handling, the laser resonators are soldered to a gold-plated oxygen-free copper submount by means of indium, which is not only an excellent heat conductor, but also very ductile so that it prevents damage due to the different thermal expansion coefficients of the soldered materials. The electrical connection is realized by gold wire bonding. Not only the top, but also the bottom contact needs to be electrically connected by means of gold wire bonds, since the substrate is semi-insulating.

3.2 Cooling systems for temperatures below 200 K

Since THz QCLs operate only at temperatures below 200 K, cooling systems that can achieve these low temperatures are required. Figure 3.1 shows the setup of the two cooling systems that have been used to investigate THz QCLs. The helium flow cryostat (Oxford Instruments Optistat-CF-V) depicted in Fig. 3.1(a) can achieve temperatures down to about 4.2 K, the boiling point of liquid helium. In contrast to bath cryostats, in which the sample to be cooled is immersed into liquid helium, the sample is mounted such that it is in thermal contact with the cryostat cold finger, through which the liquid helium flows. The thermal insulation is realized by evacuating the chamber in which the cold finger and the sample are located. In order to further reduce the heat input, a differentially cooled radiation shield is employed. A temperature sensor and a heating resistor are already integrated in the cold finger of the Optistat-CF-V cryostat, which are employed to stabilize the temperature with a feedback control loop realized by means of a temperature controller (Oxford Instruments ITC 502 or Stanford Research Systems CTC 100). For the flow cryostat, mostly optical windows from high-density polyethylene (HD-PE) with a diameter of 42 mm are employed. Since the QCL is located at a distance of about 7 mm from the window, radiation with divergence angles of up to 58° can be coupled out of the cryostat. In addition, windows made of poly-4-methylpentene-1 (also known under the trade name TPX) or of polypropylene foil can be used. The clear aperture of the window made of TPX is the same as the one made of HD-PE, but the polypropylene foil window has a smaller aperture of only 32 mm, since the foil is attached to a metal ring with that inner diameter.

Low temperatures can also be obtained with cryogen-free mechanical coolers such as pulse-tube refrigerators. Here, a cooler based on an inverse Stirling motor is used (Ricor K535), which will therefore be referred to as Stirling cooler. It achieves temperatures down to 35 K. At the same time, it is very compact and therefore portable. The Stirling cooler only requires a conventional wall socket due to the low power consumption of below 400 W. Figure 3.1(b) shows the setup of the Stirling cooler. The cold finger, its extensions, and the

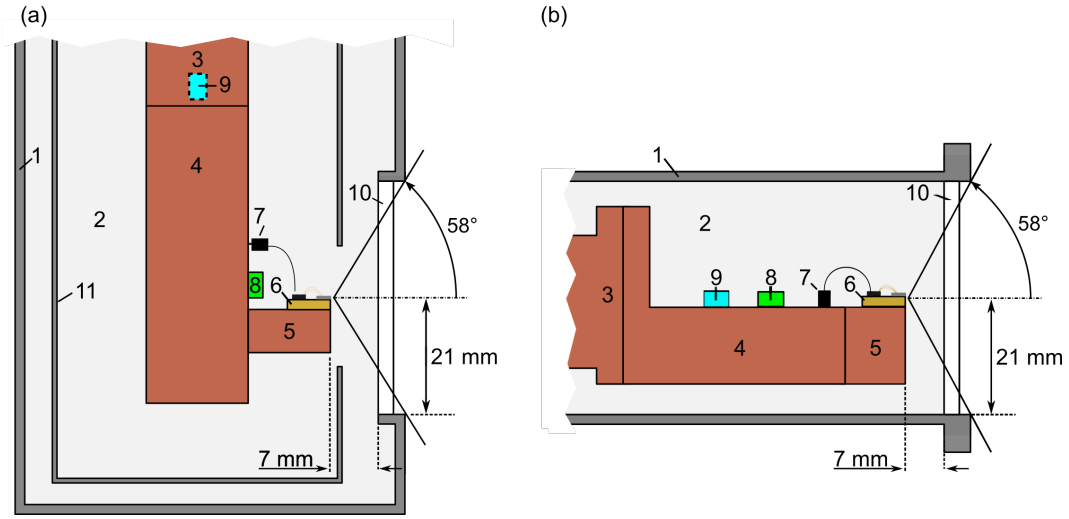

Figure 3.1: Setup of (a) the helium flow cryostat and (b) the Stirling cooler. 1: Chamber housing; 2: evacuated chamber; 3: cold finger; 4: first cold finger extension; 5: second cold finger extension; 6: QCL submount; 7: electrical connector; 8: temperature sensor; 9: heating resistor; 10: optical window; 11: radiation shield.

THz QCL itself are located in an evacuated chamber so that the cooled parts are thermally insulated from the environment. The thermal stabilization is realized via a temperature sensor and a heater, which are operated by a temperature controller (Oxford Instruments ITC Mercury). The same windows as for the helium flow cryostat can be used. The distance of the QCL from the window is usually 7 mm, the same value as for the flow cryostat.

The Stirling cooler is very convenient to use, since it does not require cryogenic fluids. However, the lowest achievable temperature amounts to only about 35 K, which is significantly higher than the temperature of 4.2 K that can be obtained with the helium flow cryostat. In addition, the heat that can be dissipated by the Stirling cooler is rather small at low temperatures, while the cooling power of the flow cryostat is quite high at all temperatures. For these reasons, the helium flow cryostat is better suited for the operation of THz QCLs at rather low temperatures, while the Stirling cooler is often preferred for THz QCLs that have high output powers even at elevated temperatures and for practical applications, for which a compact and portable cooling system is required.

3.3 Measurements of optical power, far-field distribution, and electrical characteristics

There are only a few detectors on the market that can reliably measure the absolute power of terahertz radiation, since only recently a metrological standard that is traceable to SI units has been established for the THz range [82]. The most frequently used detectors for the

absolute power measurement in the THz range rely on pyroelectric sensors. The impinging radiation is absorbed by means of a low-reflectance layer so that a pyroelectric crystal is heated, through which a charge separation takes place and a voltage can be measured. Since relaxation mechanisms result in a leveling to zero of the voltage for time-independent irradiation, only time-varying radiation can be measured with a pyroelectric sensor. Hence, an optical chopper is required to measure continuous-wave radiation. The crystal with the highest pyroelectric constant known to date is deuterated triglycene sulfate, which is therefore employed for the most sensitive detectors.

For the measurements of the absolute power presented in this thesis, a detector head with a pyroelectric sensor (LaserProbe RkP-575/RF) connected to a compatible radiometer (LaserProbe Rk-5710) was employed. In early 2018, the detector head along with the radiometer was calibrated for the THz frequency range by the German national metrology institute (Physikalisch-Technische Bundesanstalt). The calibration showed that the detector underestimated the power of the radiation by about 20%.

The setup for the power measurement of THz QCLs in pulsed operation is shown in Fig. 3.2(a). The radiation from the QCL is collected by means of a light pipe with an inner diameter of 11 mm, which directs the impinging radiation toward the absorption plates of the pyroelectric sensor. This configuration allows for the collection of radiation within a cone with a divergence angle of 33°. Since most THz QCLs with single-plasmon waveguides have smaller divergence angles than 33°, the collection efficiency is close to 1. Losses may appear through a limited reflectivity of the inner wall of the light pipe and incomplete absorption of radiation by the absorption plates. In addition, losses by atmospheric absorption may occur.

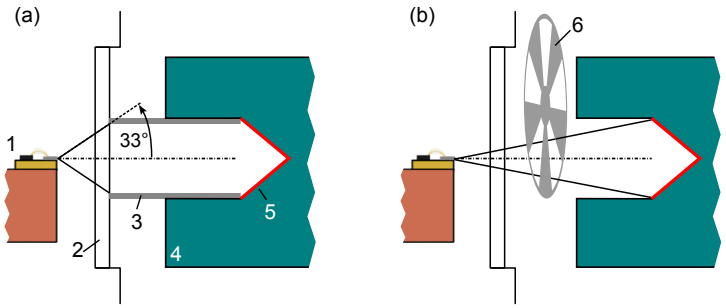

Figure 3.2: (a) Setup for power measurements of THz QCLs in pulsed operation. 1: Mounted QCL on cold finger; 2: optical window; 3: aluminum light pipe; 4: LaserProbe RkP-575/RF detector head; 5: absorber plates. (b) Setup for power measurements of THz QCLs in continuous-wave operation. 6: Optical chopper.

Figure 3.2(b) shows the setup of the power measurements for continuous-wave operation. Since an optical chopper is required, the light pipe cannot be used, and the collection efficiency is reduced by a factor of about 3. The collection efficiency for this setup can be

determined by operating the QCL in pulsed mode and comparing the measured power with the value obtained with the configuration shown in Figure 3.2(a).

The power is usually measured along with the voltage as a function of the current applied to the THz QCL. For pulsed measurements, the Avtech AV-107C-B current pulse generator is employed. For measurements in continuous-wave mode, the Keithley 2650A source measure unit is used.

Figure 3.3 shows the setup employed for the measurement of the far-field distribution. A single-pixel pyroelectric sensor with a diameter of 2 mm is mounted in such a way that it can be moved within a plane by two motorized linear translation stages. For the measurement of the far-field distribution, the QCL is electrically chopped with a frequency of 30 Hz, and the sensor signal is retrieved with a lock-in technique. The plane is scanned usually in 2 mm steps. The angular resolution can be increased by placing the sensor further away from the THz QCL, albeit at the cost of longer measurement times. Since the far-field distribution is measured within a plane, the angular element is reduced for increasing angles, which is corrected during data analysis. In addition, the sensitivity change of the pyroelectric sensor as a function of the angle of incidence has been investigated and found to be negligible for the relevant range of angles.

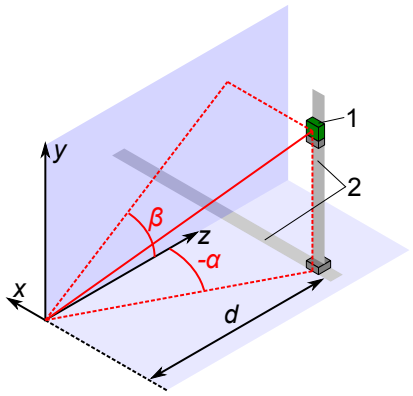

Figure 3.3: Setup for the measurement of the far-field distribution. The optical axis is collinear to the z-axis, and the THz QCL is located at the origin of the coordinate system. 1: Single-pixel pyroelectric sensor; 2: motorized linear translation stages.

3.4 Fourier transform spectrometer

Fourier transform spectroscopy is an established method to measure the emission spectrum of a radiation source or the absorption spectrum of a sample under investigation. Figure 3.4 shows a simplified setup of a Fourier transform spectrometer, which consists mainly of a Michelson interferometer. In order to measure an emission or transmission spectrum, one of the interferometer mirrors is moved continuously so that the intensity of the radiation impinging on the detector is modulated periodically due to interference. The detector signal

as a function of the path length difference between the two mirrors is usually referred to as interferogram. The corresponding spectrum is obtained through a numerical Fourier transformation of the interferogram performed by the spectrometer computer, and its resolution is determined by the maximal path length difference.

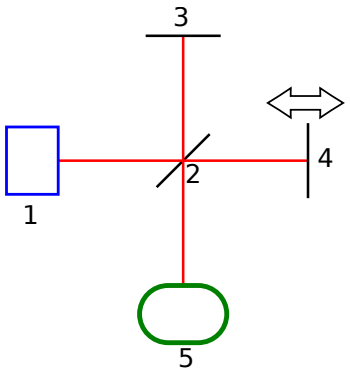

Figure 3.4: Simplified setup of a Fourier transform spectrometer. 1: Source; 2: beam splitter; 3: fixed mirror; 4: movable mirror; 5: detector.

Historically, Fourier transform spectrometers have been claimed to exhibit two fundamental advantages with respect to grating spectrometers. The first is usually referred to as Fellgett's or the multiplex advantage, which represents the spectrometer's capability to obtain spectral information for all frequencies simultaneously. While a grating spectrometer delivers information about subsequent frequencies at consecutive points in time of a measurement, a Fourier transform spectrometer has already acquired the information for all frequencies shortly after the measurement started, but with a low resolution. As the measurement continues and thus the path length difference is increased, the resolution is increased. When using identical detectors, the multiplex advantage of a Fourier transform spectrometer should lead to a signal-to-noise ratio that is by the square root of the resolution higher than for a measurement with a grating spectrometer. However, the advent of powerful detectors based on charge-coupled devices (CCDs) resulted in a dominance of grating spectrometers in the ultra-violet, visible, and near-infrared spectral range, because their high sensitivity cannot be exploited with Fourier transform spectrometers [83]. The reason is the working principle of the Fourier transform spectrometer that relies on the measurement of rather fast intensity modulations, for which CCDs are not suitable. In contrast, multiple-pixel CCDs employed as detectors for grating spectrometers also give rise to a frequency-multiplexed measurement, and their quantum efficiencies of up to almost 100% are unchallenged. Since high-sensitivity CCDs are not available in the mid- and far-infrared region, Fourier transform spectrometers are very competitive in that frequency range.

A second fundamental advantage of Fourier transform spectrometers is usually referred to as Jaquinot's or throughput advantage. The resolution of grating spectrometers depends on the width of the employed slit apertures, while circular apertures are used for Fourier transform spectrometers. Consequently, the optical throughput of a Fourier transform spectrometer is usually higher than for grating spectrometers. This advantage scales as the

frequency squared and may lead to higher sensitivities. However, this advantage again does not apply if CCDs are employed for the grating spectrometer due to their high efficiencies.

The general trading rule between sensitivity and resolution is also valid for Fourier transform spectroscopy. In this context, it is important to consider that the radiation is parallelized in order to be suitable for the Michelson interferometer and afterwards focused onto a suitable detector. Since insufficient parallelization leads to a fine structure in the plane of the detector, the required intensity modulations may be compromised and thus also the spectral resolution. Consequently, high-resolution spectrometers are equipped with a so-called Jaquinot stop, i.e., an aperture that ensures sufficient parallelization.

The frequency scale of a spectrum obtained with Fourier transform spectroscopy is determined by the values of the path length difference. This path length difference is usually measured by means of a frequency-stabilized HeNe gas laser. This laser is also coupled into the interferometer so that intensity modulations can be measured with a dedicated detector. Since the laser frequency is exactly known, the frequency scale for the radiation under investigation is automatically calibrated.

In the framework of this thesis, two different Fourier transform spectrometers have been used. The first (Bruker IFS120HR) features a maximal spectral resolution of 0.105 GHz, while the second (Bruker IFS66v) has a maximal resolution of 3.6 GHz. Both spectrometers can be fully evacuated to avoid absorption by water vapor.

4 Multiple lobes in the far-field distribution of terahertz quantum-cascade lasers

4.1 Introduction

Many applications relying on THz QCLs benefit from or even require a far-field distribution of the emission intensity which is as close as possible to a Gaussian profile. However, multiple lobes have frequently been reported for THz QCLs both with metal-metal and single-plasmon waveguides. In the case of QCLs with metal-metal waveguides, it has been shown that the modulations in the far-field distribution appear due to interference of the radiation emitted from the front facet with diffracted radiation from the back facet [84, 85]. For single-plasmon waveguides, there are a number of different mechanisms that have been discussed in the literature. A similar effect as for metal-metal waveguides [86] or an aperture-like diffraction effect due to the wavelength-sized waveguide mode [20] may be the origin. Further explanations include the presence of the substrate [87, 88] and reflections within or between cryostat windows [87]. The diversity of the suggested explanations in the literature clearly shows that a thorough investigation of the phenomenon is lacking, in particular for single-plasmon waveguides.

In the experimental investigations presented in this chapter, two different types of intensity modulations have been found as shown by the example displayed in Fig. 4.1. The modulations located in the upper half space (positive angles of β), which will be referred to as type-I modulations, have a horizontal shape. The intensity modulations in the lower half space have a semi-circular shape and are referred to as type-II modulations. Several possible origins of the modulations are investigated. The most important one is radiation reflected on parts of the cryogenic operation environment including the optical windows, which subsequently interferes with the radiation emitted directly from the QCL. Therefore, modeling techniques to reproduce the modulations due to specular reflections and interference are introduced in section 4.2. Then, after a brief description of the investigated QCLs in section 4.3, the experimental results for the type-I and type-II modulations are presented and compared to the results of the model calculations in sections 4.4 and 4.5, respectively. The suppression of the modulations by using absorptive material and a special geometry is demonstrated in section 4.5.3. The achieved results are summarized in section 4.6

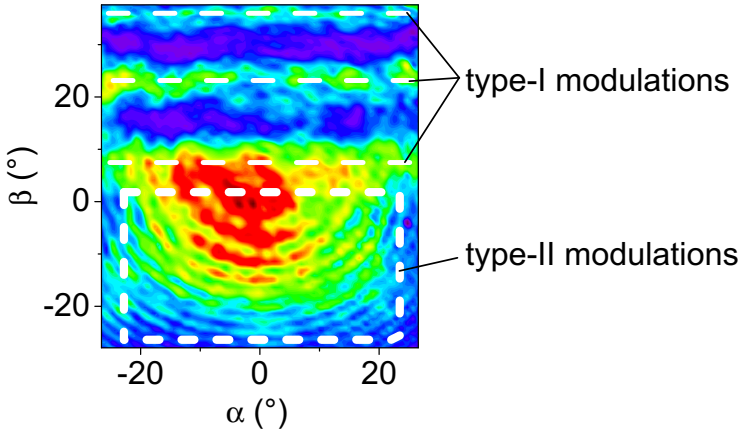

Figure 4.1: Far-field distribution of a single-mode QCL emitting at 2.5 THz measured at a distance of $d = 100$ mm. Two types of intensity modulations can be identified, type-I and type-II modulations.

4.2 Modeling reflections and interference of radiation emitted by a quantum-cascade laser

4.2.1 Geometrical-optics-based and mirror source-based modeling of reflections and interference

The simplest way to address specular reflections is to consider, in the framework of geometrical optics, a ray impinging on a mirror as illustrated in Fig. 4.2(a). Most often, the ray represents a plane wave that propagates in the same direction as the ray, while the wavefronts are perpendicular to the propagation direction. Using this approach, the phase of the reflected plane wave can be easily calculated by considering the path length that the ray has traveled. This technique is used, for example, to calculate the interference fringes of thin films by taking into account the path length difference of two or more rays. As also illustrated in Fig. 4.2(a), an alternative way to calculate the phase (and amplitude) of a reflected wave is to consider the radiation from a virtual mirror source positioned at the same distance a as the original source on the other side of the mirror. In the present case of a plane wave, the radiation field of the mirror source can be deduced from the radiation field of the original source by a geometric translation and rotation of the radiation field. In order to obtain the radiation field of the mirror source from an arbitrary radiation field of the real source, a general mirror transformation has to be performed. Both the geometrical-optics and mirror source approach are also valid for a spherical wave as shown in Fig. 4.2(b). The green and blue arrows represent rays originating from the source and traveling toward the mirror at different angles, where they are reflected. Similarly to the case of plane waves, the reflected rays can be equivalently considered as originating from the mirror source.

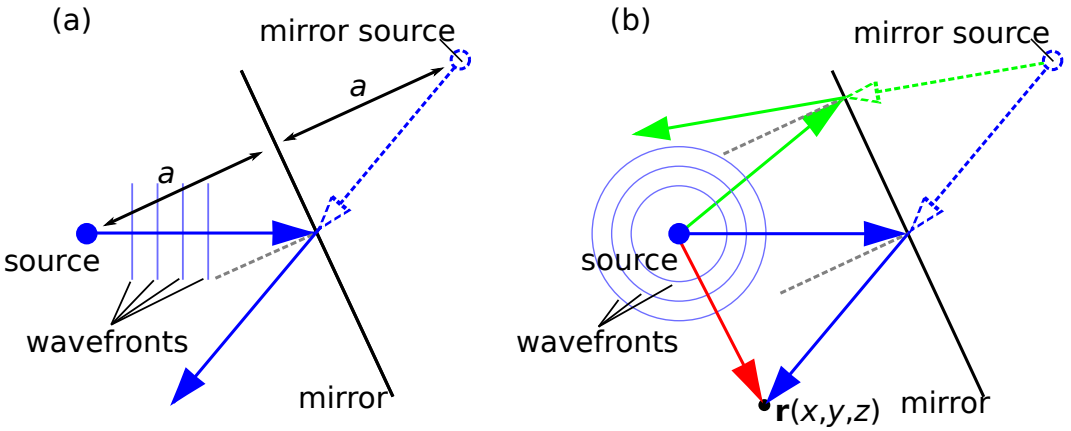

Figure 4.2: (a) A plane wave, which is emitted from a source, is represented by a ray that travels toward a mirror and is specularly reflected (solid arrows). The reflected radiation can also be thought of as originating from a mirror source and traveling toward the position of the mirror (dashed line). The mirror source is located at the distance a behind the mirror, which is equal to the distance of the real source in front of the mirror. (b) Geometrical-optics (solid arrows) and mirror source model (dashed arrows) of specular reflections assuming that the source emits spherical waves. At every point $\mathbf{r}(x,y,z)$, the reflected radiation (illustrated by the blue arrow) interferes with radiation having directly traveled from the source (red arrow).

More generally, the geometrical-optics approach is only valid if the phase of the wave can be correctly inferred from the path originating from the source to a relevant point in space. To investigate under which condition this is the case, consider a wavefront of a propagating wave. A local wave vector can be assigned to every point of that wavefront, which represents the local propagation direction, i.e. the direction, at which the rate of change of the phase is maximum. Since the wavefronts are surfaces of equal phase, i.e. $\phi(\mathbf{r}) = \text{constant}$, and the direction of the maximum phase change is the gradient vector of the phase, i.e. $\nabla\phi(\mathbf{r})$, the local propagation direction is always perpendicular to the wavefront. Therefore, if a ray originating from the source is perpendicular to the wavefronts, it is also always parallel to the local propagation direction at any point of the wave in the considered direction. In this case, the phase can correctly be inferred from the corresponding path length, which cannot be expected in the general case of arbitrarily shaped wavefronts, which may intersect some rays by an angle different from 90°. This restriction for the geometrical-optics approach does not apply to the mirror source-based model, since explicit equations for the waves can be used, which may be in principle arbitrarily complex.

Furthermore, the mirror source approach may be more convenient to use than the geometrical-optics approach. Consider a point in space $\mathbf{r}(x,y,z)$ as shown in Fig. 4.2(b), at which radiation directly emitted from the source and radiation from the reflection at the mirror are superimposed. To calculate the intensity due to interference at this point, the path

length of the ray traveling directly to the point $\mathbf{r}(x,y,z)$ (red arrow) and the path length of a ray traveling to that point via the reflection on the mirror (blue arrow) have to be determined. Afterwards, the resulting intensity has to be calculated from the path length difference, taking also into account the intensities as a function of the path length, and, in a more general case, also the intensity dependence as a function of the emission direction. In contrast, considering the radiation field emitted from a mirror source and its superposition with the directly emitted radiation can be more convenient in some cases. The transformation to obtain the radiation field of the mirror source from the original radiation field includes a translation, a possible phase change, and sometimes a transformation of the emission direction, which is, for instance, the case for a plane wave as clearly seen in Fig. 4.2(a). The latter is not necessary in the case of a pure spherical wave due to its isotropy or for certain mirror configurations as will become clear in sections 4.4 and 4.5.

To give an example of how to calculate the intensity of an interference pattern, let $\mathbf{E}(\mathbf{r}-\mathbf{r}_0)$ be the radiation field emitted from a source at the point $\mathbf{r}_0$ and $\tilde{\mathbf{E}}(\mathbf{r}-\mathbf{r}_\mathrm{M})$ the appropriately transformed radiation field of the mirror source centered at the position $\mathbf{r}_\mathrm{M}$. If a mirror reflectivity of 100% is assumed, both fields have equal intensities so that the resulting intensity can be calculated by

$$I(\mathbf{r}) = |\mathbf{E}(\mathbf{r}-\mathbf{r}_0)+\tilde{\mathbf{E}}(\mathbf{r}-\mathbf{r}_\mathrm{M})|^2 \,. \tag{4.1}$$

If $\mathbf{E}$ and $\tilde{\mathbf{E}}$ are collinear, their sum represents a coherent superposition. Taking the absolute square yields the intensity due to interference of the two radiation fields.

In the remainder of this chapter, this general example is adapted to the specific cases under investigation. The geometrical-optics-based model is used for illustration purposes and the mirror source-based model for the numerical calculation of the interference patterns.

4.2.2 Model for the radiation field

In order to mathematically describe the radiation field of a QCL, it seems natural, at first glance, to assume a Gaussian beam. However, the Gaussian beam, which is a solution of the paraxial Helmholtz equation, cannot correctly describe radiation with a divergence angle exceeding 30° as it is the case for typical QCLs. The divergence angle is defined as the angle for which the intensity has decreased by a factor of e^2 as compared to its value at 0°. Due to the restriction of the Gaussian beam to small divergence angles, a spherical wave should be a better approximation to the divergent radiation of a QCL. However, the spherical wave totally lacks directionality, which radiation from typical QCLs clearly exhibits. Therefore, a combination of both models is used. Neglecting the polarization, the field strength of the Gaussian beam with a divergence angle θ is given by [89]

$$E_{\mathrm{G},\theta}(x,y,z) = \frac{A_0}{W_\theta(z)}\exp\left[-\frac{\rho^2}{W_\theta^2(z)} - i\left(kz + k\frac{\rho^2}{2R(z)} - \zeta(z)\right)\right] , \tag{4.2}$$

where

$$W_\theta(z) = \sqrt{z^2\theta^2 + \frac{\lambda^2}{\pi^2\theta^2}}\,, \tag{4.3}$$

$$R(z) = z\left[1+\left(\frac{z_0}{z}\right)^2\right]\,, \tag{4.4}$$

$$\zeta(z) = \tan^{-1}\left(\frac{z}{z_0}\right)\,, \tag{4.5}$$

$$\rho = \sqrt{x^2+y^2}\,, \tag{4.6}$$

$$k = \frac{2\pi}{\lambda}\,. \tag{4.7}$$

Here, A_0 represents a normalization constant, W_θ the beam width, λ the wavelength, R the wavefront radius of curvature, z_0 the Rayleigh range, ζ the Gouy phase, ρ the distance from the z-axis, and k the wavenumber.

The field strength of a spherical wave, in contrast, is described by the equation

$$E_\mathrm{s}(x,y,z) = \frac{A_0}{r}\exp[-i\,k\,r]\,, \tag{4.8}$$

where $r = \sqrt{\rho^2+z^2}$. The polarization is neglected. For the combined model, the amplitude and lateral intensity distribution from Eq. (4.2) are used, while the part responsible for the phase is taken from the expression of the spherical wave. Assuming that the front facet is situated at the origin of the coordinate system, the complex amplitude of the emitted radiation at a point $\mathbf{r}(x,y,z)$ is given by

$$\mathbf{E}_\theta(x,y,z) = \frac{A_0}{W_\theta(z)}\exp\left[-\frac{\rho^2}{W_\theta^2(z)} - i\,k\,r\right]\,, \tag{4.9}$$

The parameter θ denotes the divergence angle in radians, which was set to 0.59 (34°) for all calculations. A beam with this divergence angle exhibits an angular full width at half maximum of 40°, which is defined as twice the angle, for which the intensity has decreased by a factor of 2 as compared to its value at 0°.

4.3 Active regions and emission spectra of the employed quantum-cascade lasers

Before the presentation of the intensity modulations in the two subsequent sections, the investigated QCLs will be briefly described. All QCLs are processed into single-plasmon waveguides and Fabry-Pérot resonators. We have investigated two sets of QCLs at two different frequencies.

The first set of QCLs is made from wafer M4.2650. The active region is very similar to the design presented in Ref. [42], which is based on the hybrid design introduced in

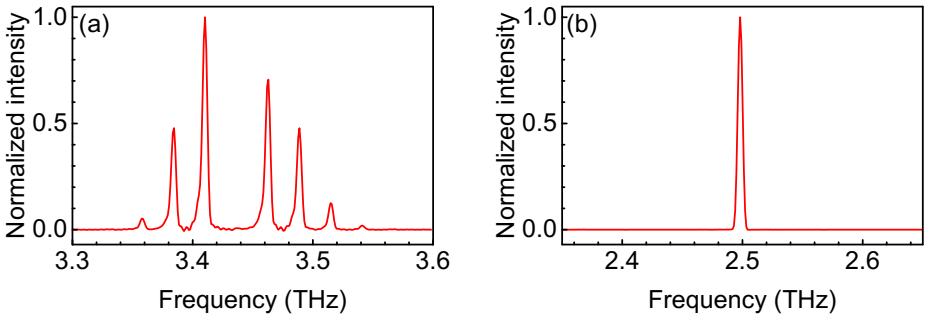

Figure 4.3: (a) Emission spectrum of a QCL with a resonator length of about 1.5 mm from wafer M4.2650. (b) Emission spectrum of a QCL fabricated from wafer M4.2135 with the same resonator length as in (a) [90, 91].

section 2.2.2 with low thermal dissipation. Figure 4.3(a) shows an exemplary emission spectrum of a QCL from this wafer with a resonator length of about 1.5 mm. The emission spectrum contains several modes. At a frequency of about 3.44 THz, one Fabry-Pérot mode is missing, which is most likely due to the nonlinear character of the mode competition present in multi-mode lasers.

The second set of QCLs is taken from wafer M4.2135. This wafer is based on the bound-to-continuum design for emission frequencies of 2.9 THz described in Ref. [90], but the quantum well thicknesses have been increased to reduce the emission frequency to 2.5 THz. Figure 4.3(b) shows an exemplary emission spectrum of a QCL from wafer M4.2135 with a resonator length of about 1.5 mm. The QCLs from this wafer emit only a single mode for resonator lengths that are not too large, because the gain profile is so narrow that only one Fabry-Pérot mode can build up.

4.4 Type-I intensity modulations

In order to investigate the origin of the type-I intensity modulations, Figs. 4.4(a)–4.4(d) show the far-field distributions of four different QCLs. The investigated QCLs are mounted in two different ways, as illustrated in the insets in the upper right corners of the figures. The QCL chips, whose far-field distributions are shown in Figs. 4.4(a) and 4.4(b), are mounted with a finite distance to the submount edge, leaving an exposed horizontal metal surface. These QCLs have a far-field distribution exhibiting the type-I modulations. In contrast, the QCL chips, whose far-field distributions are shown in Figs. 4.4(c) and 4.4(d), are mounted on the submount edge, for which the type-I modulations are absent. It can be concluded that the uncovered surface of the metal submount in front of the QCLs in Figs. 4.4(a) and 4.4(b) is responsible for the type-I modulations.

Since the submount is made from gold-plated copper, radiation emitted from the QCL toward the submount can be reflected on the uncovered surface. As Fig. 4.5 illustrates, the

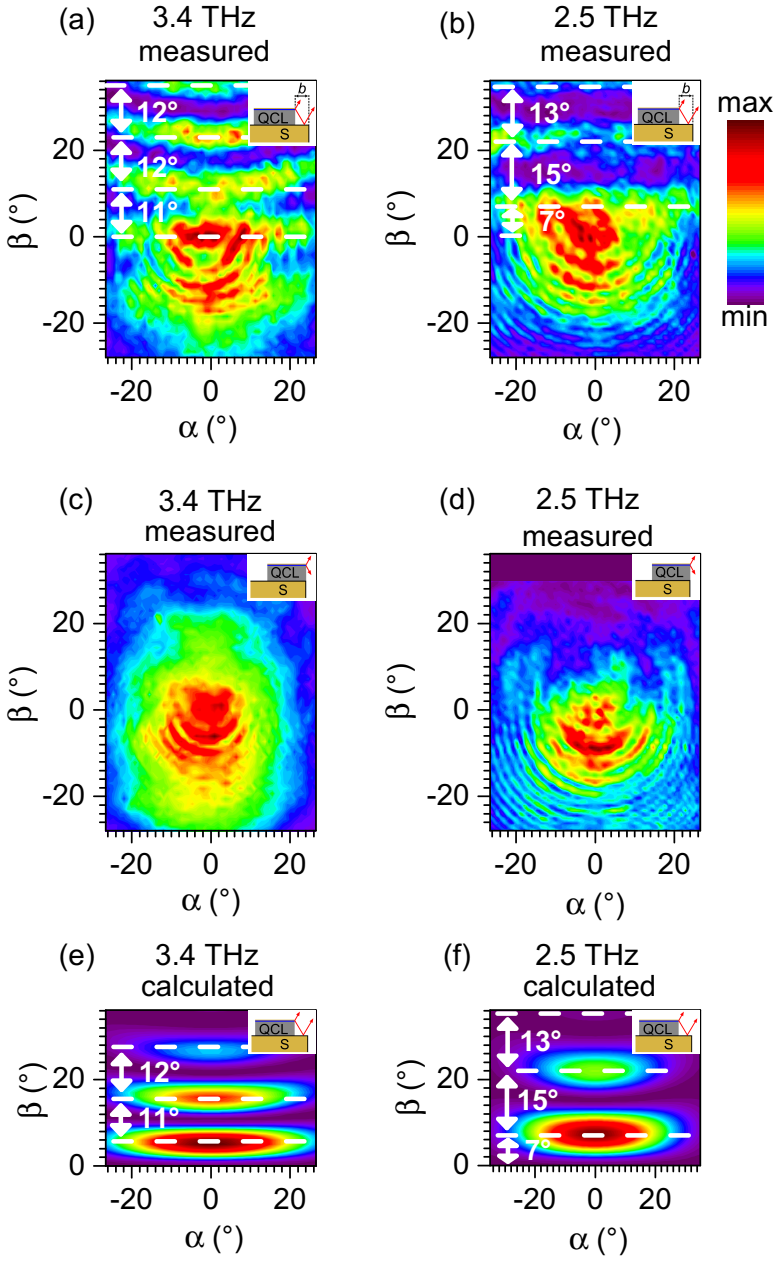

Figure 4.4: (a)–(d) Measured far-field distributions of QCLs with two different emission frequencies indicated above each panel. The QCLs in (a) and (b) are mounted with a distance of $b = 490$ and 680 µm from the submount edge, respectively, as illustrated in the insets. In contrast, the QCLs in (c) and (d) are mounted at the submount edge, i.e., $b = 0$ µm, as also illustrated in the insets. The 3.4-THz QCLs in (a) and (c) have a width of 120 µm and the 2.5-THz QCLs in (b) and (d) have a width of 150 µm. The lengths of the QCLs amount to 1,432 µm in (a), 1,324 µm in (b), 1,310 µm in (c), and 1,338 µm in (d). (e) and (f) display the calculated far-field distributions based on the interference of the radiation reflected at the submount surface with directly emitted radiation as illustrated in the insets.

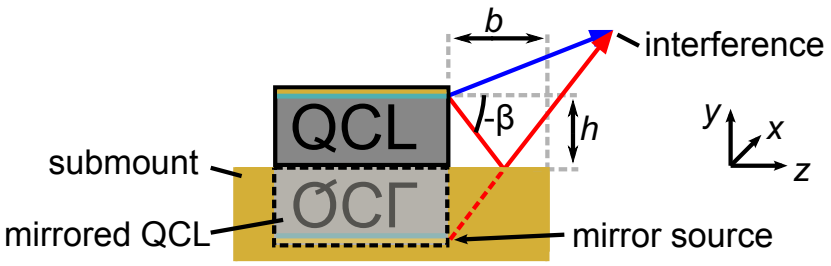

Figure 4.5: Schematic of a QCL mounted at a distance b from the submount edge illustrating the proposed interference mechanism for the type-I modulations, displayed in the framework of the geometrical-optics-based and mirror source-based model. The source of the emitted radiation is assumed to be located at a height h above the submount surface. Radiation emitted toward the lower half space can be reflected at the exposed surface and interfere with the radiation emitted toward the upper half space.

radiation reflected at the submount toward the upper half space can interfere with the radiation directly emitted from the QCL toward the upper half space. Since the path length difference between the directly emitted and the reflected radiation varies as a function of y (or, equivalently, as a function of the angle β with the x-axis in the far field), alternating constructive and destructive interferences develop, leading to the type-I intensity modulations. Having described the assumed mechanism for the modulations using geometrical optics, the calculation of the interference pattern will be performed applying the method based on the mirror source for the reasons outlined in section 4.2.

For the calculation of the interference patterns, the position of the center of the radiation field is an important parameter. This center corresponds to the position of the source in the geometrical-optics model. Determining the exact position of this center is not straightforward, because in QCLs with single-plasmon waveguides the laser mode is not fully confined to the active region, but extends significantly into the substrate. Therefore, the center of the emission is not necessarily located at the vertical position of the active region as depicted in Fig. 4.5 for illustration purposes, but may also be located somewhat lower toward the substrate. Since this position depends on the details of the waveguide mode, it is considered to be a free parameter h for the modeling of the reflections and defined as the distance between the surface of the submount and the center position of the emitted radiation field (cf. Fig. 4.5). To calculate the resulting intensity modulations, the origin of the coordinate system is positioned at the center of the radiation field, and the mirror source is positioned at $y = -2h$, i.e., at a distance h from the submount surface, which is assumed to act as a mirror with 100% reflectivity. The intensity distribution in the x-y-plane at a horizontal distance d (along the z-axis) from the mirror is then given by

$$I_{\theta,v}(x,y,d) = I_0 |F_{\theta,v}(x,y,d) + F_{\theta,v}(x,y+2h,d)\exp(-i\phi)|^2 \,, \tag{4.10}$$

where $x = d\tan(\alpha)$, and $y = d\tan(\beta)$. Since a phase change upon reflection is taken into account, $\phi = \pi$.

Figures 4.4(e) and 4.4(f) show the results of the calculations corresponding to the experimental results displayed in Figs. 4.4(a) and 4.4(b), respectively. For a best fit to the experimental results, the free parameter h is set to 240 µm in case of Fig. 4.4(e) and to 230 µm in case of Fig. 4.4(f).

Using the above-mentioned values for h, the relative positions of the intensity maxima indicated by the dashed lines in Figs. 4.4(a) and 4.4(b) are well reproduced by the calculations shown in Fig. 4.4(e) and 4.4(f). For the 3.4-THz QCL, there is an offset of about 6° along the β-direction. The fourth maximum in Fig. 4.4(e) and the third maximum in Fig. 4.4(f) counting from $\beta = 0°$ exhibit lower intensities than in the measurements. The good agreement between the measured and calculated far-field distributions suggest that, indeed, specular reflections on the submount and subsequent interference with the upward emitted radiation are responsible for the type-I intensity modulations. The deviations between the calculated and measured far-field distributions might result from the simplifications made as discussed in the following.

One simplification was made by assuming that the radiation emitted from the QCL is symmetric (cf. subsection 4.2.2), although there is an asymmetry in the β-direction as shown in Fig. 4.4(c). This simplification prevents an overly complex treatment of the emitted radiation field. Furthermore, by using the mirror source-based model, a semi-infinite mirror is implicitly assumed. Considering that the lengths of the exposed metal surfaces are only $b = 490$ and 680 µm for the 3.4- ($\lambda = 88$ µm) and 2.5-THz ($\lambda = 120$ µm) QCL, respectively, i.e., about 6 times the wavelength, an infinite mirror seems to be a rather poor approximation. However, taking into account the finite length b of the exposed metal within a geometrical-optics approach leads to contradictions with the observed far-field distributions as will be now discussed.

If a ray at $\beta = 0°$ is considered, there is no interaction with the submount surface. The same is valid for small negative values of β, until the corner of the submount blocks the radiation, as is obvious from Fig. 4.5. For the 3.4-THz QCL, this angle is $-24°$ as can be calculated from the values of h and b given earlier. The ray at this angle is reflected and has, after the reflection, an angle of about $+24°$ in the far field. This ray can interfere with the radiation emitted directly toward the upper half space. However, rays toward the lower half space with angles between 0° and $-24°$ do not hit the submount and will therefore not be reflected to become rays with positive angles between 0° and $+24°$, which could interfere with the radiation directly emitted toward the upper half space. Therefore, within the geometrical-optics-based model, no interference patterns are expected between $\beta = 0°$ and $+24°$ for the 3.4-THz QCL, which clearly disagrees with the measurements.

Apart from the deviations between the calculated and the measured distributions, the obtained values for the vertical distance of the exposed metal surface from the center of the emitted radiation h (cf. Fig 4.5) need to be discussed. The obtained values for h of 240 and 230 µm for the 3.4- and 2.5-THz QCL, respectively, correspond to distances of about 110 and 120 µm below the active region, since the height of the substrate amounts to about 350 µm. In contrast, a reasonably chosen center of the waveguide mode (inside the wave-

guide) is located only some tens of μm below the active region, as can be derived from finite-element calculations of the waveguide mode [30]. This difference may be explained by considering that the center of the field outside of the waveguide may be situated at a different location than the center of the field inside the waveguide, since the optical wavelength increases by a factor of about 3 upon outcoupling and the field inside the waveguide is vertically asymmetric. Furthermore, the asymmetry of the radiation emitted from the QCL has not been taken into account as mentioned earlier. These effects could be the origin of the difference between the observed and the expected values of h.

The above considerations hint at another approach for investigating the effects of the exposed metal surface of the submount. Since the vacuum wavelengths at 3.4 and 2.5 THz amount to 88 and 120 μm, respectively, they are on the same order as the relevant lengths for the interaction of the emitted radiation with the submount surface, i.e., h and b. Therefore, it might be necessary to consider the interaction of the near field of the emitted radiation with the submount surface. Since the near field might have non-trivially shaped wavefronts, the geometrical-optics approach as described in subsection 4.2.1 is inappropriate. Although the mirror source-based model is in principle applicable to non-trivial wavefronts, assumptions for the near field have to be made, and a correct treatment of the finite length of the exposed submount surface with the mirror source-based model is difficult as mentioned earlier. In contrast, it should be feasible to perform simulations based, for example, on the finite-element method to investigate the near- and the far-field distributions. The computational effort is not too large for finite-element simulations, because the system comprising the outcoupling facet and the submount surface has a length of less than 10 wavelengths. With this approach, also effects such as the built-up of surface plasmon polaritons on the metal surface or excessive fields can be studied.

In conclusion, the origin of the type-I intensity modulations in the far-field distribution of QCLs has been investigated. Since the type-I modulations are only present if the QCL chips are mounted with a finite distance from the submount edge, the exposed metal surface is clearly responsible for these modulations. Furthermore, the experimentally observed positions of the modulation maxima have been compared with the results of the model calculations, which assume specular reflections on the submount surface and are based on the mirror source-based model. By choosing appropriate parameters, a good agreement between the results of the calculations and the measurements was achieved. This agreement shows that specular reflections are the dominant mechanism for the type-I modulations. However, there may be a contribution of near-field effects, which can be studied using for example finite-element simulations.

4.5 Type-II intensity modulations

In this section, the type-II intensity modulations are investigated. The QCLs presented in this section are mounted on the submount edge to prevent the type-I modulations. Three different possible origins for the type-II modulations are examined, and the one responsible is clearly identified in subsection 4.5.1. In subsection 4.5.2, the identified mechanism is further analyzed.

4.5.1 Identifying the underlying mechanism

Transmittance of the cooling system window

One possible explanation for the type-II intensity modulations may be reflections within the window of the cooling system. In order to investigate this possibility, the spectral transmittance of the window was measured at several angles between 0° (normal incidence) and 40° with the Fourier transform spectrometer, using the globar as a source and a pyroelectric detector. The results of the measurements are shown in Fig. 4.6(a). At all measured angles, the transmittance is modulated with a spectral period of about 1.5 THz as expected for the foil window with a thickness of only 75 µm and a refractive index of about 1.5 at THz frequencies, which results in an optical path length of only about 110 µm. Due to this small thickness of the window, also the modulation as a function of the angle is relatively weak, as displayed in Fig. 4.6(b). For the 2.5-THz QCL, the transmittance decreases monotonously with increasing angle, while for the 3.4-THz QCL the transmittance remains almost constant. Since the type-II intensity modulations are periodic, but the intensity transmitted through the window is monotonous in the relevant range of incidence angles, interferences due to reflections within the window cannot explain the type-II intensity modulations in the far-field distribution.

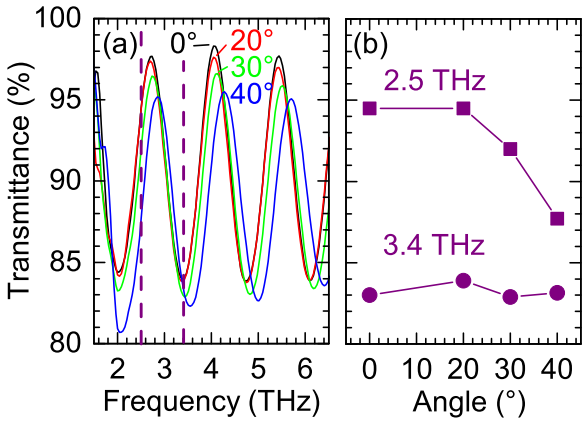

Figure 4.6: (a) Spectral transmittance for several angles of incidence of the 75-µm-thick polypropylene foil window employed for the measurements of the far-field distribution. An angle of 0° corresponds to normal incidence. (b) Transmittance as a function of the angle of incidence at the indicated frequencies of the THz radiation derived from (a).

Dependence of the far-field distribution on the QCL geometry

As described in the introduction of this chapter, intensity modulations in the far-field distributions have not only been reported for QCLs with single-plasmon, but also for QCLs with

metal-metal waveguides. In case of QCLs with metal-metal waveguides, the modulations were clearly attributed to the interference between radiation from the back and the front facet. Due to the confinement of the waveguide mode to sub-wavelength dimensions, the back facet radiates not only forward (away from the front facet) as usual for semiconductor stripe lasers, but also backward, i.e., toward the optical window. Interference between the radiation from the back facet and radiation from the front facet leads to intensity modulations in the far field of the QCLs with metal-metal waveguides. As this mechanism for QCLs with metal-metal waveguides is also a possible origin for the type-II modulations of QCLs with single-plasmon waveguides, it will now be investigated. Since for this mechanism the modulation period depends on the length of the QCL, the far-field distribution of QCLs with different lengths are investigated. Apart from this, also QCLs with different widths will be considered in order to obtain a full picture of the dependence of the far field on the geometry of the QCL.

Figures 4.7(a), 4.7(c), and 4.7(e) show the measurements of the far-field distribution for QCLs with a constant width of 150 µm and lengths of 1,009, 1,338, and 1,873 µm, respectively. Although the length is increased by almost a factor of 2 between 1,009 and 1,873 µm, the periodicity of the intensity modulations remains largely unchanged. Therefore, an effect originating from interference of radiation from the back facet with radiation from the front facet, which is known to be the dominant effect for the modulations observed for QCLs with metal-metal waveguides, can be excluded, because a strong dependence between the resonator length and the modulation period would be expected.

Figures 4.7(a), 4.7(b), and 4.7(d) show the far-field distributions of QCLs with single-plasmon waveguides with a constant length of 1,009 µm and different widths of 150, 120, and 200 µm, respectively. At angles β below $-10°$ (i.e., larger negative values), the modulation periodicity is very similar. There is some deviation in the modulations between $0°$ and $-10°$. The intensity maximum visible at values of β of about $-5°$ in Figs. 4.7(a) and 4.7(d) is not visible in Fig. 4.7(b). Despite this deviation, the far-field distributions can be considered to exhibit no significant difference. It can therefore be concluded that a relation between the intensity modulations and the width is also improbable. Therefore, the modulations are unlikely to originate from the QCL itself.

Interference of radiation reflected at the window of the cooling system

Since effects related to the geometry of the QCL or reflections within the optical window of the cooling system were excluded as the origin of the type-II modulations, a different mechanism has to be identified. Figure 4.8 illustrates that radiation reflected from the window of the cooling system can experience an additional reflection at the submount or cold finger, before it is transmitted through the window (cf. red arrow in Fig. 4.8). This radiation can be superimposed with the directly transmitted radiation (cf. blue arrow in Fig. 4.8), leading to intensity modulations. In particular, the intensity modulations are expected to change their periodicity with the distance a of the window from the QCL.

The left panels of Figs. 4.9(a), 4.9(b), and 4.9(c) show the measured far-field distributions with increasing distance a of the window from the QCL. The periodicities of the modula-

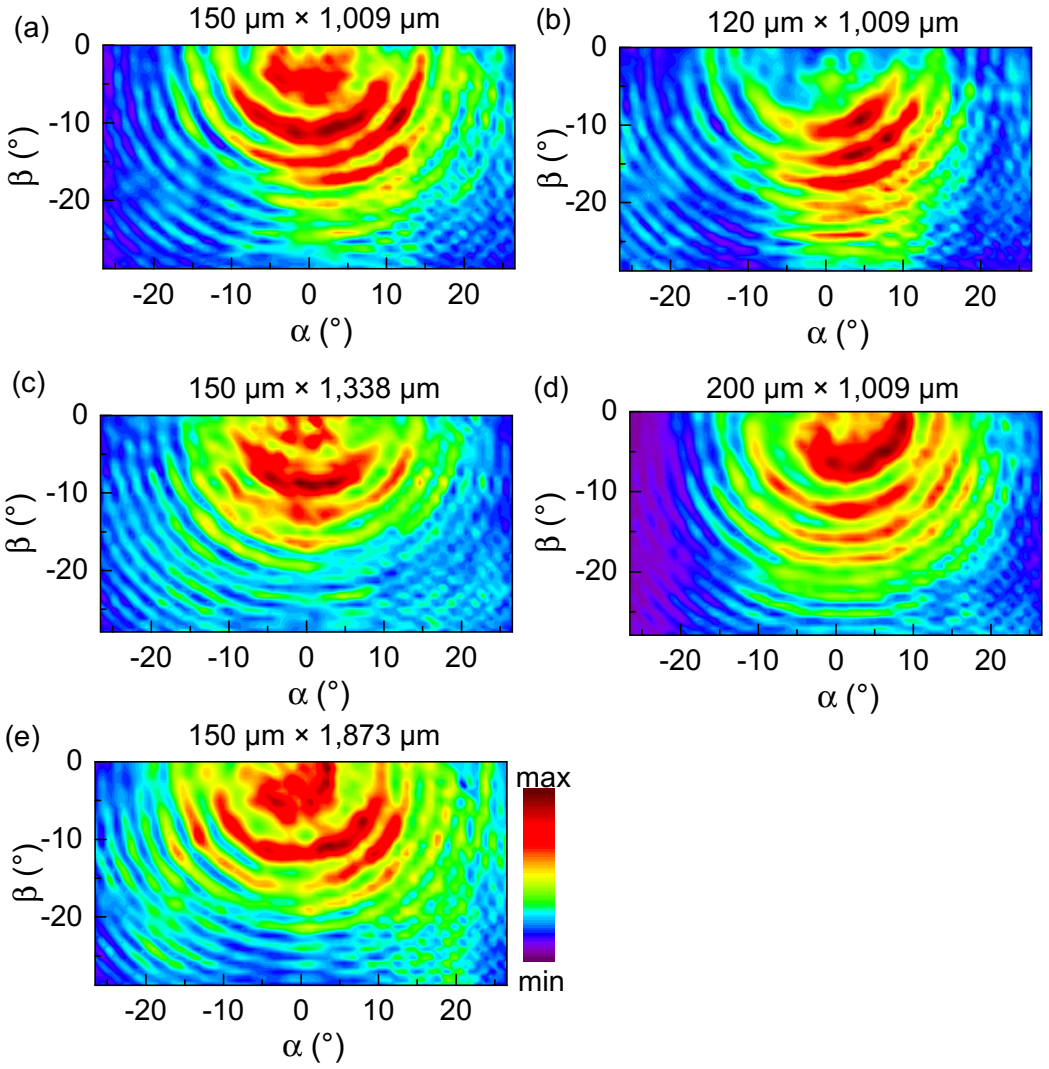

Figure 4.7: Measured far-field distributions for THz QCLs with the indicated dimensions (width × length), fabricated from wafer M4.2135. (a), (c), and (e) display the results of a series of different ridge lengths, keeping the ridge width constant at 150 µm, while (a), (b), and (d) show the far-field distributions of a series of different ridge widths, keeping the ridge length constant at 1,009 µm.

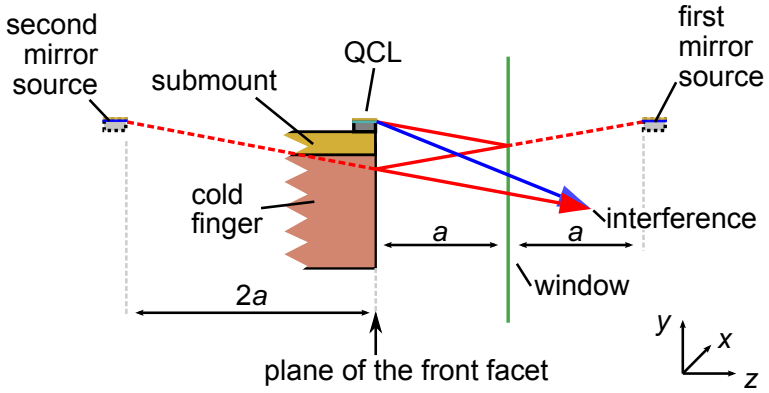

Figure 4.8: Schematic of the proposed mechanism for the type-II modulations, viewed from the side. The mechanism based on interference is displayed in the framework of both the geometrical-optics-based and the mirror source-based model. The optical window of the cooling system is located at a distance a from the plane of the front facet. First mirror source: mirror source corresponding to the reflection at the window of the cooling system. Second mirror source: mirror source corresponding to the second reflection at the submount/cold finger front side. The modulations in the far-field distribution arise from the interference of the directly transmitted radiation (blue arrow) and the radiation which is first reflected at the window and subsequently at the submount/cold finger (red arrow).

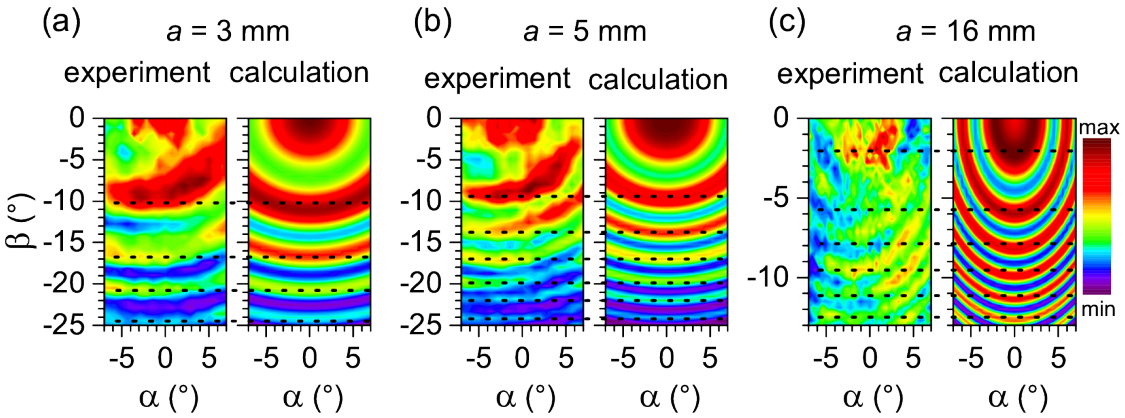

Figure 4.9: Comparison of the measured far-field distributions with the respective calculated results for the 2.5-THz QCL with a length of 1,873 µm for distances a of (a) 3, (b) 5, and (c) 16 mm. The error for the measurement of a is 1 mm. The detector distances d used in the measurements (a), (b), and (c) are 148, 150, and 300 mm, respectively. The values for a assumed in the calculation results (a), (b), and (c) are 2.69, 4.32, and 15.25 mm, respectively.

tions are clearly reduced for increasing a, strongly suggesting that the mechanism described above is indeed responsible for the type-II modulations in the far-field distribution.

For the calculation of the interference patterns relying on this mechanism, the mirror source-based model is used to account for the reflections. For a distance between the plane of the front facet and the window of a, the first reflection can be represented by a first mirror source (cf. Fig. 4.8) located at a distance a behind the window or, in other words, at a distance of $2a$ with respect to the plane of the front facet. The radiation from this mirror source is then again reflected at the submount or cold finger, which are both aligned with the QCL front facet. A second mirror source can account for this reflection (cf. Fig. 4.8), which is located at a distance of $2a$ behind the front facet of the QCL, since the first mirror source is located at the distance $2a$ in front of the submount/cold finger (plane of the front facet). By a coherent superposition of the radiation field of the QCL and the second mirror source, interference patterns build up behind the window. The first mirror source only plays a role in deriving the position of the second mirror source and has no part in the actual calculation of the interference patterns outside the cooling system.

The intensities of the radiation fields emitted by the QCL and the mirror source depend on the reflectivity of the window. From the measurement of the window transmittance in Fig. 4.6, the window reflectance (intensity ratio of the reflected wave) at 2.5 THz is estimated to amount to $R = 0.04$ and is assumed constant in the relevant range of incidence angles between 0° to 25°. The reflectance at the submount and cold finger is assumed to be 1, since they are both made from metal.

The intensity of the interference pattern arising at the detector plane due to the coherent superposition of radiation from the second mirror source (cf. Fig. 4.8) and the direct radiation from the QCL is given by

$$I_{\theta,R}(x,y,d) = |\sqrt{1-R}\,E_\theta(x,y,d) + \sqrt{R(1-R)}\,E_\theta(x,y,d+2a)|^2 \,, \tag{4.11}$$

where $x = d\tan(\alpha)$ and $y = d\tan(\beta)$. The first term on the right-hand side of the equation represents the field of the radiation that is directly transmitted through the window and the second term the field of the mirror source. Any secondary reflections are neglected because of the relatively low window reflectivity R.

In Fig. 4.9, the results of the calculations are compared to the measured far-field distributions for three different values of the distance a between the window and the plane of the front facet. The positions and intensities of the modulations in the measured and corresponding calculated far-field distributions agree very well. This agreement clearly shows that the described mechanism is responsible for the type-II intensity modulations.

4.5.2 Analysis of the mechanism

The model describing the underlying mechanism of the type-II intensity modulations can be used to predict and investigate the behavior of the modulations for parameters that have not been investigated experimentally. In that way, further insight into the physics of the underlying mechanism can be gained.

One of these additional physical insights is that the far-field distribution is extremely sensitive to small variations in a and λ. As an example, Fig. 4.10(a) shows a calculated profile of the far-field distribution for $\lambda = 120$ µm ($\nu = 2.5$ THz) and $a = 3$ mm. As shown in Fig. 4.10(b), a different profile with a phase shift of about π with respect to Fig. 4.10(a) is obtained when a is increased by only 0.03 mm. The origin of this shift is related to constructive and destructive interference in the direction along the z-axis (α and $\beta = 0°$). The intensity along the z-axis depends on the ratio

$$N = \frac{2a}{\lambda}\,, \tag{4.12}$$

where $N = 1, 2, \ldots$ for an intensity maximum and $N = 1/2, 3/2, \ldots$ for an intensity minimum. These conditions can be derived from Eq. (4.11). The profile of the far-field distribution shown in Fig. 4.10(a) exhibits a maximum at $\beta = 0°$, since $N = 50$ for $a = 3$ mm and $\lambda = 120$ µm according to Eq. (4.12) and is thus an integer. In contrast, a minimum is observed at $\beta = 0°$ for the profile displayed by the solid line in Fig. 4.10(b), because the value of a has been changed to 3.03 mm so that $N = 50.5$, which is an odd multiple of $1/2$. The profile of the far-field distribution changes in the same manner, if for $a = 3$ mm the wavelength λ is changed from 120 µm as used for the solid line in Fig. 4.10(a) to 118.81 µm as used for the dashed line in Fig. 4.10(b), keeping N constant. Since the value for λ or a is only slightly changed, the profiles appear to be identical. However, profiles for larger differences in λ or a keeping N constant may differ significantly at larger negative values of β.

The high sensitivity of the far-field distribution on the wavelength has an important consequence for QCLs in multi-mode operation. While every mode creates a far-field distribution with multiple lobes independently of the other modes, the detector records the incoherent superposition of these distributions. Figure 4.10(c) shows the profile of the resulting far-field distribution for $a = 3$ mm assuming two modes with different wavelengths of 120 and 118.81 µm, which represents the sum of the profile in Fig. 4.10(a) and the one indicated by the dashed line in Fig. 4.10(b). Because of the phase difference of about π between these two profiles, the oscillatory structure of Figs. 4.10(a) and 4.10(b) almost completely disappears in Fig. 4.10(c) so that the resulting far-field distribution is expected to be single lobed.

Apart from the coherence of the emitted radiation, the large divergence is the underlying fundamental property enabling the type-II modulations. While the results of the calculations shown in Figs. 4.10(a)–4.10(c) were achieved assuming a divergence angle of $\theta = 34°$, Fig. 4.10(d) shows the profile of the calculated far-field distributions for two smaller divergence angles of 5° and 15°. The other parameters are the same as for Fig. 4.10(a). The modulation of the profile is strongly reduced with decreasing divergence angle and completely disappears for $\theta = 5°$. The physical reason for this dependence is that for a radiation field with a small divergence angle the first minimum of the profile occurs at an angle, where the intensity of the radiation field has already vanished.

The described mechanism does not only apply to THz QCLs with single-plasmon, but also to QCLs with metal-metal waveguides, for which the cases of cleaved and etched facets

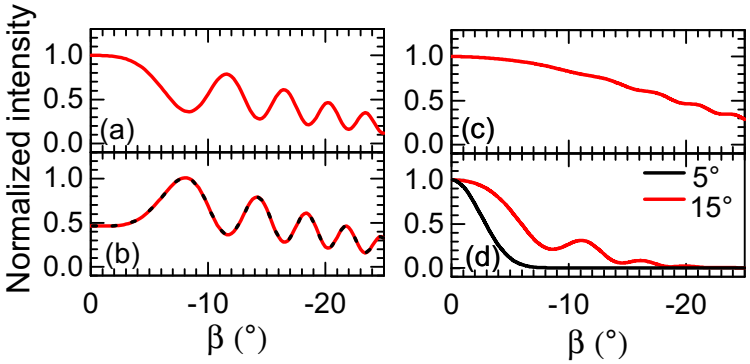

Figure 4.10: Profiles of the calculated far-field distributions for $\alpha = 0°$ at a distance $d = 150$ mm. (a) Profile for $a = 3$ mm, $\lambda = 120$ µm, and a divergence angle $\theta = 34°$. (b) Profile for $a = 3.03$ mm and $\lambda = 120$ µm (solid line) as well as $a = 3$ mm and $\lambda = 118.81$ µm (dashed line) both for $\theta = 34°$. The normalization of the intensity in (a) and (b) is identical. (c) Sum of the profiles for $a = 3$ mm with $\lambda = 120$ µm from (a) and $\lambda = 118.81$ µm from (b). (d) Profiles for $\theta = 5°$ and $15°$ for $a = 3$ mm and $\lambda = 120$ µm.

must be distinguished. This distinction is not applicable to THz QCLs with single-plasmon waveguides, which always have cleaved facets. In the case of cleaved facets, the modulations resulting from the reflections at the window are expected to appear in the lower half space (negative β), while the modulations resulting from interference between radiation from the front and the back facet develop predominantly in the upper half space. In the case of etched facets, the radiation is emitted predominantly into the upper half space (positive β), and the window usually reflects only a minor portion toward the submount/cold finger of the cooling system. Therefore, THz QCLs with metal-metal waveguides and cleaved facets are expected to exhibit similar phenomena as presented here for THz QCLs with single-plasmon waveguides.

4.5.3 Suppression of the modulations

In this section, it is shown how the modulations in the far-field distribution can be suppressed. As discussed in section 4.4, the type-I modulations can be relatively easily suppressed by mounting the QCL chip on the submount edge. Using such a 2.5-THz QCL mounted accordingly, this section focuses on the more difficult task of suppressing the type-II modulations, which is accomplished by using a ring-shaped absorptive material (Eccosorb) with a clear aperture of about 4 mm (diameter). In order to minimize the reflectivity of the absorber material, its absorption coefficient should be rather small and its thickness sufficiently large to avoid any transmission. The selected thickness is 3 mm. However, the large thickness of the absorber makes it difficult to position it in such a way that the direct emission from the QCL is not blocked by the absorber, and the radiation reflected at

the out-coupling window of the cooling system is absorbed. Figure 4.11(a) shows the setup with the absorber. As indicated by the purple arrow in Fig. 4.11(a), only radiation emitted from the QCL at a certain range of angles is not blocked by the absorber directly, but only the fraction reflected by the window is removed as intended. For larger negative angles than the angle indicated by the purple arrow, the radiation emitted by the QCL is attenuated or fully absorbed by the absorptive material. In contrast, for angles that are sufficiently close to 0° such as the angle indicated by the blue arrow in Fig. 4.11(a), radiation reflected at the window is not absorbed and can still lead to interference with the directly emitted radiation (red arrow). Thus, the modulations in the far-field distribution are not fully suppressed as can be seen from the measured far-field distribution in Fig. 4.11(b). To solve the problem of radiation still impinging on the submount, it is mounted at an angle of 20° with respect to the original setup as illustrated in Fig. 4.11(c). As a consequence, any residual radiation impinging on the submount is now deflected toward large positive angles and can no longer interfere with the directly emitted radiation, as illustrated by the blue arrow in Fig. 4.11(c).

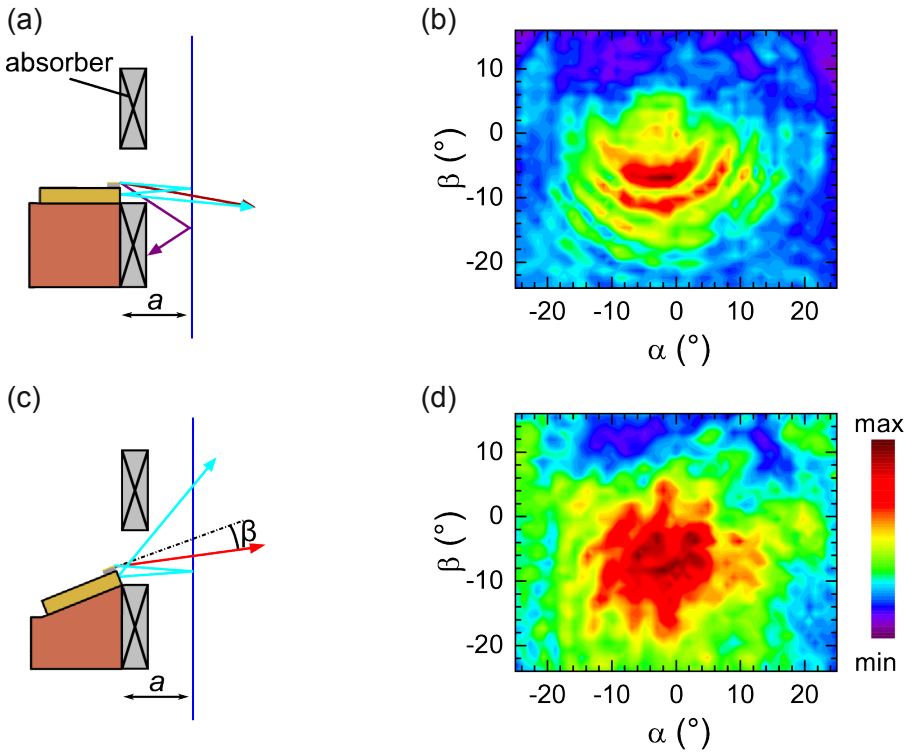

Figure 4.11: (a) and (c) Different setups using absorptive material. (b) and (d) Measured far-field distributions corresponding to the setups (a) and (c), respectively.

Therefore, the measured far-field distribution shown in Fig. 4.11(d) does not exhibit any type-II modulations.

4.6 Conclusions

In this chapter, the modulations in the far-field distribution of THz QCLs with single-plasmon waveguides have been investigated. Two types of modulations have been observed, which were referred to as type-I and type-II modulations. The type-I modulations can clearly be attributed to the presence of the exposed metal surface in front of the QCL front facet, if the QCL is mounted with a finite distance to the submount edge. The results of the calculation of the far-field distribution assuming specular reflections on the metal surface and subsequent interference with the directly emitted radiation are in good agreement with the experimental results. The type-II modulations can clearly be attributed to the interference of the directly emitted QCL radiation with radiation reflected at the cryostat window and the QCL submount/cold finger of the cooling system, since the modulations are very well reproduced by corresponding calculations. Finally, it is shown that both types of modulations can be suppressed by mounting the QCL chip on the edge of the submount and introducing an absorptive material together with an oblique mounting of the QCL.

5 Terahertz quantum-cascade lasers for operation at predefined emission frequencies

5.1 Introduction

Many proof-of-concept experiments have been performed showing that THz QCLs in continuous-wave operation are powerful sources for the spectroscopy of absorption (and emission) lines, exploiting their narrow spectral linewidths and their high output powers in the mW range [78, 92–98]. Since there is significant scientific interest for example in the study of sharp transitions between rotational energy levels of molecules, the application of THz QCLs for the high-resolution spectroscopy of these transitions is desirable. For that purpose, THz QCLs emitting at frequencies predefined by the samples to be investigated are required. While the active region of a QCL mainly determines the frequency range in which emission is possible, the exact position of the spectral modes depends mainly on the waveguide and resonator properties.

Applications in spectroscopy beyond proof-of-concept demonstrations are hindered by the limited inherent tuning capability of THz QCLs. Many techniques have been developed to enhance the tuning range of THz QCLs, but the larger tuning range comes at the cost of reduced power, unreliable frequency calibration, and frequency stability issues. In contrast, THz QCLs with only inherent tuning capabilities do not have these disadvantages, but a reliable fabrication for the emission at a specific frequency has turned out to be very challenging.

This chapter will focus on THz QCLs with Fabry-Pérot resonators and single-plasmon waveguides. Fabry-Pérot resonators usually exhibit multi-mode operation, which is required for a number of spectroscopic techniques such as multi-channel or dual-comb spectroscopy [94, 99–101]. This chapter mainly aims at a quantitative understanding and control of the Fabry-Pérot modes. This understanding is also important for single-frequency devices, since methods to suppress multi-mode operation such as distributed-feedback gratings or longitudinal multi-section approaches can be understood as mode selection techniques of effective Fabry-Pérot resonators.

This chapter begins with a description of the employed simulation techniques in section 5.2, which are then used to analyze the emission frequencies of THz QCLs with Fabry-Pérot resonators in section 5.3. The investigated waveguide widths range between 120 and 200 µm and the resonator lengths between 1,000 and 4,000 µm. Moreover, an emission bandwidth of about 100 GHz is assumed. These numbers cover most of the typical values in the experimental investigations. Based on the simulation results, a method for the precise

control of the emission frequencies is investigated in section 5.4. The achieved results are summarized in section 5.5.

5.2 Simulation of mode frequencies in Fabry-Pérot resonators

5.2.1 Fabry-Pérot modes in waveguide lasers

THz QCLs—just like most conventional semiconductor lasers—can be considered as waveguide lasers, in which waveguiding structures are employed to confine electromagnetic radiation to the active region in the lateral (x,y) direction [102]. Waveguide modes building up due to the optical gain in the active region travel along the waveguide in the z-direction. If the waveguide is of finite length, the waveguide mode is usually partly reflected at both ends—here referred to as facets—so that a Fabry-Pérot resonator is formed. The gain and phase requirements for the Fabry-Pérot modes in a waveguide laser are derived in this subsection.

The field of a waveguide mode propagating in the z-direction can be expressed as

$$\mathbf{E}_{x,y}(z) = \mathbf{E}_0(x,y)\exp\left([\Gamma g_{\mathrm{th}} - \tilde{\alpha}_{\mathrm{wg}}]z\right)\exp\left(-i\tilde{\beta}z\right), \tag{5.1}$$

where $\mathbf{E}_0(x,y)$ is the lateral field distribution of the waveguide mode, Γ the confinement factor, g_{th} the threshold gain, $\tilde{\alpha}_{\mathrm{wg}}$ the waveguide losses, and $\tilde{\beta}$ the propagation coefficient. The values of Γ, g_{th}, and $\tilde{\alpha}_{\mathrm{wg}}$ are assumed to be constant. The relation to the (angular) frequency ω is established by the dispersion relation $\omega(\tilde{\beta})$ of the waveguide mode. Alternatively, the dispersion can be expressed in terms of the frequency-dependent effective refractive index $n(\omega)$. Both representations are connected by the definition of the phase velocity v_{ph} and the corresponding refractive index n, reading without explicit functional dependencies

$$\frac{\omega}{\tilde{\beta}} = v_{\mathrm{ph}} = \frac{c}{n}, \tag{5.2}$$

where c represents the speed of light in vacuum. The function $\omega(\tilde{\beta})$ can be obtained from $n(\omega)$ by first rearranging Eq. (5.2) and taking the inverse function of $\tilde{\beta}(\omega)$, i.e.

$$\tilde{\beta}(\omega) = \frac{\omega n(\omega)}{c} \;\Rightarrow\; \omega(\tilde{\beta}) = \tilde{\beta}^{-1}(\omega). \tag{5.3}$$

Conversely, $n(\omega)$ can be obtained from the inverse function of $\omega(\tilde{\beta})$ and by employing Eq. (5.2) so that

$$n(\omega) = \frac{c\tilde{\beta}(\omega)}{\omega}. \tag{5.4}$$

For the consideration of the Fabry-Pérot modes, let the facets of the resonator be located at $z = 0$ and $z = L$ and the corresponding real-valued reflectivities be defined as R_1 and R_2. For simplicity, it is assumed that the waveguide mode experiences the same phase shift (either 0 or π) at the waveguide ends so that the total phase shift is either 0 or 2π and can therefore be neglected.

A laser mode of a resonator is characterized by a periodicity with respect to one round trip, which means that the field strength of the mode that has traveled a path $2L$ and has experienced reflections at both ends of the waveguide is required to be equal to the field strength of the mode that did not travel at all. This condition can be expressed as

$$\mathbf{E}(x,y,0) = \mathbf{E}(x,y,2L) \Leftrightarrow \tag{5.5}$$

$$\mathbf{E}_0(x,y) = \mathbf{E}_0(x,y)\sqrt{R_1R_2}\exp\left([\Gamma g_{\mathrm{th}} - \tilde{\alpha}_{\mathrm{wg}}]2L\right)\exp\left(-i\tilde{\beta}2L\right). \tag{5.6}$$

If $\mathbf{E}_0(x,y)$ is non-vanishing, it can be removed from Eq. (5.6), which is then fulfilled if both the amplitude (the real factors) and the phase factor (the complex exponential) are equal to 1, yielding two equations. The first equation

$$\sqrt{R_1R_2}\exp\left([\Gamma g_{\mathrm{th}} - \tilde{\alpha}_{\mathrm{wg}}]2L\right) = 1 \tag{5.7}$$

determines the threshold gain g_{th} for the laser oscillation, i.e.

$$\Gamma g_{\mathrm{th}} = \frac{1}{2L}\ln\left(\frac{1}{\sqrt{R_1R_2}}\right) + \tilde{\alpha}_{\mathrm{wg}}\,. \tag{5.8}$$

The second equation

$$\exp\left(-i2\tilde{\beta}L\right) = 1 \tag{5.9}$$

leads to

$$2\tilde{\beta}L = 2M\pi \;\Rightarrow\; \tilde{\beta}_M = \frac{M\pi}{L} \tag{5.10}$$

using a positive integer M. The value of M represents the order of the Fabry-Pérot mode. From this condition, frequencies of the Fabry-Pérot modes can be determined by employing the dispersion relation of the waveguide $\omega(\tilde{\beta})$ as will be explained in detail in subsection 5.2.3.

5.2.2 Simulation of the waveguide dispersion

Approach

The waveguide dispersion $\omega(\tilde{\beta})$ of the single-plasmon waveguide used for THz QCLs can be obtained by the the rigorous solution of Maxwell's equations for the waveguide geometry. Here, the commercial software package *JCMsuite* is used, which applies the finite-element method. In order to obtain the waveguide dispersion, the problem class *propagating modes* is employed. Based on a given waveguide geometry, material parameters, and a desired frequency of the solution, the field distributions, the effective refractive index n (often denoted $\tilde{n}$ in the literature), and the losses of a waveguide mode are calculated. Only the fundamental transverse magnetic mode is taken into account, since no transverse electric or higher-order modes build up in QCLs with single-plasmon waveguides, if they are not too wide. The dispersion can be obtained by consecutive simulations for different frequencies, yielding a frequency-dependent refractive index $n(\omega)$, from which $\omega(\tilde{\beta})$ can be determined by Eq. (5.3).

Material parameters used for the simulations

For the material parameters, frequency-dependent functions for the permittivities implemented by Wienold are employed [103, 104], which take into account the material dispersion. The parameters for the $Al_xGa_{1-x}As$ material system as a function of aluminum content x and doping density are based on experimental data by Palik [105, 106] and by Levinshtein *et al.* [107] as well as on additional measurements. In order to limit the complexity of the simulations, a constant temperature is assumed. The selected temperature is 100 K, since the refractive index changes only slightly below that temperature. The active region is considered as a single effective layer with a thickness of 11 µm and an average aluminum content of $x = 0.02$. The highly doped layers for the top and bottom contact have doping densities of 5×10^{18} and 2×10^{18} cm^{-3} as well as thicknesses of 0.08 and 0.7 µm, respectively. For the material parameter of the top metal (gold), a Drude-Lorentz approximation as used in Ref. [71] for simulations of THz QCLs is employed with a relaxation time of 0.06 ps and a carrier density of 5.9×10^{22} cm^{-3}. The above approach for the material parameters does not involve gain or losses due to intersubband transitions in the active region. Since the real and imaginary parts of the complex refractive index are coupled by the Kramers-Kronig relation, taking into account gain and losses due to intersubband transitions would also imply a change in the real part of the complex refractive index. This relation is quite intricate and is expected to depend on the particular design of the active region. In addition, the value of the gain also depends on the mirror losses, which, in turn, depend on the length of the resonator. Therefore, to limit the complexity, gain and losses due to intersubband transitions are neglected.

Figure 5.1(a) displays the simulation results of the effective refractive index n as a function of the frequency for the waveguide widths $W = 120$ and 200 µm. The value of n is somewhat higher for a waveguide width of 200 µm than for a width of 120 µm due to the different waveguide dispersion. This difference decreases toward higher frequencies, since the waveguide mode is more localized in the center of the waveguide so that the waveguide

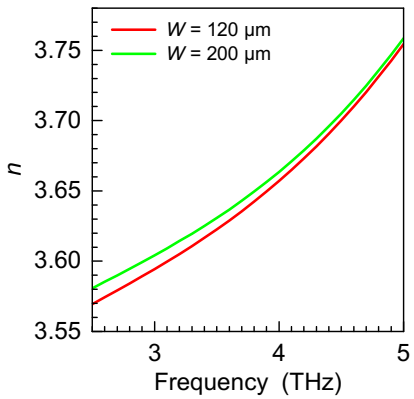

Figure 5.1: Effective refractive index n as a function of frequency for the two waveguide widths $W = 120$ and 200 µm.

width becomes less important. The displayed dispersion relation is the basis for the calculation of the frequencies of the Fabry-Pérot modes as will be described in the following subsection.

5.2.3 Calculation of Fabry-Pérot mode frequencies

In this subsection, several methods for the calculation of the frequencies of the Fabry-Pérot modes based on the waveguide dispersion are presented. First, the rigorous method is described, for which no additional approximations are used. In addition, several approximate methods are presented, for which the results will be compared to the results of the rigorous method in section 5.3. The approximate method "S" is similar to the usually assumed approximations for conventional semiconductor lasers for the Fabry-Pérot mode positions and spacing. The approximate method "N" assumes a linear dependence of the refractive index on the frequency. The results of this approximate method are compared with the results of the rigorous method in order to investigate the impact of the curvature of the refractive index. Similarly, the comparison of the results of the approximate method "N", for which a linear dependence of the refractive index is assumed, with the results of method "N0", which assumes a constant refractive index, allows to study the influence of the slope of the refractive index on the Fabry-Pérot modes.

Rigorous method

Based on the dispersion relation $\omega(\tilde{\beta})$, the frequencies of the Fabry-Pérot mode of order M can readily be obtained by substituting $\tilde{\beta}_M$ from Eq. (5.10) into the dispersion relation Eq. (5.3), i.e.

$$\omega_M = \omega(\tilde{\beta}_M) = \omega(\tilde{\beta})|_{\tilde{\beta}=M\pi/L} \,. \tag{5.11}$$

Here, an equivalent, but more direct approach to obtain the mode frequencies is used, which is based on a numerical solution of

$$\frac{M\pi}{L} = \frac{\omega_M n(\omega_M)}{c} \tag{5.12}$$

for the angular frequency ω_M.

Approximate methods "S"

The approximate method "S" is based on a linear approximation of $\omega_M(\beta)$. The Taylor expansion to the first order of the dispersion relation $\omega(\tilde{\beta})$ around the reference point $\tilde{\beta}_\mathrm{r}$ is given by

$$\omega(\tilde{\beta}_\mathrm{r} + d\tilde{\beta}) = \omega(\tilde{\beta}_\mathrm{r}) + d\tilde{\beta}\left.\frac{d\omega}{d\tilde{\beta}}\right|_{\tilde{\beta}=\tilde{\beta}_\mathrm{r}} \tag{5.13}$$

$$= \omega(\tilde{\beta}_\mathrm{r}) + d\tilde{\beta}\, v_\mathrm{gr}(\tilde{\beta}_\mathrm{r}) \,, \tag{5.14}$$

where the definition of the group velocity v_{gr} was used. For the consideration of Fabry-Pérot modes, $\tilde{\beta}_M$ from Eq. (5.10) can be rewritten using $M = M_0 + \Delta M$, where the values of ΔM are small positive or negative integers:

$$\tilde{\beta}_{M_0+\Delta M} = \frac{\pi}{L} M_0 + \frac{\pi}{L} \Delta M = \tilde{\beta}_{M_0} + \Delta\tilde{\beta}_{\Delta M} \,. \tag{5.15}$$

In the limiting case $M_0 \to \infty$ and $\Delta M \to 0$, $\tilde{\beta}_{\mathrm{r}}$ can be identified with $\tilde{\beta}_{M_0}$ and $d\tilde{\beta}$ with $\Delta\tilde{\beta}_{\Delta M}$. The Fabry-Pérot modes are then given by

$$\omega_{M_0+\Delta M} = \omega(\tilde{\beta}_{M_0}) + \frac{\pi}{L} \Delta M \, v_{\mathrm{gr}}(\tilde{\beta}_{M_0}) \,. \tag{5.16}$$

From this equation, it is already clear that for a certain fixed reference point $\tilde{\beta}_{M_0}$ adjacent Fabry-Pérot modes are equally spectrally spaced.

The last equation can also be expressed in terms of n and the group refractive index n_{g} using $\omega/\tilde{\beta} = c/n$ and $v_{\mathrm{gr}} = c/n_{\mathrm{g}}$ so that the mode frequencies read

$$\omega_{M_0+\Delta M} = \underbrace{\frac{c\pi}{L} \frac{M_0}{n(\omega_{M_0})}}_{\omega_{M_0}} + \Delta M \underbrace{\frac{c\pi}{L} \frac{1}{n_{\mathrm{g}}(\omega_{M_0})}}_{\Delta\omega} \,, \tag{5.17}$$

where n_{g} is given by

$$n_{\mathrm{g}}(\omega_{M_0}) = n(\omega_{M_0}) + \omega_{M_0} \left.\frac{dn}{d\omega}\right|_{\omega=\omega_{M_0}} \,. \tag{5.18}$$

Equation (5.17) directly yields the expression for the mode spacing of Fabry-Pérot resonators usually given in the literature, which reads

$$\Delta\omega = \omega_{M_0+1} - \omega_{M_0} = \frac{c\pi}{L n_{\mathrm{g}}(\omega_{M_0})} \,. \tag{5.19}$$

Approximate method “N”

Equation (5.12) leads to

$$\omega_M = \frac{M\pi c}{L n(\omega_M)} \,, \tag{5.20}$$

which is an implicit equation in ω_M. For the refractive index n, the linear ansatz

$$n(\omega_M) = n_0 + (\omega_M - \omega_0) n' \tag{5.21}$$

is used, where $n_0 = n(\omega_0)$ and

$$n' = n'(\omega_0) = \left.\frac{dn}{d\omega_M}\right|_{\omega_M=\omega_0} \,. \tag{5.22}$$

With this ansatz, Eq. (5.20) is transformed into the quadratic equation

$$\omega_M^2 + \omega_M \left(\frac{n_0}{n'} - \omega_0 \right) - \frac{M\pi c}{Ln'} = 0 \,, \tag{5.23}$$

of which the physical solution is

$$\omega_M = -\frac{1}{2} \left(\frac{n_0}{n'} - \omega_0 \right) + \sqrt{\frac{1}{4} \left(\frac{n_0}{n'} - \omega_0 \right)^2 + \frac{M\pi c}{Ln'}} \,. \tag{5.24}$$

The value of M, which is necessary to calculate the Fabry-Pérot mode frequencies by means of Eq. (5.24), is determined by replacing ω_M by ω_0 in Eq. (5.20) and taking the closest integer value. Equation (5.24) is used to calculate the frequency shift of a Fabry-Pérot mode upon a small length variation.

Approximate method "N0"

If the refractive index n is approximated to the zeroth order at a reference frequency ω_0, i.e.

$$n(\omega) = n(\omega_0) = n_0 \,, \tag{5.25}$$

the mode spacing can be obtained directly from Eq. (5.20) and therefore reads

$$\Delta\omega = \omega_{M+1} - \omega_M = \frac{\pi c}{Ln_0} \,. \tag{5.26}$$

The frequency shift for a small variation dL of the resonator length L_0 can be obtained by the differential of Eq. (5.20).

$$d\omega = -\frac{M\pi c}{L_0^2 n_0} dL \,. \tag{5.27}$$

In the limiting case $M \to \infty$, M can be considered continuous and be obtained from Eq. (5.20) under the assumption made in Eq. (5.25). M then reads

$$M = \frac{L_0 n_0 \omega_0}{\pi c} \,. \tag{5.28}$$

Consequently, Eq. (5.27) is reduced to

$$d\omega = -\frac{\omega_0}{L_0} dL \,. \tag{5.29}$$

Note that this equation is independent of the refractive index.

5.3 Analysis of Fabry-Pérot modes in terahertz quantum-cascade lasers

5.3.1 Simulation results

Based on the simulated waveguide dispersion for THz QCLs, the dependencies of the Fabry-Pérot mode frequencies on waveguide and resonator dimensions are investigated. The rigorous method for the determination of the Fabry-Pérot modes is compared to the approximate methods. The calculated values are expressed in terms of the frequency $\nu = \omega/2\pi$ in order to be comparable to the experimental results.

Single-plasmon waveguides with Fabry-Pérot resonators typically have widths between $W = 120$ and 200 µm and lengths between 1,000 and 4,000 µm. The typical bandwidth of the emission is on the order of 100 GHz for driving current densities significantly above the threshold current density. These numbers are the basis for the simulations.

Figure 5.2(a) shows the frequencies of the Fabry-Pérot modes of orders $M = 100$ to 104 as a function of a small length variation from 1,500 to 1,520 µm calculated with the rigorous method. In case of the 120-µm-wide waveguide, all modes shift linearly toward lower frequencies for increasing lengths by about 36 GHz. On the frequency scale used in Fig. 5.2(a), the spacing between the modes of successive order is identical at constant resonator length. Similarly, no change in the spacing for increased resonator lengths from 1,500 to 1,520 µm is observed. Figure 5.2(a) also shows the Fabry-Pérot modes for a waveguide width of

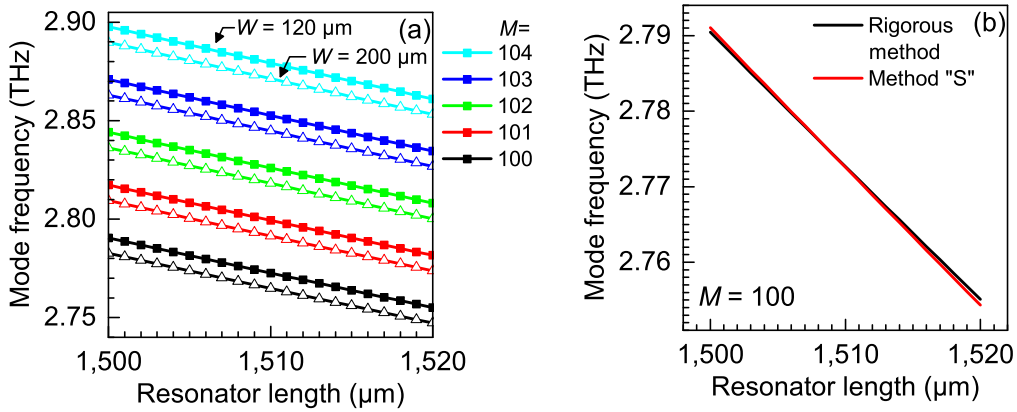

Figure 5.2: (a) Frequencies of the Fabry-Pérot modes of order $M = 100$ to 104 as a function of a small length variation from 1,500 to 1,520 µm for a waveguide width W of 120 (squares) and 200 µm (triangles). The corresponding mode order M is indicated in the legend. (b) Comparison of the calculation results based on the rigorous and approximate method "S" for the mode order $M = 100$ and waveguide width $W = 120$ µm. The chosen reference frequency is $\nu_0 = 2.83$ THz, and the reference mode order is $M_0 = 102$.

200 µm, which are collectively shifted toward lower frequencies by about 8 GHz with respect to the 120-µm-wide waveguide due to the different waveguide dispersion. A similar calculation as done for Fig. 5.2(a) based on the rigorous approach can also be performed by using the approximate method "S". The parameters for the linear approximation M_0 and ν_{M_0} are chosen in a such way that they are mean values in the considered range of mode orders and mode frequencies so that they amount to $M_0 = 102$ and $\nu_{M_0} = 2.83$ THz. On the frequency scale of Figure 5.2(a), the results of the calculation based on the rigorous and the approximate method "S" cannot be distinguished.

Figure 5.2(b) shows a comparison of the results based on the rigorous and the approximate method "S" for the mode of order $M = 100$ and a waveguide width of 120 µm. On the scale of Fig. 5.2(b), a difference mainly with respect to the slopes between both approaches can be clearly observed. The difference of the mode frequencies for both approaches is largest at a resonator length of 1,520 µm, at which the difference in the mode frequencies amounts to 0.7 GHz.

Figure 5.3(a) shows the spacing of the modes displayed in Fig. 5.2(a) as a function of the mode spacing index M^*. A mode spacing index M^* of for example 101 signifies the spacing between the modes of order 100 and 101. The rectangles and crosses represent the results

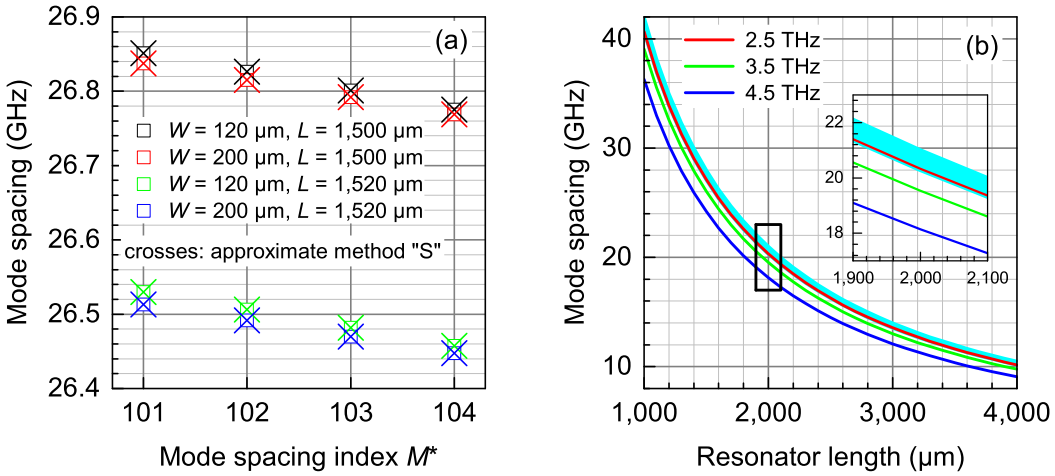

Figure 5.3: (a) Spacing between the modes of order $M^* - 1$ and M^* for the indicated waveguide widths W and resonator lengths L. The rectangles and crosses represent the results of the calculations based on the rigorous method and the approximate method "S", respectively. (b) Mode spacing as a function of resonator length at center frequencies of 2.5, 3.5, and 4.5 THz. The difference between waveguides with a width of 120 and 200 µm are too small to be observed in the graph. For clarity, the points for which the calculations were performed are not displayed. The cyan-colored shaded area represents the results of the calculation with the approximate method "N0" for frequencies between 2.5 and 4.5 THz. The inset shows an enlarged view of the region indicated by the rectangle in the main plot.

of the calculation based on the rigorous and the approximate method "S", respectively. The selected reference frequency for the approximate method is always the center frequency between adjacent modes. For instance, a center frequency of 2.885 THz is selected for adjacent Fabry-Pérot modes at 2.87 ($M = 103$) and 2.90 THz ($M = 104$) for the 1,500-µm-long resonator. Figure 5.3(a) clearly shows that the results of the approximate method "S" agrees very well with the ones of the rigorous calculation. Moreover, for increasing M^*, the mode spacing is reduced by somewhat less than 0.1 GHz for the investigated lengths and widths. Note that an increasing mode spacing index M^* corresponds to higher center frequencies. The mode spacings for different waveguide widths at the same resonator length are very similar, i.e. the difference amounts to less than 0.1 GHz. If the length is increased from 1,500 to 1,520 µm, the mode spacing is reduced by about 0.32 GHz for both widths.

The discussion of the change of the mode spacing across a bandwidth of 100 GHz in Fig. 5.3(a) was restricted to a center frequency of 2.82 THz and to resonator lengths of 1,500 to 1,520 µm. More generally, the change of the mode spacing over a bandwidth of 100 GHz is larger for shorter waveguides and higher center frequencies. For a length of 1,000 µm and a center frequency of 5.0 THz, the maximal change of the mode spacing amounts to about 0.4 GHz. For longer resonators and smaller frequencies, this number is substantially reduced.

Since the approximate method "S" yields accurate results, it is well suited to analyze the dependence of the mode spacing both as a function of length and of the center frequency. Figure 5.3(b) shows the mode spacing as a function of the resonator length for frequencies of 2.5, 3.5, and 4.5 THz. The difference between the waveguide widths W of 120 and 200 µm is very small and not observable in the graph. The mode spacing at a frequency of 4.5 THz is by 4 GHz smaller as compared to the mode spacing at 2.5 THz for a resonator length of 1,000 µm and by 1 GHz for a resonator length of 4,000 µm. For comparison, the results for the calculation with the approximate method "N0", which neglects the slope of the frequency-dependent refractive index, are also shown in Fig. 5.3(b). In the framework of this approximation, the mode spacing follows the same trend with increasing resonator length and center frequency. However, the variation with frequency is substantially reduced as compared to the method "S". Therefore, the results are shown as a shaded area in Figure 5.3(b) for clarity, representing the frequencies between 2.5 and 4.5 THz. While both approximations yield similar results at 2.5 THz, the deviation increases substantially toward higher frequencies. At a center frequency of 4.5 THz and a resonator length of 1,000 µm, the difference amounts to almost 6 GHz.

In order to determine the frequency shift due to a change of the resonator length as a function of the initial length, the red shift has been calculated for three different initial frequencies using a fixed length change of $\Delta L = +1$ µm. Figure 5.4(a) shows the red shift of a Fabry-Pérot mode as a function of the initial length calculated with the rigorous method. The same calculation has also been performed with the approximate method "N", the results of which agree very well with the results of the rigorous approach and are therefore not shown. Since method "N" is based on a linear approximation of the refractive index around a specific center frequency, it can be concluded that the curvature of $n(\nu)$ is not important for the present calculation. In contrast to method "N", method "N0" neglects the slope of

$n(\nu)$ and therefore assumes that the refractive index is constant. As a result, there is some deviation in the results obtained with method "N0" as compared to the results obtained with the rigorous method (and method "N") as shown in Fig. 5.4(a) for a frequency of 4.5 THz, for which the deviation is largest.

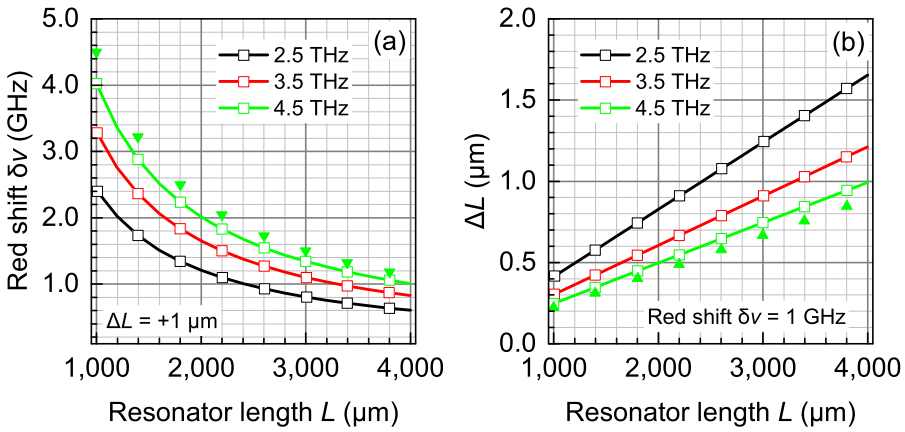

Figure 5.4: (a) Red shift of a mode at a frequency of 2.5, 3.5, or 4.5 THz as a function of initial resonator length for a length extension of $\Delta L = +1$ µm. The waveguide width is 120 µm. The results for a waveguide width of 200 µm are practically identical. The rectangular symbols represent the calculation results obtained by the rigorous method. The triangles represent the results of the approximate method "N0" for 4.5 THz. For frequencies of 3.5 and 2.5 THz, the deviation from the results of the rigorous method are much smaller and therefore not displayed for clarity. (b) Necessary increase of the resonator length ΔL to obtain a red shift of $\delta\nu = 1$ GHz for a Fabry-Pérot resonator. The same parameters as in (a) were used for the calculation.

The simulations show that the frequency shift is smaller for longer resonators or lower frequencies. For an initial resonator length of 1,000 µm, the frequency shift amounts to 2.4 and 4 GHz for initial mode frequencies of 2.5 THz and 4.5 THz, respectively. For an initial resonator length of 4,000 µm, the frequency shift amounts to 0.6 GHz at 2.5 THz and 1.0 GHz at 4.5 THz.

For a tuning of the laser frequency to a given value, the necessary correction of the resonator length for the respective frequency change has to be determined. Figure 5.4(b) shows the length change ΔL that is necessary to obtain a red shift of $\delta\nu = 1$ GHz as a function of the initial resonator length L. A linear dependence of ΔL as a function of the intial length L is observed. For $L = 1{,}000$ µm, ΔL amounts to 0.2 and 0.4 µm for 4.5 and 2.5 THz, respectively, which increases to 1.0 and 1.55 µm, respectively, for $L = 4{,}000$ µm. Figure 5.4(b) also displays the result of the calculation with the approximate method "N0" for a frequency of 4.5 THz (triangles).

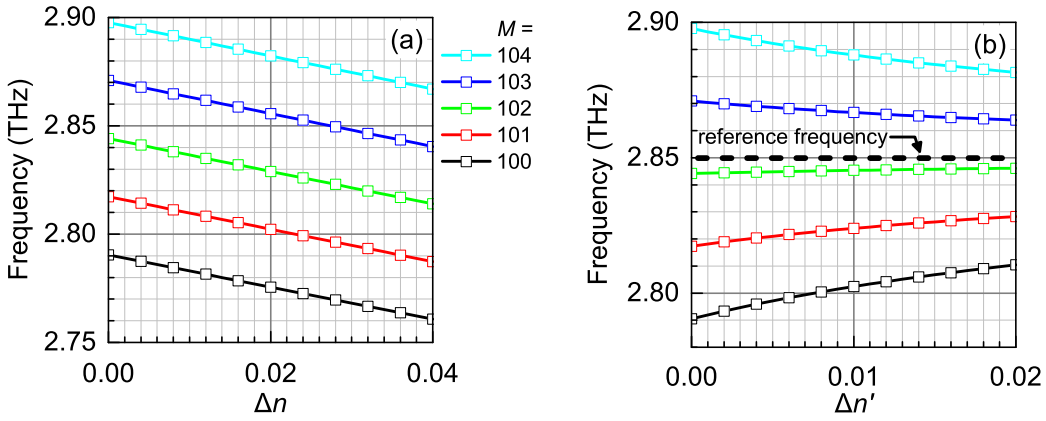

Figure 5.5: (a) Fabry-Pérot mode frequencies of order $M = 100$ to 104 for increasing refractive index. Based on the refractive index $n(\nu)$ for the 120-µm-wide waveguide, the refractive index $n(\nu)$ is increased by Δn. (b) Fabry-Pérot mode frequencies of order $M = 100$ to 104 for increasing slope n' of the refractive index. The refractive index for this calculation is assumed to be $n(\nu) + (\nu - \nu_0)\Delta n'$, where $\nu_0 = 2.85$ THz represents the reference frequency and $n(\nu)$ the dispersion for a waveguide width of $W = 120$ µm. The color coding of the lines for different values of M is the same as in (a).

Figure 5.5(a) shows how the Fabry-Pérot modes shift if the absolute value of the refractive index is increased. The calculation is based on the frequency-dependent refractive index for the 120 µm-wide waveguide, to which a value of Δn is added. Similar to the case of an increasing physical length of the resonator as shown in Fig. 5.2(a), the modes shift to lower frequencies for increasing refractive index. The spacing between the modes remains rather constant. The maximum change of the mode spacing amounts to 0.02 GHz between the modes at $\Delta n = 0$ and $\Delta n = 0.04$.

The frequencies of the Fabry-Pérot modes depend not only on the absolute value of the frequency-dependent refractive index, but also on its slope n'. Figure 5.5(b) shows this dependence based on the refractive index of a waveguide with a width of 120 µm, to which a linear function $(\nu - \nu_0)\Delta n'$ was added. The reference frequency $\nu_0 = 2.85$ THz has been chosen such that it is at about the center of the investigated frequency range. As a result, the frequency of the mode $M = 102$ remains practically constant, since it is close to the reference frequency. The modes of lower and higher orders approach the mode with $M = 102$ as $\Delta n'$ is increased. Therefore, the mode spacing is decreased from 26.8 to 17.8 GHz for an increase of $\Delta n'$ by 0.02. Note that the investigated range of $\Delta n'$ is quite large, which was chosen for clarity. In contrast to the selected change in $\Delta n'$ by 0.02 as shown in Fig. 5.5(b), the difference between the slopes of the 120- and 200-µm-wide waveguide amounts to only 0.0028 at 2.85 THz. Consequently, the mode spacing differs only very little between the waveguides with a width of 120 and 200 µm, as was already shown in Fig. 5.3(a).

5.3.2 Discussion

The Fabry-Pérot modes have been investigated with respect to the waveguide width and resonator length. Due to the different waveguide dispersion depending on the resonator width, the Fabry-Pérot modes are located at different frequencies for the same resonator length, while the mode spacing remains approximately constant. Similar to the mode spacing, a difference in the waveguide width has also a negligible effect on the frequency shift for a small length variation. In contrast, the resonator length and the emission frequency have a large effect on the mode spacing and on the frequency shift for a small length variation.

The typical approximation employed in the literature for conventional semiconductor lasers, which is referred to as approximate method "S", assumes that the spacing between two consecutive modes remains constant. This is also a good approximation for THz QCLs with typical waveguide widths and resonator lengths. From the results of the calculations with the rigorous method, it has been found that the deviation from a constant mode spacing is larger for shorter resonators and larger frequencies, which may be observed in a careful measurement and analysis of emission spectra with sufficient resolution, but will be difficult to observe for larger resonators and smaller frequencies.

A small variation in length of 1 µm causes a frequency shift of the Fabry-Pérot modes of roughly between 1 and 4 GHz depending on the considered resonator length and frequency. Therefore, if a control of the frequency with a precision of for example 1 GHz is desired, the length has to be controlled with a precision of better than 1 µm. The lengths of Fabry-Pérot resonators are defined by cleaving in accordance with the established fabrication method. Cleaving by hand has a precision of ± 50 µm at best, which is two orders of magnitude larger than what would be needed to control the emission frequency on the scale of GHz. Employing special cleaving devices may allow for a maximal precision of several µm, which is still not sufficient. Fabrication methods for the definition of the Fabry-Pérot resonators other than cleaving do not come into consideration, mainly because the mode in single-plasmon waveguides for THz QCLs partly penetrates also into the substrate so that a "mirror" of the Fabry-Pérot resonator must be formed by the heterostructure and the substrate together in a plane perpendicular to the ridge axis and to the growth direction.

The Fabry-Pérot modes are not only shifted for varying resonator lengths, but also if the refractive index is changed. An important consequence is that small differences between the measured and the simulated refractive index will lead to a disagreement in the measured and simulated individual mode positions. Uncertainties in the material parameters are one possible origin of these differences.

Furthermore, the above mentioned inherent tuning relies on changes of the refractive index due to modified operating conditions. The operating conditions include the employed bias (current/voltage) to drive the QCL, the cold finger temperature, and the operation mode, i.e. pulsed or continuous-wave. In case of continuous-wave operation, the QCL is heated by the dissipated thermal power, which is not the case for pulsed operation with a sufficiently low duty cycle. For the investigation of the inherent tuning mechanisms, pulsed operation is much better suited, since in this case current/voltage-induced tuning can be distinguished from temperature-induced tuning.

Figure 5.6 shows the red shift of a mode at about 3.39 THz, when the temperature is increased from 5 to 100 K. The mode frequency is shifted to lower frequencies by about 6.5 GHz. This shift cannot be explained by thermal expansion or compression of the QCL. The largest value of the expansion coefficient within the considered temperature range is attained at 100 K and amounts to about $2 \times 10^{-6}\,\mathrm{K}^{-1}$. By employing this value together with a temperature difference of 100 K, an upper limit of the thermal expansion can be calculated, which amounts to about 0.3 µm for a resonator length on the order of 3,000 µm. According to the results of the simulations, this value is by far too low to explain the observed frequency shift. Thus, the influence of thermal expansion on the temperature-induced tuning is negligible, and the temperature-induced change of the material refractive index is expected to be responsible for the frequency shift.

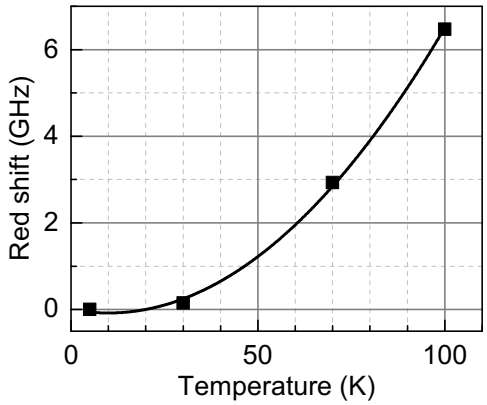

Figure 5.6: Red shift of the emission frequency of a mode at about 3.39 THz at 5 K with increasing temperature. The employed QCL was fabricated from the wafer M4.2650 with a width of 200 µm and a length of 3,423 µm. It was operated in pulsed mode with a duty cycle of 0.25%. The voltage was kept constant at 6.8 V. The line represents a guide to the eye.

Current/voltage-induced tuning, i.e. not induced by sample heating due to the dissipated heat, can usually be observed in pulsed operation at a constant temperature. This tuning can also be understood as originating from a change in the refractive index. Absorption/gain is linked to the refractive index via the Kramers-Kronig relation. Since absorption/gain in the active region depends on the applied bias, it may lead to a change in the refractive index and therefore to tuning. This effect is known as frequency pulling [108–111].

5.3.3 Summary

Based on the simulations of the waveguide dispersion, the modes of a Fabry-Pérot resonator have been quantitatively analyzed for resonator lengths between 1,000 and 4,000 µm and waveguide widths between 120 and 200 µm. The specific mode frequencies depend sensi-

tively on the resonator length and the refractive index, while the mode spacing depends less sensitively on these parameters. For a sufficiently small variation of the resonator length or refractive index, there is a collective linear shift of the modes with increasing resonator length or refractive index so that the mode spacing remains approximately constant. For a variation in resonator length of 1 µm, the Fabry-Pérot modes shift between 0.8 and 4.0 GHz depending on the resonator length and emission frequency.

The specific frequencies of the Fabry-Pérot modes depend on the effective refractive index of the waveguide mode, the waveguide width, and the resonator length. While the effective refractive index is difficult to manipulate since it is mainly determined by the material refractive indexes, the waveguide widths can be precisely controlled by photolithography. However, the influence of the waveguide width on the mode frequency is very limited. For instance, the frequency difference between a 120- and a 200-µm-wide waveguide for a 1,500-µm-long resonator amounts to only 20% of the mode spacing at 2.8 THz. The relationship between the frequencies and the length is very sensitive, which is a blessing and a curse at the same time. On the one hand, the sensitivity of the relationship prevents a control of the frequencies by the definition of the Fabry-Pérot resonator through cleaving, which is too inaccurate. On the other hand, it may allow for a manipulation of the mode frequencies without significantly changing the ridge area (or volume) and consequently the heat dissipation, which would enable an independent optimization of emission frequencies and thermal management. Therefore, the manipulation of the resonator length in a post-processing step is subject of the next section.

5.4 Adjustment of Fabry-Pérot mode frequencies by polishing the front facet

5.4.1 Introduction

As described in the previous section, cleaving—part of the established fabrication method—limits the precision with which the length of a Fabry-Pérot resonator can be defined. For an enhanced control of the modes, an additional method to modify the resonator length is required. Since the precise prediction of the Fabry-Pérot mode frequencies on the GHz scale is very difficult only from the measurement of the QCL geometry due to uncertainties in the measurements and material parameters, the emission spectra have to be measured first to determine the required change in the resonator length. For that purpose, the QCL needs to be soldered to the submount and be wire-bonded. Therefore, the method for the modification of the resonator lengths needs to be compatible with that configuration. Ideally, the method for the length modification should have a precision below 1 µm to control the emission frequency with a precision on the order of 1 GHz. Furthermore, the method should enable a length modification by at least 15 µm in order to shift the modes by about one mode spacing so that any frequency within the operating frequency range of a specific QCL is accessible.

There are several semiconductor device fabrication technologies that come into consideration to modify the resonator length. First, a material may be deposited onto the facet to increase the resonator length. However, the length of a Fabry-Pérot resonator may only be

considered as increased if there are no reflections at the interface between the QCL facet and the deposited material. Otherwise, the additional layer may rather act as an interference filter, either enhancing or reducing the outcoupling. In order to avoid these reflections, the material must be impedance matched to the waveguide mode of the QCL, which means that the refractive index must be identical or very similar to the effective refractive index of the waveguide mode. In addition, deposition techniques in semiconductor technology such as sputtering are designed to produce rather thin layers well below 1 µm. Layer thicknesses of several µm are therefore difficult to achieve.

Instead of increasing the resonator length, it may also be reduced. For the removal of material, semiconductor device fabrication technology provides wet or dry etching. However, an important disadvantage of these methods is the different etching rates of semiconductors and metals. In the single-plasmon waveguide, apart from the semiconductor layers, the top metal plays an important role in the waveguiding process. In an as-cleaved ridge-type QCL, the longitudinal ends of the metal and semiconductor layers are located in the facet planes. This may be no longer the case after etching due to the different etching rates. Therefore, the resonator would not be clearly defined anymore, which may lead to undesired effects especially if the length has to be modified by several µm. In case of wet-etching techniques, a further challenge lies in the mostly isotropic removal of material. Therefore, the etching agent may attack not only the front and back facet, but also other semiconductor surfaces. One of these surfaces is the highly doped bottom contact layer, which ensures the electrical injection from the bottom metal contact layer to the active region. Part of this layer would also be removed during wet-etching, which would impede current injection. An anisotropic dry-etching technique is inductively-coupled-plasma (ICP) reactive-ion (RIE) etching . However, the large amount of metal that has to be introduced into the etching machine due to the presence of the submount is undesirable in ICP RIE processes. In addition, machines for ICP RIE processes are designed for wafers, which can lead to problems due to the different geometry of a mounted QCL.

A further possible technique to reduce the resonator length is mechanical or chemical-mechanical polishing, which is employed, for example, in semiconductor device fabrication technology or for the preparation of samples for microscopic examination. This method has the advantage that it can create planar surfaces also if several different materials are present. In addition, there is in principle no limit for the maximal amount of material that can be removed. Therefore, polishing is investigated as a method to reduce the resonator length particularly with regard to the achievable precision. A particular goal of the polishing experiments is also to adjust the emission frequency of one Fabry-Pérot mode so that it reaches a frequency within several GHz of the target frequency. Such a QCL may be employed as a local oscillator for the heterodyne detection of the astronomically important transition in atomic oxygen at 4.745 THz. To perform such a measurement, the emission frequency of the QCL should be detuned according to the sensitivity maximum of the employed high-frequency detector. Therefore, the selected target emission frequency of the QCL amounts to 4.742 THz.

After an introduction to the technical and experimental aspects of the polishing in subsection 5.4.2, the results of six subsequent polishing runs are presented in subsection 5.4.3, and the corresponding results are discussed in subsection 5.4.4.

5.4.2 Experimental methods

Polishing technique

The polishing technique is based on the methods employed for the preparation of specimens for transmission electron microscopy. Figures 5.7(a) and 5.7(b) depict the polishing holder made from brass viewed from the side and from the top, respectively. Since the QCL front facet needs to be horizontally aligned for a uniform polishing, the holder is equipped with two spacers made of polytetrafluoroethylene (PTFE), which can be vertically moved by hand screws. The hand screws can be turned in small and reproducible steps via a latching mechanism shown in Fig. 5.7(b). The measurement of the inclination with respect to the horizontal plane is performed using an electronic tilt sensor with an angular resolution of 0.1°, while the holder stands on a glass plate. For polishing, the holder is put and held by hand on the rotating plate of the polishing/grinding machine Buehler EcoMet 250, which can be equipped with different polishing films or papers as depicted in Fig. 5.7(c). The rotation direction with respect to the orientation of the polishing holder is also shown in Fig. 5.7(c). The polishing experiments were performed with UltraPrep Diamond lapping films with grain sizes of 0.1 or 0.5 µm. The polishing holder was positioned such that the QCL is located at a distance of about 4 to 5 cm from the center of the rotating plate.

Figures 5.7(d) and 5.7(e) show two options for mounting the QCL chip for polishing. The first option is to mount the QCL chip on the submount edge as shown in Fig. 5.7(d). In that case, the front side of the submount is also polished along with the front facet of the QCL. Since the front side of the submount has a large area (22×2 mm^2) as compared to the front facet of the QCL chip (typically 2×0.35 mm^2), the material removal rate for polishing with small grain sizes below 1 µm is very low and therefore unpractical. For polishing/grinding with grain sizes such as 15 µm (SiC grinding paper), the material removal rate is increased, but the top gold of the QCL is easily damaged, and the roughness of the front facet becomes quite large. These disadvantages do not apply if the QCL is mounted with a small overhang as shown in Fig. 5.7(e). This second option is therefore preferable and used in the experiments presented here.

Control and monitoring of the polishing process

The achievable precision with regard to the control of the Fabry-Pérot mode frequencies is determined by the degree of control with which the resonator length can be reduced. In general, the removed amount of material by polishing increases with time, grain size, rotation speed of the polishing plate, and pressure exerted on the sample. The adjustment of the pressure exerted on the sample is rather cumbersome, since it is mainly determined by the geometry of the polishing holder and the weight of the material from which it is made. In contrast, the grain size and the rotation speed can be rather conveniently adjusted.

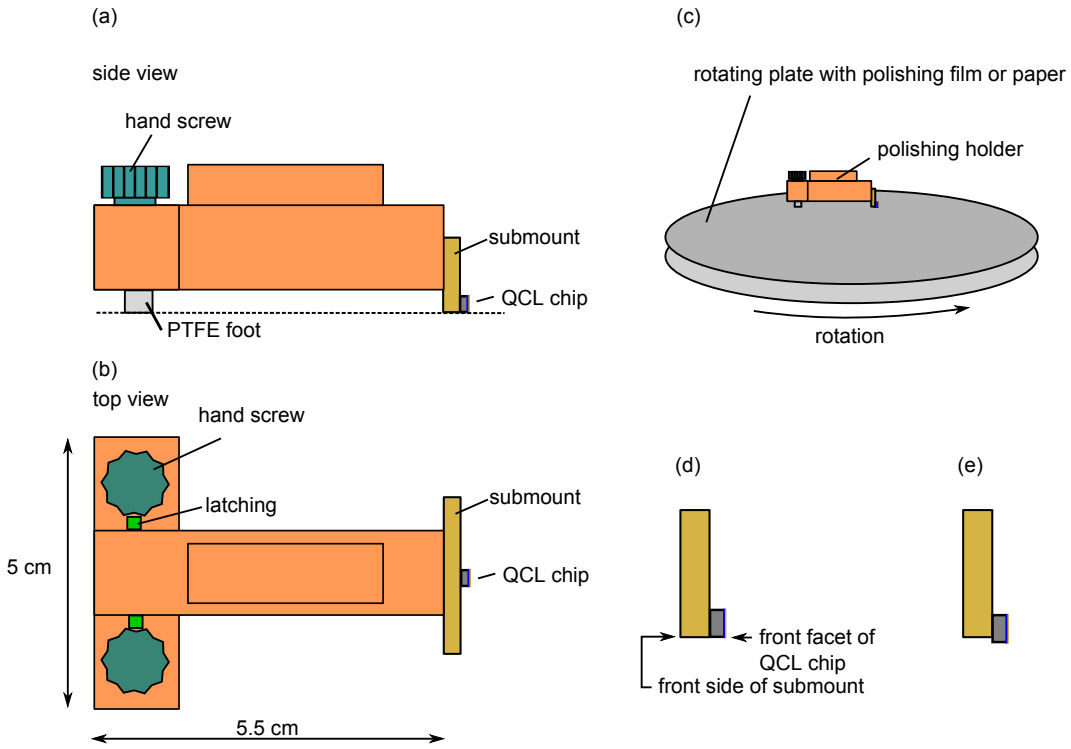

Figure 5.7: (a) Side view and (b) top view of a schematic of the polishing holder. (c) Schematic of the polishing process. The QCL mounted on the polishing holder is put on a rotating table with a polishing film or paper. (d) and (e) schematic of the QCL chip mounted on the submount edge and mounted with an overhang, respectively.

In order to control the amount of the removed material with a precision of at least 1 µm, a polishing rate on the order of 1 µm/min appears suitable. Thus, preliminary experiments were performed to identify the parameters to obtain this particular polishing rate, which yielded a grain size of 0.5 µm at a rotation speed of 10 rpm as well as a grain size of 0.1 µm at a rotation speed of 30 rpm.

There are several approaches to measure the removed amount of material, i.e., the reduction of the resonator length due to polishing. One option is to employ an optical microscope for that purpose. Figure 5.8 shows a schematic of the employed microscope, which is equipped with an electronically encoded vertical focus position. The resolution of the electronic encoding amounts to 1 µm. For a measurement of the length reduction of the resonator, the microscope is focused to the front side of the submount first, which represents the reference plane. This step is shown in Fig. 5.8(a). By focusing on the front facet of the QCL as shown in Fig. 5.8(b), its vertical position relative to the front side of the submount can be measured. From this relative position, the length reduction of the resonator is obtained, since the submount is not polished and therefore remains unaltered. While the

electronic encoding of the focus position in principle allows for a measurement precision of ± 1 µm, it turned out to be very difficult to place the sample under the microscope in a reproducible way. Therefore, the measurement of the length reduction employing the described microscope only features a precision of ± 3 µm. Consequently, this method for the measurement of the length reduction is mainly helpful if larger amounts of material have to be removed.

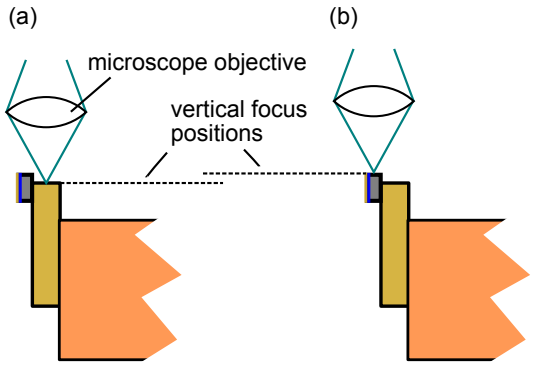

Figure 5.8: Principle of the measurement of the length reduction by a microscope with encoded focus position. (a) The front side of the submount represents the reference point. (b) The position of the front facet is measured with respect to the front side of the submount.

A second approach to measure the amount of removed material is to infer it from the measurement of the emission spectrum of the QCL. While the amount of removed material is only measured indirectly with this approach, it directly provides information about the deviation of the mode frequency from the target frequency. In order to conveniently measure the emission spectrum of a QCL after a polishing run, the vacuum chamber of the Stirling cooler was adapted so that the QCL could be operated while mounted on the polishing holder. This approach facilitates repeated alternating polishing and measurement runs. In addition, this approach in principle avoids the error that would be introduced by the required realignment of the QCL for further polishing. For the measurements of the emission spectrum while the QCL is mounted on the polishing holder, pulsed operation is employed, because the thermal coupling of this setup is reduced with respect to a direct mounting of the QCL on the cryostat cold finger. The difference of the emission spectrum between pulsed and continuous-wave operation of the QCL is investigated in subsection 5.4.3.

There is an important detail related to the above approach of mounting the polishing holder within the vacuum chamber of the Stirling cooler. In fact, because of the presence of the vacuum in conjunction with the vibrations of the Stirling cooler, one or both PTFE spacers may be partially pulled out of the polishing holder so that the alignment may be significantly altered. However, this effect can be prevented by introducing an evacuation channel into the spacers, which is for example also performed for screws used in ultra-high vacuum setups.

Despite all the efforts described above to maintain the alignment also during alternating polishing and measurement runs, the front facet is not uniformly polished at all times. Instead, the polishing starts at one corner or edge of the facet and progresses over the facet with time. This effect is probably due to the rotatory movement of the polishing film, which favors a specific corner or edge for the polishing process. In addition, the polishing process is influenced by different pressures and holder orientations, since the holder is placed and held by hand on the polishing film. These effects compromise the reliability and reproducibility of the polishing using time as the control parameter. In order to tackle this problem, a method referred to as *alternating-grain-size technique* has been developed, which provides enhanced control over the removed amount of material.

Figure 5.9 illustrates the alternating-grain-size technique. The blue circle marks the ridge with a width of 120 µm, which is investigated in this section. The chip facet shown in Fig. 5.9 was first polished with a grain size of 0.1 µm and afterwards with a grain size of 0.5 µm for a limited time. The polishing advances from the top left corner toward the bottom right corner of the chip facet as indicated by the red arrow in Fig. 5.9. Since the roughness created by the polishing with a grain size of 0.5 µm is different from the roughness created with the grain size of 0.1 µm, the progress of the polishing can be monitored by regularly interrupting the polishing and investigating the facet under the microscope. The polished area of the chip facet (either the complete chip facet or a fraction thereof) can be taken as a control parameter to determine the removed amount of material, i.e., the reduction of the resonator length. Since the method is based on selecting a different grain size than in the polishing run before and observing the change in the roughness of the chip facet as it progresses from one corner toward the remaining chip facet, a different roughness has to be selected once the roughness of the facet has changed completely. In conclusion,

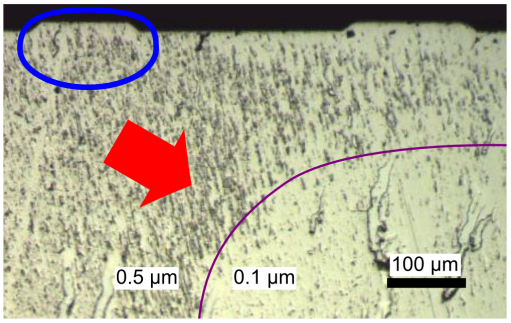

Figure 5.9: Example of an optical microscope image of the front facet. The blue circle indicates the investigated QCL ridge with a width of 120 µm. First, the facet has been polished with a grain size of 0.1 µm and afterwards with a grain size of 0.5 µm. The polishing advances in the direction indicated by the red arrow. The region already polished with 0.5 µm grain size can clearly be distinguished from the region previously polished with 0.1 µm, as indicated by the purple line.

the alternating-grain size technique can be employed to reduce the resonator length in reproducible steps. This is achieved via monitoring the progress of the polishing process by regularly investigating the change of the roughness of the polished surface. After the desired area has been polished, the grain size of the polishing film is changed so that the progress of the polishing can again be monitored. The application of the alternating-grain-size method to adjust the emission frequencies of a THz QCL is described in subsection 5.4.3.

Employed QCL and measurement parameters

For the polishing experiments, a QCL with a single-plasmon waveguide and a Fabry-Pérot resonator, which was fabricated from the wafer M4.2594, is employed. Its width and initial length amounts to 120 and 1,585 µm, respectively. The QCL emits around 4.7 THz. For all pulsed measurements, the Avtech AV-107C-B current pulse driver was employed with a pulse width of 1 µs and externally triggered at a frequency of 50 kHz. The continuous-wave measurements were performed with the Keithley source measure unit 2635A. The measurements of the optical power, current-voltage characteristics, and the spectra in pulsed operation are performed using the Stirling cooler, while the helium flow cryostat is used for the measurement of the spectra in continuous-wave operation. The optical path between the cooling system and the spectrometer or the power meter is flushed with nitrogen to reduce absorption by water vapor in air.

5.4.3 Polishing experiments and results

Polishing experiments

In order to investigate the influence of the polishing on the Fabry-Pérot modes, six alternating polishing and measurement runs of the emission spectrum were performed. Table 5.1 summarizes the grain sizes, rotation speeds, and polishing times employed in the different polishing runs. Based on the initially measured emission spectrum of the QCL, the required

Table 5.1: Employed parameters for the different polishing runs.

Polishing run No.	Grain size (µm)	Polishing time (s)	Rotation speed (rpm)
1	0.5	20 260	30 10
2	0.1	300	30
3	0.5	40	10
4	0.1	20 30	10 30
5	0.5	20	10
6	0.1	20 25	10 30

reduction of the the resonator length to obtain an emission mode at the target frequency of 4.742 THz was estimated and amounts to about 6 µm. While the goal of the polishing runs 1 and 2 was to coarsely remove several µm, the remaining polishing runs aimed at approaching the target frequency in small steps by employing the alternating-grain-size technique. Polishing run 1 was performed with a grain size of 0.5 µm at a rotation speed of 30 rpm for 20 s at first and 10 rpm for 260 s afterwards. The reduction of the resonator length as measured by means of the microscope with electronically encoded focus amounts to (5 ± 3) µm. For polishing run 2, a grain size of 0.1 µm at a rotation speed of 30 rpm was employed. Due to issues with the alignment of the QCL chip, the polishing time was quite long and amounted to about 300 s.In polishing runs 3 and 4, the polishing was per-

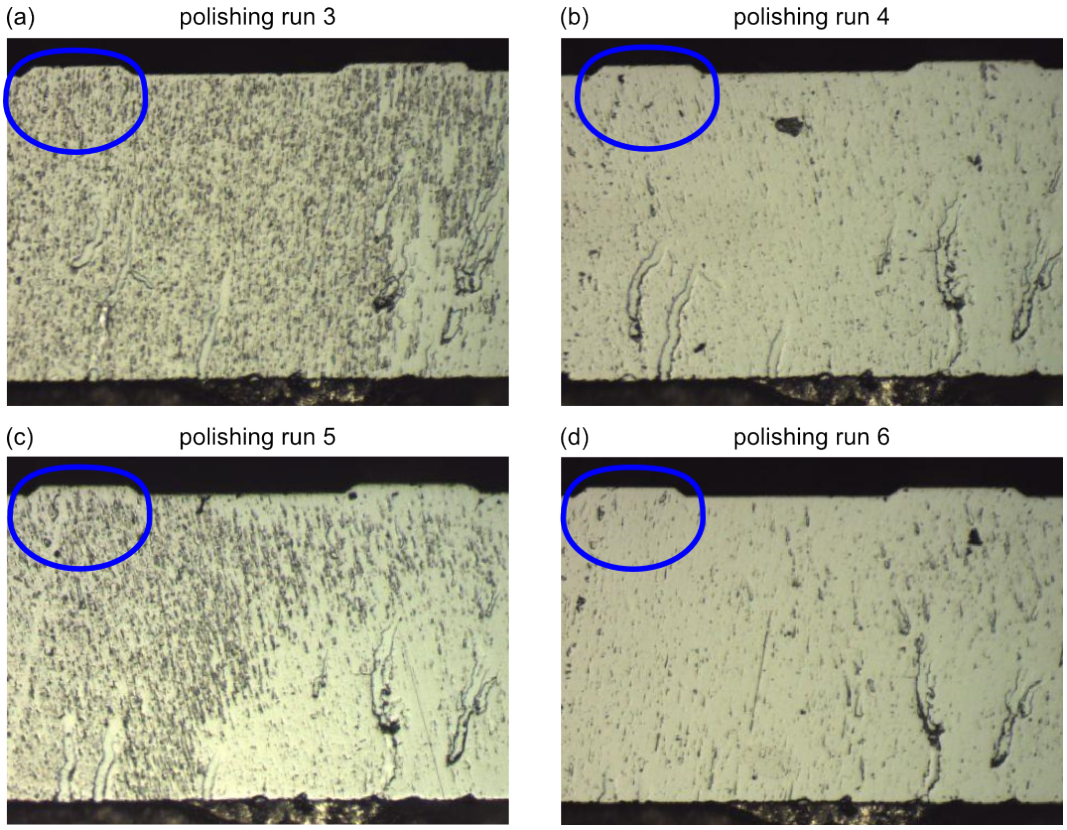

Figure 5.10: Optical microscope images of the QCL chip front facet taken after the polishing runs (a) 3, (b) 4, (c) 5, and (d) 6.

formed with the alternating-grain-size method until the polishing progressed to about half of the chip facet. In order to allow for the monitoring of the process in polishing run 3, a grain size of 0.5 µm was selected, since polishing run 2 was performed with a grain size of 0.1 µm. Figure 5.10(a) shows an optical microscope image of the facet after polishing run 3. The polishing started at the left-hand side of the chip and advanced toward the right-hand

side. The total polishing time amounts to 40 s at 10 rpm. For polishing run 4, the grain size has been changed to 0.1 µm.

It is important to realize that not the whole area of one of the front or back facets of the chip, but rather only part of it represents the "mirrors" of the Fabry-Pérot resonator. The blue circles in Figs. 5.10(a)–5.10(d) mark that part, which contains the QCL ridge itself as well as a region up to about 100 µm below the ridge. Since the waveguide mode is not restricted to the ridge, but rather extends to a certain amount into the substrate, the part marked by the blue circle constitutes the area that the waveguide mode occupies. Only alterations within that area modify the "mirror" of the laser resonator and therefore the Fabry-Pérot modes, since the intensity of the waveguide mode is negligible outside that area. While for polishing runs 3 and 4 the polishing was performed until it progressed from the left hand side to the center of the chip facet, for polishing runs 5 and 6 the polishing was already stopped after it progressed beyond the area marked by the blue circle as shown in Fig. 5.10(c) and 5.10(d). With this approach, the smallest possible steps in the reduction of the resonator length for the grain sizes of 0.5 and 0.1 µm are obtained in polishing runs 5 and 6, respectively.

Emission spectra

Figure 5.11(a) shows the emission spectra of the QCL before polishing (polishing run 0) in two configurations. In the first configuration, the QCL is located directly on the cold finger of a helium flow cryostat. The QCL is operated in continuous-wave mode as also required for the intended application. The second configuration is employed to allow for the alternating polishing and measurement runs as described above. Here, the QCL is cooled while mounted on the polishing holder, which in turn is fixed to the cold finger of the Stirling cooler. Due to the somewhat reduced thermal contact in this configuration, the QCL is operated in pulsed mode.

For continuous-wave operation at the current densities of 231 and 284 $\mathrm{A\,cm^{-2}}$, the emission spectra exhibit only a single mode at a frequency at about 4.74 THz as shown in Fig. 5.11(a). Two additional modes at lower frequencies appear at the current densities of 336 and 368 $\mathrm{A\,cm^{-2}}$. The spacing of the modes amounts to about 20 GHz. Thus, the observed modes can be assigned to successive Fabry-Pérot modes of order $M_0 - 1$, M_0, and $M_0 + 1$, since the value for the mode spacing obtained from the simulations [cf. Fig. 5.3(b) for a resonator length of 1,585 µm] amounts to 23 GHz and is therefore very similar to the value obtained from the measured emission spectra. The difference of 3 GHz between the measured and simulated mode spacing is attributed to cavity pulling due to the optical gain [89], which is not considered in the simulations.

For pulsed operation with the QCL mounted onto the polishing holder, three current densities were selected. The spectra exhibit only a single mode for all three current densities, which is attributed to the higher cold finger temperature and the lower thermal contact as compared to the measurements for continuous-wave operation with the QCL mounted directly on the cold finger. For 260 and 280 $\mathrm{A\,cm^{-2}}$, the mode has a frequency of about 4.74 THz similar to the mode observed in continuous-wave operation at 231 and 284 $\mathrm{A\,cm^{-2}}$. At 300 $\mathrm{A\,cm^{-2}}$, the frequency of the mode is reduced by about 20 GHz with

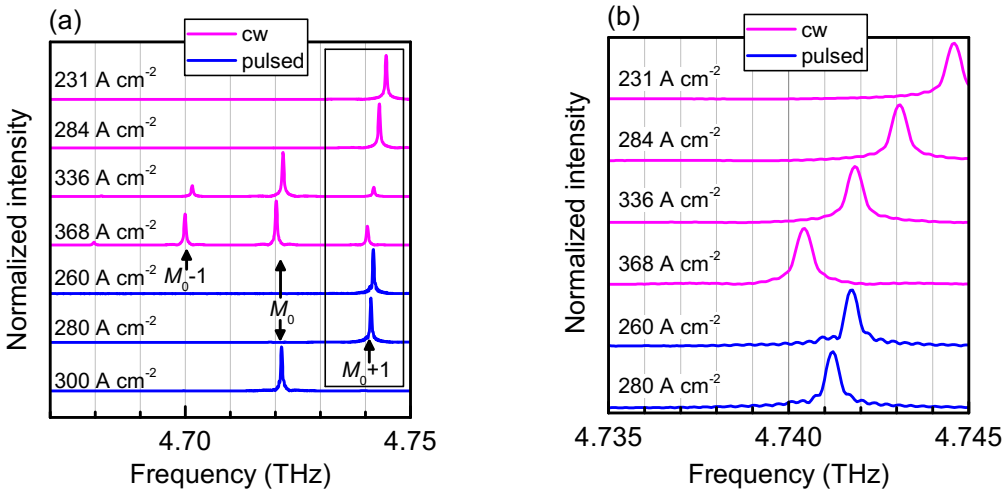

Figure 5.11: Measurements of the emission spectra for continuous-wave and pulsed operation before polishing. (a) Overview of the emission spectra for different current densities. The mode orders $M_0 - 1$, M_0, and $M_0 + 1$ have been assigned to the observed Fabry-Pérot modes. (b) Magnification of the relevant spectral range for the Fabry-Pérot mode of order $M_0 + 1$. The measurements in continuous-wave operation have been performed in the helium flow cryostat at 35 K and the pulsed measurements in the Stirling cooler at 40 K with the QCL mounted onto the polishing holder.

respect to the modes present at 280 A cm^{-2} and is located at about 4.72 THz, which is similar to the frequency of the Fabry-Pérot mode of order M_0 in the continuous-wave spectra at 336 and 368 A cm^{-2}. Thus, the observed reduction of the mode frequency by about 20 GHz is clearly due to a reduced Fabry-Pérot mode order, which changed from $M_0 + 1$ to M_0. This effect will be referred to as mode hopping.

Figure 5.11(b) shows a magnified frequency range of the mode at the highest frequency, indicated by the rectangle in Fig. 5.11(a). In continuous-wave operation, there is a red shift of about 4 GHz for increasing current densities from 231 to 368 A cm^{-2}. In pulsed operation, the mode shifts to lower frequencies by about 0.5 GHz for increasing current densities from 260 to 280 A cm^{-2}. The red shift of the mode frequencies with increasing current densities observed in Fig. 5.11(b) is due to a change of the effective refractive index of the waveguide mode, which modifies the optical length of the resonator. This dynamical tuning is a further effect for increased current densities in addition to the appearance of additional Fabry-Pérot modes or "hopping" to a mode of a lower order, which were already discussed.

The observed differences between the emission spectra in pulsed and continuous-wave operation are no obstacle for the approach to measure the emission spectrum with the QCL mounted on the polishing holder, for which pulsed mode is required, because the measured

differences can be used to predict the spectrum that will be obtained in continuous-wave mode from the measured spectra in pulsed mode. This is readily possible, since the mode spacing is altered only very little for the small reductions of the resonator length performed here.

Figure 5.12(a) shows the emission spectra measured before polishing (polishing run 0) and after each of the six polishing runs for current densities of 260, 280, and 300 $\mathrm{A\,cm^{-2}}$ in pulsed operation with the QCL mounted onto the polishing holder. Figure 5.12(b) displays the mode frequencies extracted from Fig. 5.12(a) as a function of the polishing run. The spectra for all current densities and all polishing runs exhibit only a single mode. As explained earlier, the large frequency difference between the modes of polishing run 0 (before polishing) appearing at the current densities of 280 and 300 $\mathrm{A\,cm^{-2}}$ originates from the different order M of the modes. The order of the mode at 300 $\mathrm{A\,cm^{-2}}$ is denoted M_0, while at 260 and 280 $\mathrm{A\,cm^{-2}}$ the mode order is $M_0 + 1$. The modes appearing for the polishing runs 1 to 6 are of order M_0. Therefore, all modes in the spectra measured at 300 $\mathrm{A\,cm^{-2}}$ as shown in Fig. 5.12(a) are of the same order M_0.

If the modes of polishing runs 1 to 6 are considered, the modes are shifted toward lower frequencies by roughly 1 GHz for increasing current densities as can be seen in Fig. 5.12(b). The value of 1 GHz for the frequency shift varies by up to 50% due to the limited precision

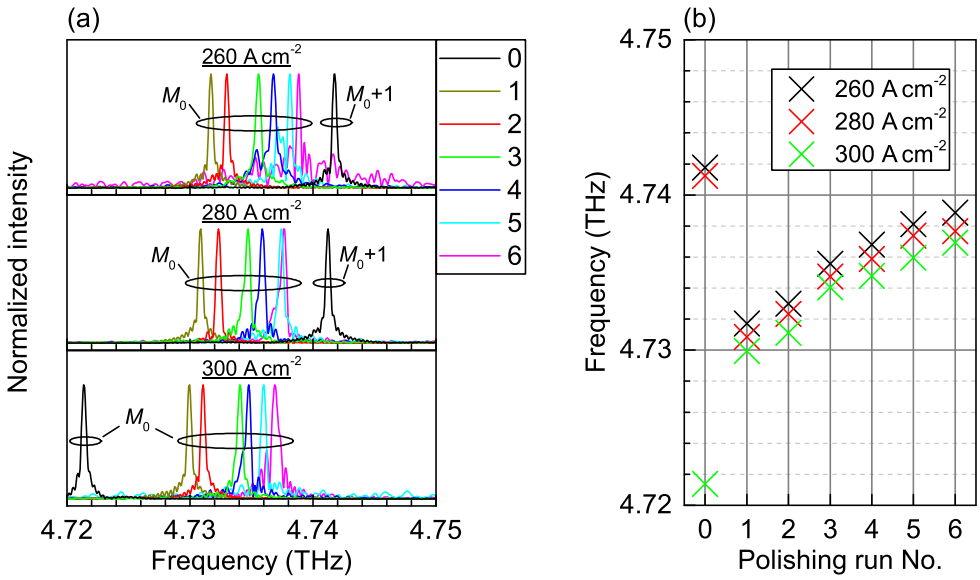

Figure 5.12: (a) Comparison of the spectra before the polishing (referred to as polishing run 0) and after the polishing runs 1 to 6 as indicated. The spectra were taken with the QCL mounted onto the polishing holder and operated in the Stirling cooler at a cold finger temperature of 40 K. For each polishing run, three spectra at 260, 280, and 300 $\mathrm{A\,cm^{-2}}$ have been measured. (b) Mode frequencies extracted from (a).

of the current and frequency measurement. The spectra measured before polishing (polishing run 0), which have already been shown in Fig. 5.11(a), are also displayed in Figs. 5.12(a) and 5.12(b) for comparison with the spectra after the different polishing runs. The large frequency difference between the modes occurring at 260/280 and 300 A cm^{-2} is due to the reduction of the Fabry-Pérot mode order by 1 (mode hopping) as explained earlier.

In order to qualitatively understand the effect of the frequency shift, the spectra shown for a current density of 300 A cm^{-2} in Fig. 5.12(a) are most suitable, since all modes are of the same order M_0. For consecutive polishing runs, the mode is shifted toward higher frequencies as expected for decreasing resonator lengths. This frequency shift is quite large for polishing run 1 and smaller for the subsequent polishing runs. For a quantitative analysis, the incremental frequency shifts for consecutive polishing runs are displayed in Fig. 5.13 for all three current densities. The shift for polishing run 1 amounts to about +8.5 GHz (blue shift) at 260 A cm^{-2} as well as about −10 and −10.5 GHz (red shift) for 280 and 300 A cm^{-2}. The red shift is again due to mode hopping. For polishing runs 2 to 6, the values of the frequency shift are very similar for all current densities. Figure 5.13 also shows the average of the frequency shifts for the three current densities, which will be the basis for the determination of the length reduction achieved with every polishing run.

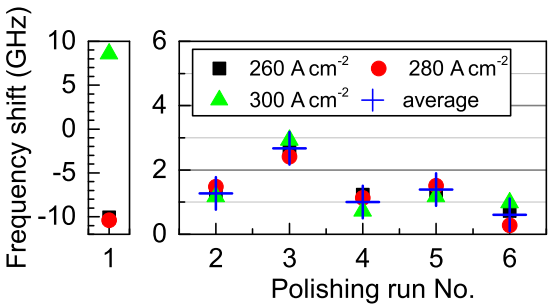

Figure 5.13: Incremental frequency shift of the modes after each polishing run extracted from Fig. 5.12(b).

According to Fig. 5.12(b), the mode position after polishing run 6 is located at about 4.739 THz for a current density of 300 A cm^{-2} in pulsed operation. This value is already close to the target frequency of 4.742 THz. Since the tuning range extends to higher frequencies in continuous-wave operation, the target frequency is expected to be achievable. Therefore, the QCL was removed from the polishing holder to investigate the spectra in continuous-wave operation. As shown in Figure 5.14, the target frequency is reached by a mode in continuous-wave operation at a current density of 237 A cm^{-2}.

Figures 5.15(a) and 5.15(b) show the emission spectra in continuous-wave operation before the polishing and after the sixth polishing run, respectively. All modes that were present before the polishing also build up after polishing. This result confirms that no additional losses were introduced by polishing. In the spectra after polishing, the modes have a somewhat lower frequency as the modes before polishing, which can be understood as follows.

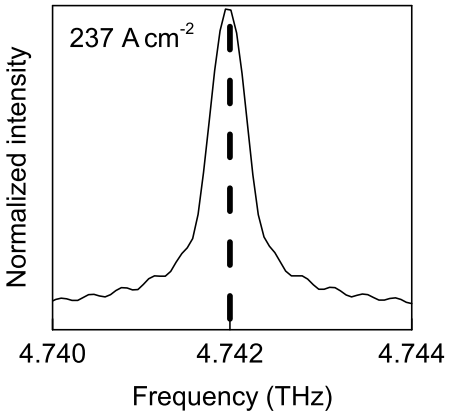

Figure 5.14: Emission spectrum measured at a cold finger temperature of 35 K with the QCL mounted in the helium flow cryostat. The QCL was operated in continuous-wave mode at 237 A cm^{-2}.

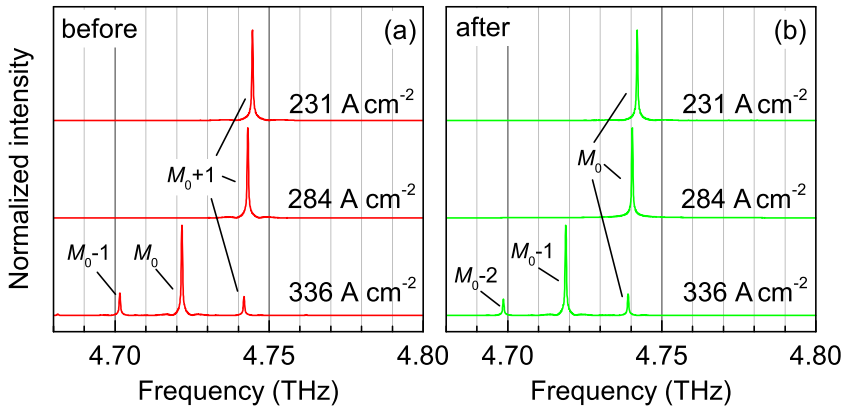

Figure 5.15: Emission spectra of the QCL in continuous-wave operation (a) before polishing and (b) after the polishing run 6. The QCL was mounted in the helium flow cryostat operated at 35 K.

As already established, a mode of a specific order M is shifted toward higher frequencies for a reduction of the resonator length. If this shift is approximately equal to a mode spacing, the initial modes are "replaced" by modes with order $M-1$. For example, consider the current density of 336 $\mathrm{A\,cm^{-2}}$ and the modes of order M_0 and M_0+1 in Fig. 5.15(a). As the mode of order M_0+1 is shifted toward higher frequencies, it leaves the spectral region with sufficient gain so that it can no longer build up. Instead, the mode of order M_0 shifts toward the initial frequency of the mode M_0+1 for decreasing resonator lengths. Therefore, as displayed in Fig. 5.15(b), the modes appearing at similar frequencies correspond to mode orders that are decreased by 1. Another aspect of the spectra is the mode spacing. For the spectra before and after polishing at a current density of 336 $\mathrm{A\,cm^{-2}}$, the mode spacing amounts to about 20.2 GHz with a variation of ± 0.1 GHz corresponding to the measurement error.

Output power and current density-voltage characteristics

For applications using QCLs as radiation sources, high powers are required to achieve high sensitivities. Therefore, it is important that the power is not reduced due to the polishing process. Figure 5.16(a) shows a comparison of the output power and current density-voltage (*L-J-V*) characteristics in pulsed operation before polishing and after the last polishing run (polishing run 6). In contrast to the measurements of the emission spectra in pulsed operation, which had been performed with the QCL mounted onto the polishing holder to allow for the alternating polishing and measurement runs, the QCL is now mounted directly on the cold finger of the Stirling cooler in accordance with the established setup of the *L-J-V* characteristics in pulsed operation. The voltage and power curves before and after polishing are very similar, which clearly shows that no detrimental effect of the polishing is present. Figure 5.16(b) displays the *L-J-V* characteristics in continuous-wave operation. While the voltage curves are again very similar, the power of the QCL after polishing appears to be higher than before polishing. This increase may be due to a modified purging of the optical path, leading to a decreased absorption by water vapor. A further explanation may be an enhanced thermal performance of the QCL after polishing due to the decreased resonator length, leading to a reduced overhang of the QCL chip with respect to the submount edge. An alternative explanation would be a different outcoupling efficiency due to the increased roughness of the facet, through which a layer acting as an effective anti-reflection coating is created. In that case, however, a similar difference in the power curves would be expected in pulsed operation, which is not observed in the measurement.

The *L-J-V* characteristics in pulsed and continuous-wave operation as displayed in Figs. 5.16(a) and 5.16(b) deviate from each other in several respects. First, the maximal voltage is somewhat higher, and the threshold as well as the maximal current density are somewhat lower in pulsed operation as compared to the continuous-wave measurements. The dynamic range, defined as the difference between the maximal current density and threshold current density, amounts to 110 for pulsed and 120 $\mathrm{A\,cm^{-2}}$ for continuous-wave operation. A possible origin of these differences is a somewhat lower temperature of the QCL chip in pulsed operation. The temperature is measured at the cold finger at some distance from the QCL chip itself, which usually has a somewhat higher temperature than the

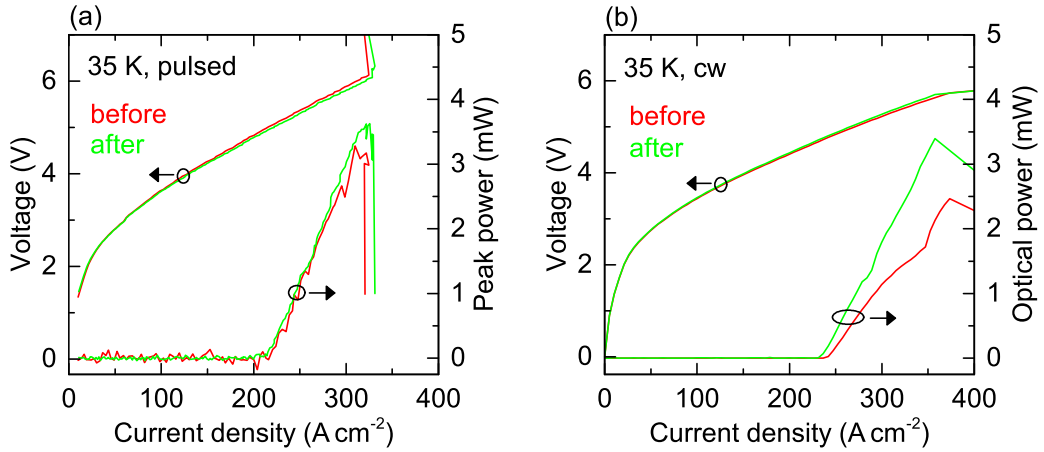

Figure 5.16: Optical output power and current density-voltage characteristics (a) in pulsed operation and (b) in continuous-wave (cw) operation. In both cases, the QCL was mounted onto the cold finger of the Stirling cooler and operated at a cold finger temperature of 35 K. The characteristics before the polishing and after polishing run 6 are compared. The pulsed measurements were performed at a repetition frequency of 50 kHz and a pulse length of 1 µs.

cold finger due to self-heating. This effect may explain the lower threshold current density in pulsed operation. An additional effect may appear due to the non-ohmic character of the QCL, which leads to non-perfect pulse shape including overshoot and may therefore lead to some deviations in the voltage measurement and an early onset of negative differential resistance. Thus, the dynamic range is reduced, and the voltage is overestimated in pulsed operation.

In summary, the measurements show that the output power is not reduced due to polishing and that the number of emission modes remains constant. For applications, a high output power ensures a good sensitivity, and the number of modes after polishing determines the frequency range, within which a certain target emission frequency can be reached. Thus, the introduced roughness by the polishing process has no detrimental effect, which can be understood by considering the wavelength of the THz radiation. At a frequency of 4.7 THz, the wavelength amounts to 64 and 17 µm in vacuum and in the waveguide, respectively. Therefore, roughness or imperfections that are clearly visible in the optical range are less important in the THz range due to the substantially larger wavelength, which explains the unaltered output power and mode number.

5.4.4 Analysis of the length reduction

In the last subsection, the shift of the emission frequencies due to the polishing has been analyzed. In particular, the incremental frequency shift of the modes after each polishing run has been discussed based on Fig. 5.13. It is interesting to investigate the corresponding

length reduction of the resonator. Since a direct measurement of the length reduction is difficult as described earlier, the length reduction is instead inferred from the average incremental shift of the modes for each polishing run as shown in Fig 5.13. This is done by a calculation similar to the one used for Fig. 5.4 in section 5.3 using the rigorous method. Figure 5.17 shows the results of this calculation. In polishing run 1, the resonator was shortened by about 3.3 µm. This value agrees with the value measured by means of the optical microscope, which amounts to (5 ± 3) µm. In polishing run 2, the resonator length was reduced by about 0.5 µm. This value is significantly lower than what would be expected from the polishing time of 300 s at 10 rpm according to the preliminary experiments. However, due to problems in the alignment of the QCL during polishing run 2, only a small corner of the facet was polished at first so that only a very small amount of material was removed from the relevant areas of the facet.

For the remaining polishing runs, the alternating-grain-size technique has been employed. For polishing run 3, a grain size of 0.5 µm has been used. The polishing was stopped until it had progressed over about half the facet. The corresponding length reduction amounts to 1 µm as shown in Fig. 5.17. In contrast, polishing run 5, which was also performed with a grain size of 0.5 µm, was already stopped as soon as the polishing had progressed over the area representing the "mirror" of the Fabry-Pérot resonator. Consequently, the length reduction amounts to only 0.5 µm, which is only half of the value obtained in polishing run 3. The same argument applies to the polishing with the grain size of 0.1 µm as employed for polishing runs 4 and 6. In polishing run 4, for which a larger area of the facet was polished, the length reduction amounts to about 0.4 µm, while polishing run 6 was stopped already when the relevant area was polished so that the length of the resonator was only reduced by about 0.2 µm.

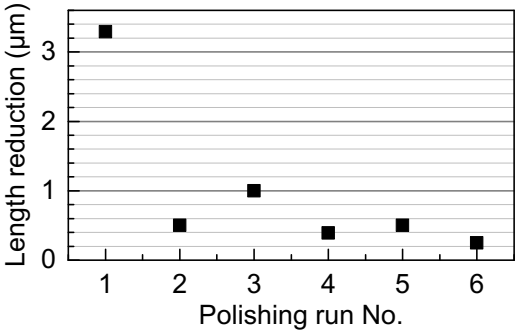

Figure 5.17: Length reduction of the resonator due to polishing derived from the average values of the mode shift taken from Fig. 5.13 by employing the simulation results of the rigorous method, which was presented in section 5.3.

These results of the experiments using the alternating-grain-size technique suggest that reliable length reductions at steps of about 0.5 and 0.2 µm are achievable. These values correspond to a frequency shift of 1.4 and 0.6 GHz for the investigated QCL emitting around 4.7 THz. Since the grain sizes have to be alternated, the achievable precision in the total

length reduction is determined by the larger grain size. The steps of the length reduction may be further decreased if less pressure is applied between the QCL and the polishing film. This can be achieved by using a polishing holder made from a lighter material such as aluminum instead of brass.

The length difference necessary to obtain a specific frequency shift decreases with the emission frequencies as shown in Fig. 5.4 of section 5.3. Therefore, QCLs with an emission frequency below 4.7 THz will exhibit a reduced frequency shift for the length reduction obtained here, through which the achievable precision for the adjustment of the Fabry-Pérot modes is increased. Conversely, the corresponding precision is decreased for QCLs emitting at higher emission frequencies.

5.5 Conclusions

In this chapter, the Fabry-Pérot mode frequencies have been investigated as a function of resonator length and waveguide width, also taking into account waveguide dispersion. While the exact mode frequencies depend only weakly on the waveguide width, they depend very sensitively on the resonator length. Due to this dependence, two Fabry-Pérot QCLs with a length difference of only 0.1% (for instance, 1,000 and 1,001 µm) can differ in emission frequency by several GHz, which can amount to more than 10% of the mode spacing (for example at 4.5 THz). Due to the special waveguiding principle in single-plasmon waveguides, the resonator length must be defined by cleaving, which has a precision of several µm at best even with dedicated cleaving machines. Since a sufficiently precise control of the mode frequencies is therefore impossible during the fabrication of the QCL, a post-fabrication technique to adjust the mode frequency has been developed. This technique relies on mechanical polishing of the front facet, which allows for a reduction of the length in alternating steps of 0.5 and 0.2 µm, employing the newly developed alternating-grain-size method. With this method, a sufficient control of the resonator length is achieved so that the emission frequencies can be adjusted on the scale of 1 GHz without a detrimental effect on the output power. An outstanding feature of this method is the possibility to reduce the resonator size also by an in principle arbitrary amount, which is necessary if the as-cleaved length is unfavorable for post-fabrication techniques to obtain a certain emission frequency. This feature is not present for other post-fabrication techniques that come into consideration. The presented results are also important to obtain a specific predefined frequency for single-mode QCLs, since the methods to obtain single-mode operation can be considered as mode-selection techniques applied to an effective Fabry-Pérot resonator.

6 Terahertz quantum-cascade lasers as high-power and wideband, gapless sources for spectroscopy

6.1 Introduction

Many spectroscopic techniques rely on a powerful radiation source with a wide spectral coverage. In the THz frequency range, QCLs are promising sources for diverse spectroscopic applications due to their high emission powers.

Unprecedented resolution and sensitivity has been achieved due to the narrow linewidth of single-mode THz QCLs in continuous-wave operation. In order to obtain the spectrum of a gas absorption line, the laser mode can be continuously tuned over the line, which leads to a corresponding variation of the detector signal [92, 95, 97]. A QCL can also act as a local oscillator in a heterodyne detection scheme, in which the original spectrum is converted down to radio frequencies and then investigated by a spectrum analyzer [7, 20, 93, 96, 112]. This technique is employed to obtain the spectrum of, for example, black-body radiation transmitted through a gas cell or of THz radiation from outer space [7, 93, 112].

The achievable continuous coverage of these techniques is limited by the low intrinsic tuning range of THz QCLs in continuous-wave operation, which is usually below 5 GHz. Many techniques have been developed to increase the continuous tuning range, but it is either extended only moderately or the increase comes at the cost of high complexity, low emission power, low tuning speeds, or insufficient reproducibility [104, 113–119].

For the spectroscopy of absorption lines of gases and absorption bands of long molecules such as explosives, multi-mode QCLs covering a frequency range of several 100 GHz have also been employed [94, 120, 121]. However, the emission spectra exhibit gaps of more than 20 GHz. While spectral gaps on this order might be acceptable for the spectroscopy of slowly varying absorption bands, they prevent the application of THz QCLs as sources for versatile high-resolution spectroscopy. Multi-mode THz QCLs can also be operated as frequency combs, which are promising for high-resolution spectroscopy due to the small linewidths of their modes, but the problem of gaps between the modes remains [104, 122–124]. Using multiheterodyne spectroscopy (also known as dual-comb spectroscopy) with two QCL-based THz frequency combs, the transmission spectrum of an etalon could be measured at 23 points over a frequency range of about 200 GHz [101].

For wideband spectroscopy in the THz spectral range, Fourier transform spectroscopy is the established technique. Typically, radiation from a thermal emission source such as a globar is used, which is spectrally decomposed by means of a Michelson interferometer. In this chapter, a multi-mode THz QCL is realized that can be employed as a high-power re-

placement for conventional THz wideband sources used in Fourier transform spectroscopy. A gapless coverage over a range of 72 GHz at about 4.7 THz is achieved using a novel principle referred to as gapless time-averaged wideband (G-TAWB) operation, which is introduced in section 6.2. In section 6.3, the emission spectrum of the QCL in G-TAWB operation is analyzed, and its superiority to conventional sources in terms of signal-to-noise ratio, dynamic range, and reproducibility of the transmission spectra is demonstrated. Furthermore, since G-TAWB operation is based on a QCL with a large tuning range of the laser modes during a fast ramp of the injection current, the tuning mechanism is discussed, and the performance of several similar QCLs is compared to the QCL employed for G-TAWB operation in section 6.4. Section 6.5 deals with the analysis of the collection efficiency of the spectrometer, i.e., the fraction of the output power emitted by the QCL that is coupled into the spectrometer. This number is important, since increasing the collection efficiency results in a higher sensitivity. The achieved results are summarized in section 6.6.

6.2 Principle and setup

The employed multi-mode QCL is based on a Fabry-Pérot resonator. Figure 6.1(a) shows a sketch of a typical spectrum of a Fabry-Pérot resonator, which consists of several equally spaced modes. Equation 5.12 of chapter 5 leads to

$$\nu_M = \frac{cM}{2L_{\text{opt}}}\,, \tag{6.1}$$

where ν_M are the frequencies of the Fabry-Pérot modes of order M and $L_{\text{opt}} = nL$ is the optical path length determined from the effective refractive index n of the waveguide mode as well as from the length L of the resonator. The order of the Fabry-Pérot mode M represents the number of intensity maxima of the standing wave in the resonator and amounts to at least 100 for typical resonator lengths. Altering L_{opt} by a small amount dL_{opt} changes the frequency of a Fabry-Pérot mode by

$$d\nu_M = -\frac{cM}{2L_{\text{opt}}^2} dL_{\text{opt}}\,. \tag{6.2}$$

Neighboring Fabry-Pérot modes shift practically by the same amount, since $d\nu_{M+1} \approx d\nu_M$ for large M. If the collective shift exceeds the mode spacing as indicated in Figs. 6.1(b) and 6.1(c), the overall continuously covered frequency range is the product of the mode spacing and the number of active modes, which approaches the total width of the gain profile.

Using this quasi-continuous tuning scheme, a QCL can in principle be adjusted such that one laser mode operates at any desired emission frequency within the operating range. However, in contrast to conventional wideband sources for spectrometers, the QCL cannot emit a continuous spectrum at one point in time. In order to use the QCL as a high-power replacement for conventional spectrometer sources, the QCL must be tuned over a short time interval Δt, while the signal of the spectrometer detector is averaged over this time span as sketched in Fig. 6.1(d). If Δt is substantially smaller than the acquisition time of the

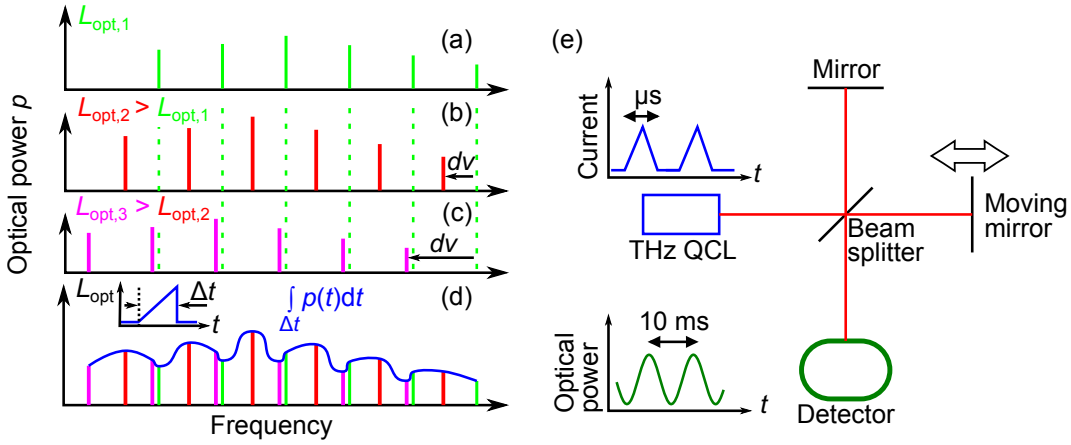

Figure 6.1: (a)–(c) Schematic emission spectra of QCLs with Fabry-Pérot resonators for increasing optical path lengths L_{opt}. The modes in (b) and (c) are collectively red-shifted by an amount $d\nu$, which can be larger than the mode spacing as shown in (c). (d) If the optical path length is continuously increased over a time Δt and the spectral power p is averaged over this time span, a wide, gapless spectrum may be generated, which is referred to as G-TAWB operation. (e) Setup for a Fourier transform spectrometer with a THz QCL under G-TAWB operation.

spectrometer, the emission spectrum appears to be continuous due to the averaging so that G-TAWB operation is obtained.

The main challenge to realize G-TAWB operation is to tune the discrete Fabry-Pérot modes over a frequency range which closes the spectral gaps between these modes. For about 3-mm-long Fabry-Pérot resonators, which are typical for pulsed-mode operation of THz QCLs, mode spacings of about 10 GHz are observed. The typically achievable current-induced tuning range for this kind of devices in pulsed operation is well below 10 GHz for many of the QCLs grown and investigated at the Paul-Drude-Institut. However, some QCLs exceed a tuning range of 10 GHz, from which the most suitable one is selected to demonstrate G-TAWB operation. A discussion of the tuning mechanism and a comparison of the emission properties of several QCLs with the ones of the QCL employed for G-TAWB operation is given in section 6.4.

Figure 6.1(e) depicts the experimental setup using a THz QCL in G-TAWB operation as a source for a Fourier transform spectrometer. The employed GaAs/AlAs QCL was fabricated from wafer M4.2949, which is the same wafer as the QCL with the lower doping density in Ref. [31]. The QCL with a single-plasmon waveguide has a width of 120 μm and a length of about 3 mm. The QCL is mounted on the cold finger of a helium flow cryostat operated at 10 K, which is placed in front of the external emission port of the spectrometer. The volume between the exit window of the cryostat and the entrance window of the evacuated spectrometer is purged with nitrogen to reduce absorption by water vapor in air. In order to realize the current ramp for G-TAWB operation, an ILX Lightwave LDP-

3840 pulsed driver is employed with the pulse width set to 1 µs and triggered at 300 kHz. Using a smoothening capacitor, the original rectangular pulse shape can be transformed into a triangular waveform, yielding a current ramp amplitude of about 1 A and a maximum voltage of about 8 V.

The time averaging is realized by employing a slow pyroelectric detector for the spectrometer, which does not follow the fast intensity changes due to the current ramp. The detector has its highest sensitivity for intensity variations between 10 and 100 Hz, which corresponds to the typical frequency range of the intensity variations due to the continuously moving mirror of the interferometer. The highest resolution of the employed spectrometer (Bruker IFS 120HR) is 0.105 GHz (0.0035 cm^{-1}). To compare the performance of the THz QCL in G-TAWB operation with a conventional source, a globar is employed, which is part of the spectrometer and therefore optimized to its optics and running at full capacity.

6.3 Quantum-cascade laser in gapless time-averaged wideband operation as a spectrometer source

Figure 6.2(a) shows the emission spectrum of the QCL in G-TAWB operation recorded with the highest resolution of the spectrometer. The measurement parameters have been chosen in such a way that any broadening effects are minimized. A continuous coverage of 72 GHz over the range from 4.686 to 4.758 THz is achieved. The spectrum is not smooth, since not only the position of the Fabry-Pérot modes, but also their power and number are a function of the injection current. This is also the reason why only part of the 200-GHz-wide emission spectrum displayed in the inset of Fig. 6.2(a) shows a gapless coverage.

Figure 6.2(b) shows the spectral power of the QCL in G-TAWB operation and of the high-performance thermal source (globar), which is delivered with the Fourier transform spectrometer, with a lower resolution than in Fig. 6.2(a). In comparison to the thermal source, the QCL exhibits one to two orders of magnitude higher powers. The spectrum of the thermal source is not smooth due to its low power, which is on the order of the detector noise. Note that the hatched rectangle in Fig. 6.2(b) marks a peak in the spectrum of the thermal source which is attributed to a pickup of the power line frequency in the detector circuitry, through which an additional signal is introduced into the interferogram. The peak in the spectrum shifts to another position outside the investigated spectral region if for example a scanner speed of 7.5 instead of 10 kHz is selected. This peak can therefore be neglected in the analysis.

An important criterion of a spectroscopic system is its signal-to-noise ratio (SNR), which is a measure for the ability to discern a weak signal from noise. It can be determined from several consecutively recorded spectra taken under the same conditions, from which then, for every point in frequency, the mean is divided by the standard deviation. Figure 6.3(a) shows the SNR of the QCL and the thermal source calculated from 10 consecutive measurements. As in Fig. 6.2(b), the variation of the SNR as a function of the frequency originates, in case of the QCL, from its varying power, and, in case of the thermal source, from its low output power, which is comparable to the detector noise. Over the complete frequency range, the SNR of the QCL is significantly higher than the SNR of the thermal

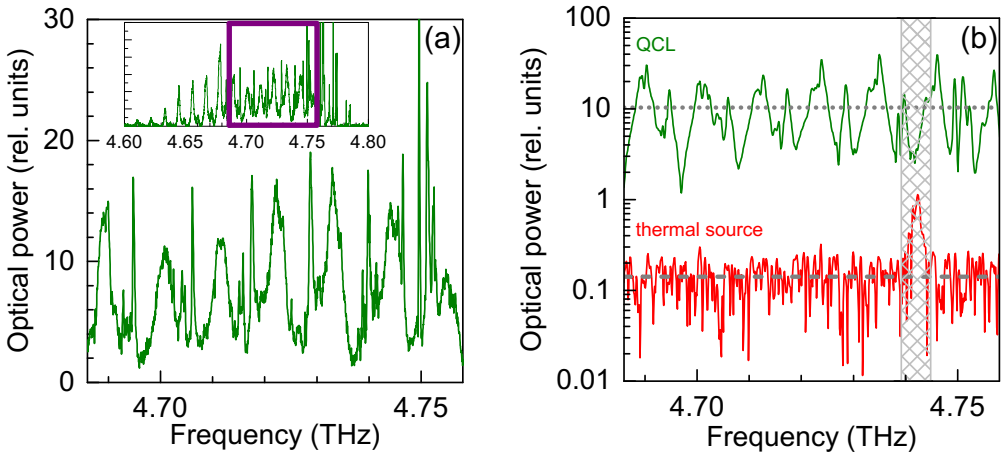

Figure 6.2: (a) Spectral power in relative units of the QCL in G-TAWB operation for a frequency range of 72 GHz (4.686 to 4.758 THz). In order to investigate the continuity of the emission spectrum, the highest possible resolution was chosen, which amounts to 0.105 GHz (0.0035 cm^{-1}). To minimize any broadening effects in the spectrum, the boxcar apodization, the Mertz phase correction, and an aperture of 8 mm are employed. The scanner speed is set to 10 kHz. Inset: Overview of the whole emission spectrum between 4.6 and 4.8 THz. The rectangle shows the gapless range of the spectrum. (b) Spectral power of the thermal source compared with the QCL in G-TAWB operation as measured with a spectral resolution of 0.3 GHz (0.01 cm^{-1}) and the same aperture as well as scanner speed as in (a). The hatched rectangle marks a peak in the spectra of the thermal source due to an electrical pickup and is therefore neglected in the analysis. The dotted and dashed lines mark the average spectral power of 10.4 for the QCL and 0.14 rel. units for the thermal source, respectively.

source. However, the SNR of the QCL as compared to the one of the thermal source is not as large as one may have expected from a comparison of their spectral power in Fig. 6.2(b). While the average spectral powers indicated by the dotted and dashed lines in Fig. 6.2(b) differ by a factor of about 75, the average SNR of the QCL is only a factor of about 20 higher than the average SNR of the thermal source. Since the measurements have been performed with the same spectrometer settings and detector, this difference must result from the noise of the QCL. More specifically, the averaged spectral power of the QCL in G-TAWB operation fluctuates in time, which is most likely due to a variation in the shape of the current pulses over time, which can be reduced by using a highly stable voltage-to-current converter. Note that the effect of the electrical pickup is only visible for the thermal source, since the QCL has a much higher emission power.

Apart from the SNR, the dynamic range is another important parameter for a spectroscopic system. To calculate the dynamic range, the detector noise level must be determined

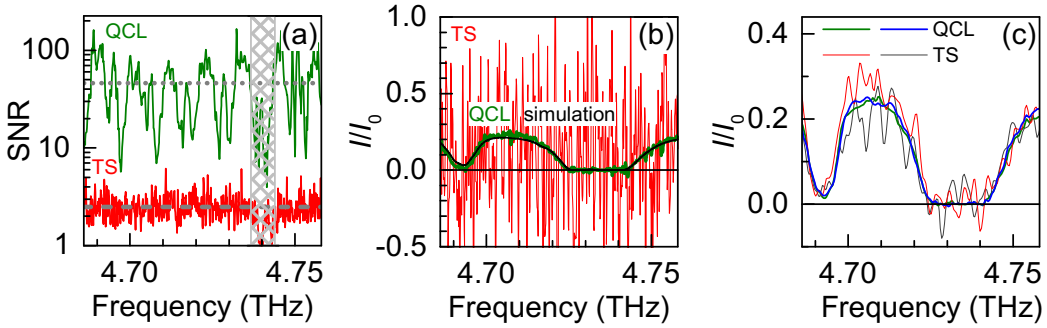

Figure 6.3: (a) Signal-to-noise ratio (SNR) as a function of frequency. The dotted and dashed lines mark the average SNR of 46 for the QCL and 2.5 for the thermal source (TS), respectively. The hatched rectangle is explained in the caption Fig. 6.2(b). (b) Transmission spectrum of air with 100% humidity in a 10-cm-long gas cell recorded with the TS and with the QCL in G-TAWB operation. The resolution is set to 0.3 GHz (0.01 cm^{-1}), the scanner speed to 7.5 kHz, and the aperture to 8 mm. The acquisition time amounts to 143 s. The black curve displays a simulated transmission spectrum. (c) Transmission spectrum of the same gas cell as in (b), but recorded with different parameters. The resolution is set to 1.5 GHz (0.05 cm^{-1}), the scanner speed to 2.2 kHz, and the aperture to 12.5 mm. In order to investigate the reproducibility, two measurements employing both, the QCL and the TS, are displayed.

while the radiation from the emission source is blocked. The dynamic range can then be calculated by dividing the spectral power by the measured noise level. It is therefore a measure of the maximal absorption which can be distinguished from noise. To determine the noise level of the employed detector, the radiation source was blocked at the entrance aperture of the sample compartment using an aluminum foil, whose low thermal emissivity ensures that no additional thermal radiation impinges on the detector. The noise level obtained by recording spectra in this configuration amounts to 0.04 relative units. Since the QCL power varies between 2 and 30 relative units according to Fig. 6.2(b), the resulting dynamic range lies between 50 and 750. In contrast, the thermal source has a power of about 0.14 relative units, leading to a dynamic range of only 3.5.

A characteristic property of the emission spectrum of the QCL in G-TAWB operation as compared to the spectrum of the thermal source is its strongly varying emission power as a function of frequency. In order to show that this variation does not hamper the reliability of a measurement, a transmission spectrum of a 10-cm-long gas cell filled with water-saturated air at atmospheric pressure is recorded, since it is expected to be slowly varying due to the strong pressure broadening of the water absorption lines. The absence of narrow peaks in the transmission spectrum may then prove that the structured emission spectrum does not prevent an accurate measurement. To demonstrate the superiority of the QCL as a spectrometer source, the results using the QCL and the thermal source are compared. Figure 6.3(b)

shows the transmission spectra for this configuration taken with both the QCL in G-TAWB operation and the thermal source. The transmission spectrum was obtained by dividing a spectrum taken with the gas cell positioned in the sample chamber of the spectrometer by a subsequently recorded spectrum without the cell. Figure 6.3(b) also shows a simulated spectrum obtained from the HITRAN database based on the *model tropics, USA,* at 296 K [125]. While the measurement employing the QCL as a source clearly shows the slowly varying transmission spectrum in agreement with the simulated spectrum, the emission power of the thermal source is too low for a meaningful measurement. Note that the peak due to an electrical pickup, which is marked by a hatched rectangle in Figs. 6.2(b) and 6.3(a), has shifted out of the investigated frequency range due to the different scanner speed. In order to confirm the validity of the obtained results, the measurements were repeated with a reduced noise level by decreasing the resolution from 0.3 to 1.5 GHz and the mirror speed from 7.5 to 2.2 kHz. Figure 6.3(c) shows the resulting transmission spectra. To investigate the reproducibility, both measurements with the QCL and with the thermal source were repeated. In contrast to the measurement at higher resolution, the spectra recorded using the thermal source now show reasonable results. However, the comparison of the nominally identical spectra and the presence of negative values between 4.73 and 4.74 THz reveal that the quickly varying modulation in the spectra of the thermal source is due to noise. In contrast, the transmission spectra using the QCL as a source are smooth and well reproducible despite the strongly varying power in the emission spectrum.

6.4 Tuning mechanism and investigation of additional quantum-cascade lasers

The G-TAWB operation relies on the strong current-induced tuning of a THz QCL. There are two established mechanisms in the literature, which may explain the strong tuning of our QCL. First, the frequency of the laser mode can be tuned by changing the waveguide/resonator temperature, by which the refractive index of the material is modified [126]. The temperature change can either be realized by directly changing the temperature of the cryostat cold finger or by changing the injection current of the QCL in continuous-wave or high-duty-cycle pulsed operation, through which the produced heat is altered [96, 127]. The temperature change is a relatively slow process, which occurs on time scales exceeding 10 µs [119]. The achievable tuning range is determined by the functional dependence of the material refractive index on temperature as well as by the temperature range over which the QCL operates. Since the improvement of these factors is difficult, the typical tuning range of THz QCLs based on single-plasmon waveguides is limited to several GHz.

A second tuning mechanism is the modification of the active-region refractive index by frequency pulling [108–110]. A different optical gain (or loss) always leads to a modification of the refractive index, since both values are coupled by the Kramers-Kronig relation. In contrast to the tuning by temperature, this is a very fast process as it is coupled to the gain build-up in the THz QCL. Therefore, this mechanism is compatible with the fast tuning at 300 kHz observed for the QCL in G-TAWB operation. Since the gain profile and its

dependence on the current can vary significantly even for similar heterostructure designs, the achievable tuning range is also expected to differ.

Figure 6.4 shows the spectral power of three additional QCLs in TAWB operation, which are similar in terms of their wavefunction structure, center frequency, and waveguide/resonator dimensions to the QCL considered so far in this work. Figure 6.4(a) displays the spectrum of a GaAs/AlAs QCL fabricated from wafer M4.3011, for which the miniband width has been increased and the coupling to the injection level improved compared to the GaAs/AlAs QCL discussed so far. For TAWB operation, the spectrum is narrower than for the GaAs/AlAs QCL shown in the inset of Fig. 6.2(a), but still exhibits an almost continuous coverage over a frequency range of 60 GHz with a narrow gap at 4.724 THz. Figures 6.4(b) and 6.4(c) display the spectra of two additional QCLs with $Al_{0.25}Ga_{0.75}As$ barriers fabricated from wafers M4.2591 and M4.2594, respectively, which are almost identical in their design with sample B2 in Ref. [7]. The QCLs exhibit a maximal tuning of the individual modes of 7.5 and 6.6 GHz, respectively, which does not span the mode spacing of about 10 GHz. While all QCLs exhibit a tuning range well above 5 GHz, only the QCLs based on AlAs barriers exhibit sufficient tuning in order to close the spectral gaps between the Fabry-Pérot modes. Apparently, the reduced leakage currents due to the higher barriers also have a significant impact on the current-dependent gain profile in addition to the improved wall-plug efficiency demonstrated in Ref. [31]. A more detailed investigation to identify the influence of the AlAs barriers for the increased tuning range is necessary to understand the difference between QCLs with AlAs and $Al_{0.25}Ga_{0.75}As$ barriers.

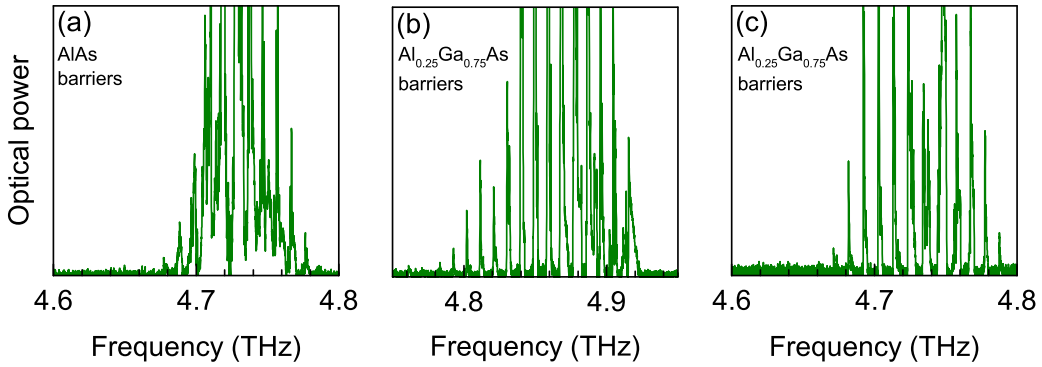

Figure 6.4: Spectral power of three additional THz QCLs in TAWB operation with (a) AlAs barriers such as the QCL considered so far as well as (b) and (c) $Al_{0.25}Ga_{0.75}As$ barriers. The QCLs in (a), (b), and (c) are fabricated from wafers M4.3011, M4.2591, and M4.2594, respectively.

6.5 Collection efficiency of the spectrometer

So far, it has been shown that the QCL is superior to the thermal source in terms of the SNR and the dynamic range due to its high output power. Since the QCL is positioned at the port for external sources, which is not specifically designed for QCLs, only a fraction of the radiation emitted by the QCL might be collected by the spectrometer and directed toward the detector. This fraction represents the collection efficiency of the spectrometer for the external spectrometer port when using the QCL as a source. A collection efficiency substantially lower than 1 may indicate that the intensity impinging on the detector can be further increased by an optimized optical coupling, which would lead to even higher values of the SNR and the dynamic range for a measurement using a THz QCL in G-TAWB operation. In contrast, the collection efficiency for the thermal source is already optimal, since it is integrated into the spectrometer to achieve the best possible optical coupling to the spectrometer optics. Therefore, only the collection efficiency for the QCL as a source is investigated in the following.

The first optical element—apart from the window of the spectrometer port for external sources—is an off-axis parabolic mirror. This mirror collimates radiation originating from its focal point and directs it toward the beam splitter of the interferometer. The collection efficiency of this mirror can be determined by comparing its area with the beam area of the QCL. The diameter of the mirror amounts to about 9 cm and its focal length to about 40 cm. The beam diameter of the radiation emitted from the QCL positioned in the focal point of the mirror amounts to 54 cm, as calculated from the divergence angle of 34° given in chapter 4. Calculating the ratio of the areas corresponding to the mirror and beam diameters yields a collection efficiency of about 3%. In this calculation, a uniform distribution of the QCL beam is implicitly assumed. For a more realistic calculation, the beam profile has to be taken into account, which can be performed with the models described in chapter 4. Such a calculation yields a collection efficiency of about 9%. The influence of modulations in the far-field distribution is negligible at the considered distance of 40 cm.

After the collimated beam has traveled through the interferometer, it is focused onto an aperture between the interferometer and the sample chamber. This aperture is sometimes called Jacquinot stop [83]. It blocks any radiation that was not sufficiently collimated by the collecting mirror. Without the aperture, the uncollimated part of the radiation would lead to a reduction in the achievable resolution. In fact, only an infinitely small source would lead to a perfectly collimated beam so that there is always a non-collimated part to be removed. Quantifying the power reduction due to the Jacquinot stop is difficult, since it depends on the specifics of the radiation field emitted by the QCL.

Losses due to absorption are expected to be small, since the spectrometer optics only consists of mirrors. The optical window at the spectrometer port for external sources is made from 1.7-mm thick high-density polyethylene and has a transmittance of about 87% at 4.7 THz. The spectrometer itself can be evacuated, and the optical path between the cryostat and the external port of the spectrometer can be purged with nitrogen to reduce or even completely avoid losses by water vapor in air.

Due to the limited size of the collecting mirror of the spectrometer, only about 10% of the total emitted power of the QCL is expected to be collected by the first mirror of the spectrometer. This problem might be compensated by, for instance, additional optics, which is expected to lead to a further increase of the SNR and dynamic range for measurements employing a QCL in G-TAWB operation.

6.6 Conclusions

By employing a THz QCL in G-TAWB operation as the source in a Fourier transform spectrometer, gapless high-resolution transmission spectra can be obtained. Due to the high emission powers of THz QCLs, they are superior to commonly used wideband sources for spectroscopy in terms of the signal-to-noise ratio and the dynamic range by a factor of 10 to 100. The prototypical transmission measurement presented in this chapter using a THz QCL in G-TAWB operation was performed over a spectral range of 72 GHz at a resolution of 0.3 GHz. The frequency coverage for such a spectroscopic measurement is more than a factor of 10 larger than what is typically demonstrated in the literature using THz QCLs in continuous-wave operation [7, 20, 92, 93, 95–97, 112]. However, the achieved resolution with THz QCLs in continuous-wave operation is usually in the MHz to kHz range and therefore considerably higher. For these reasons, spectroscopy using THz QCLs in G-TAWB operation is complementary to spectroscopic techniques employing THz QCLs in continuous-wave operation. While wideband spectroscopy at a resolution on the order of 0.1 GHz can be performed with QCLs in G-TAWB operation employed for Fourier transform spectroscopy, QCLs in continuous-wave operation can be used if a resolution in the MHz to kHz range is required for the spectroscopy of single absorption (or emission) lines.

An alternative approach for high-resolution wideband spectroscopy is dual-comb spectroscopy based on QCLs operated as frequency combs. Similar to the approach demonstrated here, the modes of these QCLs need to be tuned by at least the value of the mode spacing in order to obtain a spectrum without gaps. However, in contrast to the approach demonstrated here, the emission of the QCLs has to maintain frequency comb properties throughout the entire tuning range. Realizing such a QCL is extremely challenging due to important fundamental reasons. Since QCLs rely on waveguiding structures, waveguide dispersion in addition to material dispersion counteracts frequency comb operation, which must be compensated by an appropriate mechanism. While frequency comb operation can be obtained for specific values of the operating parameters, tuning the QCL via changing the effective refractive index will introduce additional dispersion that destroys frequency comb operation at some point. An alternative tuning mechanism would be an external cavity. However, sufficient continuous tuning of a multi-mode QCL by an external cavity has not been demonstrated so far. In addition, it is doubtful whether a sufficient stability of the external cavity can be achieved to obtain frequency comb operation. Consequently, dual comb spectroscopy based on THz QCLs has only been demonstrated with large spectral gaps of about 8 GHz [101]. In fact, only a frequency-multiplexed measurement employing dual comb spectroscopy was demonstrated so far, not at all utilizing the high spectral resolution that is in principle possible with that approach.

THz QCLs for G-TAWB operation can be optimized in several aspects. First, a QCL with an active region designed for a larger spectral range, which is known to be possible up to a bandwidth exceeding 1.7 THz [123], would clearly be very useful. For such a QCL with a larger gain bandwidth, the mode spacing is expected to remain rather constant if the waveguide and resonator geometry is unchanged, since the mode spacing depends only weakly on the waveguide dispersion. Thus, the required tuning range is almost independent of the gain bandwidth. However, in order to design future active regions for a tuning range exceeding the mode spacing on a regular basis, a better understanding of the mechanism responsible for the large current-induced tuning observed in some QCLs is necessary. To provide alternative or complementary approaches, fast tuning mechanisms compatible with QCLs with Fabry-Pérot resonators, such as for example the facet illumination with near-infrared light, should also be improved [119]. Since QCL-related noise was found to reduce the SNR, employing a highly stable voltage-to-current converter to provide the current ramps promises a higher sensitivity. With this kind of current source, the spectrum of a QCL in G-TAWB operation may also be smoothed. This may be achieved by modified pulse shapes such as a set of ramps with different slopes to compensate for low emission powers at small currents. Furthermore, a calculation of the collection efficiency of the first spectrometer mirror revealed that less than 10% of the radiation emitted by the QCL is coupled into the spectrometer. By improving the optical coupling of the QCL emission to the spectrometer for example via additional optics, a further increase in the SNR and dynamic range by a factor of about 10 might be feasible. In summary, QCLs in G-TAWB operation pave the way for high-sensitivity and high-resolution spectroscopy over a wide spectral range at THz frequencies.

7 Summary and outlook

This thesis presented the development of methods to tailor the emission characteristics of THz QCLs and employ them for spectroscopy with highest resolution and sensitivity. One focus of this work was placed on the far-field distribution of THz QCLs with single-plasmon waveguides, which was not thoroughly investigated in the literature so far, although single-plasmon waveguides are employed for most proof-of-principle demonstrations of QCL-enabled THz spectroscopy. The far-field distribution usually exhibits multiple lobes, which could be quantitatively reproduced by model calculations, and their origin thus unambiguously identified. Since these modulations are an impediment to most applications, it was demonstrated how to obtain a single-lobed far-field distribution.

A second focus of this thesis was placed on two complementary spectroscopic techniques. For the high-resolution spectroscopy of a single absorption or emission line, the narrow linewidths in the MHz to kHz range of THz QCLs operated in continuous-wave mode can be exploited. Manufacturing a QCL with an emission frequency precisely predefined by the experimental requirements was a long-standing problem for QCL-based high-resolution spectroscopy. This problem originated in part from the incomplete quantitative understanding of the relation between the emission frequencies and the waveguide and resonator parameters of THz QCLs. Therefore, these relations have been thoroughly investigated mainly via rigorous and approximate calculations. A particular result of these calculations is that the length of the resonator has to be controlled with a precision of at least 1 µm in order to control the emission frequency with a precision of at least 1 GHz. Since this precision cannot be achieved with conventional methods, a novel post-fabrication technique relying on a mechanical polishing of the QCL front facet has been developed, which allows for the required control of the emission frequency, thus solving this long-standing problem for QCL-based high-resolution spectroscopy.

While the high-resolution spectroscopy of a particular absorption line of a single atomic or molecular species only requires a continuous (i.e. without spectral gaps) emission bandwidth of a few GHz, a significantly larger bandwidth is necessary for more experimental flexibility. For this purpose, high-resolution THz Fourier transform spectrometers are often used, which allow for wideband absorption spectroscopy at a maximal resolution of typically 100 MHz. However, THz spectra obtained with Fourier transform spectrometers suffer from the low sensitivity due to the very low spectral brightness of the available wideband sources for the THz region. In an effort to utilize the high spectral brightness of QCLs for THz Fourier transform spectroscopy, a novel principle referred to as gapless time-averaged wideband (G-TAWB) operation has been developed in the framework of this thesis. This novel principle relies on a multi-mode THz QCL whose modes can be rapidly tuned via a ramping of the driving current. The application of such a QCL for THz Fourier transform

spectroscopy resulted in a substantially increased signal-to-noise ratio and dynamic range by a factor of 10 to 100 as compared to conventional wideband sources.

The so-far obtained continuous spectral coverage of 72 GHz for G-TAWB operation is mainly determined by the limited emission bandwidth of the employed QCL. While QCLs with a significantly larger emission bandwidth even exceeding 1 THz have already been demonstrated [123], the main challenge is to simultaneously achieve a sufficient dynamical tuning range. In order to meet that challenge, a deeper understanding of the mechanisms responsible for the employed current-induced tuning is required.

To sum up, one focus of this thesis was laid on the far-field distribution of THz QCLs with single-plasmon waveguides and how to obtain a distribution suitable for most spectroscopic applications. A second focus was laid on two complementary spectroscopic techniques. While a very high resolution in the MHz to kHz range can be obtained by employing THz QCLs in continuous-wave operation, a substantially larger spectral coverage—yet with a maximal resolution of typically 100 MHz—can be obtained by using a suitable current-ramped THz QCL as a source for a Fourier transform spectrometer.

One of the main challenges for flexible THz spectroscopy based on QCLs remains the realization of a technique to routinely obtain a large tuning range, which does not significantly compromise the output power. In addition, such a tuning method should be highly reliable and compatible with frequency stabilization techniques. Although numerous methods to obtain a large tuning range for THz QCLs have been demonstrated, no one of them fulfills all the listed criteria at the same time. Furthermore, larger average output powers are desirable to further increase the sensitivity of spectrometers using THz QCL sources. So far, the average output power is mainly limited by the large amount of excess heat that the cooling system has to dissipate while maintaining cryogenic temperatures. Therefore, a second important challenge is to understand the origin of the extremely low power conversion efficiencies observed for THz QCLs, which is typically around 0.1% even at very low temperatures. This value cannot be solely explained by the non-radiative scattering mechanisms required to obtain population inversion, since power conversion efficiencies well above 10% are theoretically possible with the current active-region designs. Although the techniques presented in this thesis will already enable powerful QCL-based high-resolution THz spectroscopy in the near future, the development of robust techniques to further increase the tuning range and the realization of a substantially higher power conversion efficiency may be regarded as the main challenges for an even more widespread application of THz QCLs in science and industry.

Appendix: Nominal layer sequences

All samples investigated in this work were grown by molecular beam epitaxy at a substrate temperature of 600 °C on a semi-insulating GaAs substrate with a (001) orientation. Table 7.1 shows the nominal layer sequences of the active regions of the employed wafers. The bold numbers refer to the barriers made of $Al_xGa_{1-x}As$ with the Al content x given in the table. The plain numbers refer to the Al-free GaAs wells, and the underlined numbers indicate the wells that are doped with silicon using a doping density of n_{dop} as specified in the table. The last number of each sequence refers to the layer closest to the substrate. Each growth was started with a GaAs buffer layer of a thickness of 300 nm in case of the wafers M4.2135, M4.2591, and M4.2594 or with a buffer layer of a thickness of 200 nm in case of the wafers M4.2650, M4.2949, and M4.3011. As an etch stop layer for the fabrication of metal-metal waveguides and as a high-reflectivity layer for the optical monitoring during the growth, an $Al_yGa_{1-y}As$ layer with a thickness t_r and an Al content y as indicated in Tab. 7.1 was grown on top of the buffer layer. For the bottom contact, a GaAs:Si layer with a doping density of 2×10^{18} cm^{-3} and a thickness of 700 nm was deposited. After the growth of the layer sequence of the active region, an additional barrier that is identical to the last barrier in each layer sequence as indicated in Tab. 7.1 was deposited for all wafers

Table 7.1: Wafer number, number of repetitions N_L of the nominal layer sequence, nominal layer sequence of the active region, Al content x in the barriers, doping density n_{dop} of the quantum wells, thickness t_r of the $Al_yGa_{1-y}As$ layer for the optical monitoring, and its Al content y.

Wafer No.	N_L	Nominal layer sequence	x	n_{dop} (10^{16} cm^{-3})	t_r (nm), y
M4.2135	90	**3.7**/15.8/**0.69**/10.1/**0.69**/17.7/**1.8**/14.3/**2.1**/ 13.6/**2.2**/<u>13.4</u>/**2.2**/<u>12.8</u>/**2.9**/12.8/**4**/11.3	0.15	1.1	–
M4.2591	88	24.9/**1.9**/16.3/**0.9**/10.1/**1.3**/9.2/**1.8**/ 7.6/**2.1**/6.9/2.1/<u>16.9</u>/**3.8**/15.2/**3.3**	0.25	8	74, 0.95
M4.2594	88	25.4/**1.9**/16.3/**0.9**/10.1/**1.3**/9.2/**1.8**/ 7.6/**2.1**/6.9/2.1/<u>16.9</u>/**3.8**/15.2/**3.3**	0.25	8	74, 0.95
M4.2650	85	9.7/**0.5**/15.5/**1.0**/12.4/**1.9**/11.3/**2.9**/ 9.1/**2.9**/8.2/**2.9**/6.8/**2.9**/<u>16.3</u>/**2.9**/13.9/**3.8**	0.18	2.7	110, 0.9
M4.2949	88	27.4/**0.56**/15.4/**0.56**/11.8/**0.56**/10.8/**0.56**/ 9.7/**0.56**/8.4/**0.56**/<u>18.2</u>/**1.12**/15.5/**1.12**	1	20	110, 0.9
M4.3011	88	27.2/**0.56**/15.0/**0.42**/12.1/**0.42**/10.8/**0.42**/ 9.2/**0.42**/8.1/**0.28**/2.0/**0.28**/<u>17.7</u>/**1.12**/15.7/**1.12**	1	20	110, 0.9

except for the wafer M4.2135. As the last growth step, a GaAs:Si layer with a thickness of 80 nm and a doping density of 5×10^{18} cm^{-3} was deposited for the top contact.

Bibliography

[1] J. Faist, F. Capasso, D. L. Sivco, C. Sirtori, A. L. Hutchinson, and A. Y. Cho, *Quantum cascade laser*, Science **264**, 553–556 (1994).

[2] R. Köhler, A. Tredicucci, F. Beltram, H. E. Beere, E. H. Linfield, A. G. Davies, D. A. Ritchie, R. C. Iotti, and F. Rossi, *Terahertz semiconductor-heterostructure laser*, Nature **417**, 156–159 (2002).

[3] S. Fathololoumi, E. Dupont, C. Chan, Z. Wasilewski, S. Laframboise, D. Ban, A. Mátyás, C. Jirauschek, Q. Hu, and H. C. Liu, *Terahertz quantum cascade lasers operating up to ∼200 K with optimized oscillator strength and improved injection tunneling*, Opt. Express **20**, 3866–3876 (2012).

[4] M. Wienold, B. Röben, L. Schrottke, R. Sharma, A. Tahraoui, K. Biermann, and H. T. Grahn, *High-temperature, continuous-wave operation of terahertz quantum-cascade lasers with metal-metal waveguides and third-order distributed feedback*, Opt. Express **22**, 3334–3348 (2014).

[5] E. Bründermann, H.-W. Hübers, and M. F. Kimmitt, *Terahertz techniques* (Springer, 2012).

[6] L. Ho, M. Pepper, and P. Taday, *Terahertz spectroscopy: Signatures and fingerprints*, Nat. Photon. **2**, 541–543 (2008).

[7] L. Schrottke, M. Wienold, R. Sharma, X. Lü, K. Biermann, R. Hey, A. Tahraoui, H. Richter, H.-W. Hübers, and H. T. Grahn, *Quantum-cascade lasers as local oscillators for heterodyne spectrometers in the spectral range around 4.745 THz*, Semicond. Sci. Technol. **28**, 035011, 5 pages (2013).

[8] L. Rezac, P. Hartogh, R. Güsten, H. Wiesemeyer, H.-W. Hübers, C. Jarchow, H. Richter, B. Klein, and N. Honingh, *First detection of the 63 μm atomic oxygen line in the thermosphere of mars with GREAT/SOFIA*, Astron. Astrophys. **580**, L10, 5 pages (2015).

[9] E. Bründermann, M. Havenith, G. Scalari, M. Giovannini, J. Faist, J. Kunsch, L. Mechold, and M. Abraham, *Turn-key compact high temperature terahertz quantum cascade lasers*, Opt. Express **14**, 1829–1841 (2006).

[10] P. Mousavi, F. Haran, D. Jez, F. Santosa, and J. S. Dodge, *Simultaneous composition and thickness measurement of paper using terahertz time-domain spectroscopy*, Appl. Opt. **48**, 6541–6546 (2009).

[11] A. J. Huber, F. Keilmann, J. Wittborn, J. Aizpurua, and R. Hillenbrand, *Terahertz near-field nanoscopy of mobile carriers in single semiconductor nanodevices*, Nano Lett. **8**, 3766–3770 (2008).

[12] J.-S. Rieh, B. Jagannathan, D. R. Greenberg, M. Meghelli, A. Rylyakov, F. Guarin, Z. Yang, D. C. Ahlgren, G. Freeman, P. Cottrell, and D. Harame, *SiGe heterojunction bipolar transistors and circuits toward terahertz communication applications*, IEEE Trans. Microw. Theory Tech. **52**, 2390–2408 (2004).

[13] J. Blau, K. Cohn, W. B. Colson, and R. Vigil, *Free electron lasers in 2013*, Proc. FEL **2013**, 486–490 (2013).

[14] http://www.toptica.com/products/terahertz-systems/time-domain/teraflash/, accessed on 12 February 2018.

[15] https://www.bruker.com/de/products/infrared-near-infrared-and-raman-spectroscopy/ft-ir-research-spectrometers/ifs-125hr/overview.html, accessed on 12 February 2018.

[16] http://www.toptica.com/products/terahertz-systems/frequency-domain/terabeam/, accessed on 12 February 2018.

[17] L. Consolino, S. Jung, A. Campa, M. De Regis, S. Pal, J. H. Kim, K. Fujita, A. Ito, M. Hitaka, S. Bartalini, M. A. Belkin, and M. S. Vitiello, *Spectral purity and tunability of terahertz quantum cascade laser sources based on intracavity difference-frequency generation*, Sci. Adv. **3**, e1603317, 9 pages (2017).

[18] M. Yamanishi, T. Edamura, K. Fujita, N. Akikusa, and H. Kan, *Theory of the intrinsic linewidth of quantum-cascade lasers: Hidden reason for the narrow linewidth and line-broadening by thermal photons*, IEEE J. Quantum Electron. **44**, 12–29 (2008).

[19] A. A. Danylov, T. M. Goyette, J. Waldman, M. J. Coulombe, A. J. Gatesman, R. H. Giles, W. D. Goodhue, X. Qian, and W. E. Nixon, *Frequency stabilization of a single mode terahertz quantum cascade laser to the kilohertz level*, Opt. Express **17**, 7525–7532 (2009).

[20] H.-W. Hübers, S. G. Pavlov, A. D. Semenov, R. Köhler, L. Mahler, A. Tredicucci, H. E. Beere, D. A. Ritchie, and E. H. Linfield, *Terahertz quantum cascade laser as local oscillator in a heterodyne receiver*, Opt. Express **13**, 5890–5896 (2005).

[21] H. Richter, S. G. Pavlov, A. D. Semenov, L. Mahler, A. Tredicucci, H. E. Beere, D. A. Ritchie, and H.-W. Hübers, *Submegahertz frequency stabilization of a terahertz quantum cascade laser to a molecular absorption line*, Appl. Phys. Lett. **96**, 071112, 3 pages (2010).

[22] M. S. Vitiello, L. Consolino, S. Bartalini, A. Taschin, A. Tredicucci, M. Inguscio, and P. De Natale, *Quantum-limited frequency fluctuations in a terahertz laser*, Nat. Photon. **6**, 525–528 (2012).

[23] G. Denisov, A. Fokin, M. Y. Glyavin, G. Y. Golubiatnikov, L. Lubyako, M. Morozkin, B. Movschevich, and A. Tsvetkov, *High precision frequency stabilization of a 263 GHz continuous wave gyrotron*, EPJ Web of Conferences **149**, 04022, 1 page (2017).

[24] S. S. Dhillon, M. S. Vitiello, E. H. Linfield, A. G. Davies, M. C. Hoffmann, J. Booske, C. Paoloni, M. Gensch, P. Weightman, G. P. Williams, E. Castro-Camus, D. R. S. Cumming, F. Simoens, I. Escorcia-Carranza, J. Grant, S. Lucyszyn, M. Kuwata-Gonokami, K. Konishi, M. Koch, C. A. Schmuttenmaer, T. L. Cocker, R. Huber, A. G. Markelz, Z. D. Taylor, V. P. Wallace, J. A. Zeitler, J. Sibik, T. M. Korter, B. Ellison, S. Rea, P. Goldsmith, K. B. Cooper, R. Appleby, D. Pardo, P. G. Huggard, V. Krozer, H. Shams, M. Fice, C. Renaud, A. Seeds, A. Stöhr, M. Naftaly, N. Ridler, R. Clarke, J. E. Cunningham, and M. B. Johnston, *The 2017 terahertz science and technology roadmap*, J. Phys. D **50**, 043001, 49 pages (2017).

[25] R. F. Kazarinov and R. A. Suris, *Possibility of the amplification of electromagnetic waves in a semiconductor with a superlattice*, Sov. Phys.: Semicond. **5**, 707–709 (1971).

[26] L. Esaki and R. Tsu, *Superlattice and negative differential conductivity in semiconductors*, IBM J. Res. Dev. **14**, 61–65 (1970).

[27] J. Faist, F. Capasso, C. Sirtori, D. L. Sivco, A. L. Hutchinson, and A. Y. Cho, *Room temperature mid-infrared quantum cascade lasers*, Electron. Lett. **32**, 560–561 (1996).

[28] Y. Bai, N. Bandyopadhyay, S. Tsao, S. Slivken, and M. Razeghi, *Room temperature quantum cascade lasers with 27% wall plug efficiency*, Appl. Phys. Lett. **98**, 181102, 3 pages (2011).

[29] O. Cathabard, R. Teissier, J. Devenson, J. Moreno, and A. Baranov, *Quantum cascade lasers emitting near 2.6 μm*, Appl. Phys. Lett. **96**, 141110, 3 pages (2010).

[30] B. S. Williams, *Terahertz quantum-cascade lasers*, Nat. Photon. **1**, 517–525 (2007).

[31] L. Schrottke, X. Lü, G. Rozas, K. Biermann, and H. T. Grahn, *Terahertz GaAs/AlAs quantum-cascade lasers*, Appl. Phys. Lett. **108**, 102102, 5 pages (2016).

[32] K. S. Thygesen and A. Rubio, *Conserving* GW *scheme for nonequilibrium quantum transport in molecular contacts*, Phys. Rev. B **77**, 115333, 22 pages (2008).

[33] J. Schulman and Y.-C. Chang, *New method for calculating electronic properties of superlattices using complex band structures*, Phys. Rev. B **24**, 4445, 4 pages (1981).

[34] M. Jaros and K. Wong, *New electron states in GaAs-$Ga_xAl_{1-x}As$ superlattice*, J. Phys. C **17**, L765–L769 (1984).

[35] M. Jaros, K. Wong, and M. Gell, *Electronic structure of GaAs-$Ga_{1-x}Al_xAs$ quantum well and sawtooth superlattices*, Phys. Rev. B **31**, 1205, 3 pages (1985).

[36] G. Bastard, *Wave mechanics applied to semiconductor heterostructures* (Wiley, 1990).

[37] E. Luna, F. Ishikawa, P. D. Batista, and A. Trampert, *Indium distribution at the interfaces of (Ga,In)(N,As)/GaAs quantum wells*, Appl. Phys. Lett. **92**, 141913, 3 pages (2008).

[38] E. Luna, B. Satpati, J. B. Rodriguez, A. N. Baranov, E. Tournie, and A. Trampert, *Interfacial intermixing in InAs/GaSb short-period-superlattices grown by molecular beam epitaxy*, Appl. Phys. Lett. **96**, 021904, 3 pages (2010).

[39] X. Lü, L. Schrottke, E. Luna, and H. T. Grahn, *Efficient simulation of the impact of interface grading on the optical and transport properties of semiconductor heterostructures*, Appl. Phys. Lett. **104**, 232106, 5 pages (2014).

[40] G. Scalari, L. Ajili, J. Faist, H. Beere, E. Linfield, D. Ritchie, and G. Davies, *Far-infrared ($\lambda = 87$ μm) bound-to-continuum quantum-cascade lasers operating up to 90 K*, Appl. Phys. Lett. **82**, 003165, 3 pages (2003).

[41] B. S. Williams, S. Kumar, H. Callebaut, Q. Hu, and J. L. Reno, *Terahertz quantum-cascade laser at $\lambda \approx 100$ μm using metal waveguide for mode confinement*, Appl. Phys. Lett. **83**, 2124, 3 pages (2003).

[42] M. Wienold, L. Schrottke, M. Giehler, R. Hey, W. Anders, and H. T. Grahn, *Low-voltage terahertz quantum-cascade lasers based on LO-phonon-assisted interminiband transitions*, Electron. Lett. **45**, 1030, 2 pages (2009).

[43] M. Wienold, L. Schrottke, M. Giehler, R. Hey, and H. T. Grahn, *Nonlinear transport in quantum-cascade lasers: The role of electric-field domain formation for the laser characteristics*, J. Appl. Phys. **109**, 073112, 6 pages (2011).

[44] M. Wienold, B. Röben, X. Lü, G. Rozas, L. Schrottke, K. Biermann, and H. T. Grahn, *Frequency dependence of the maximum operating temperature for quantum-cascade lasers up to 5.4 THz*, Appl. Phys. Lett. **107**, 202101, 4 pages (2015).

[45] A. Wacker, *Gain in quantum cascade lasers and superlattices: A quantum transport theory*, Phys. Rev. B **66**, 085326, 7 pages (2002).

[46] S.-C. Lee and A. Wacker, *Nonequilibrium Green's function theory for transport and gain properties of quantum cascade structures*, Phys. Rev. B **66**, 245314, 18 pages (2002).

[47] T. Kubis, C. Yeh, P. Vogl, A. Benz, G. Fasching, and C. Deutsch, *Theory of nonequilibrium quantum transport and energy dissipation in terahertz quantum cascade lasers*, Phys. Rev. B **79**, 195323, 10 pages (2009).

[48] R. C. Iotti and F. Rossi, *Nature of charge transport in quantum-cascade lasers*, Phys. Rev. Lett. **87**, 146603, 4 pages (2001).

[49] C. Weber, A. Wacker, and A. Knorr, *Density-matrix theory of the optical dynamics and transport in quantum cascade structures: The role of coherence*, Phys. Rev. B **79**, 165322, 14 pages (2009).

[50] R. C. Iotti and F. Rossi, *Microscopic theory of semiconductor-based optoelectronic devices*, Rep. Prog. Phys. **68**, 2533, 39 pages (2005).

[51] D. Taj, R. C. Iotti, and F. Rossi, *Microscopic modeling of energy relaxation and decoherence in quantum optoelectronic devices at the nanoscale*, Eur. Phys. J. B **72**, 305–322, 10 pages (2009).

[52] L. Schrottke, M. Giehler, M. Wienold, R. Hey, and H. T. Grahn, *Compact model for the efficient simulation of the optical gain and transport properties in THz quantum-cascade lasers*, Semicond. Sci. Technol. **25**, 045025, 10 pages (2010).

[53] X. Lü, L. Schrottke, and H. T. Grahn, *Fourier-transform-based model for carrier transport in semiconductor heterostructures: Longitudinal optical phonon scattering*, J. Appl. Phys. **119**, 214302, 14 pages (2016).

[54] C. Jacoboni and P. Lugli, *The Monte Carlo method for semiconductor device simulation* (Springer, 2012).

[55] L. Schrottke, X. Lü, and H. T. Grahn, *Fourier transform-based scattering-rate method for self-consistent simulations of carrier transport in semiconductor heterostructures*, J. Appl. Phys. **117**, 154309, 8 pages (2015).

[56] C. Y. Wang, L. Diehl, A. Gordon, C. Jirauschek, F. X. Kärtner, A. Belyanin, D. Bour, S. Corzine, G. Höfler, M. Troccoli, J. Faist, and F. Capasso, *Coherent instabilities in a semiconductor laser with fast gain recovery*, Phys. Rev. A **75**, 031802, 4 pages (2007).

[57] C. Jirauschek and T. Kubis, *Modeling techniques for quantum cascade lasers*, Appl. Phys. Rev. **1**, 011307, 51 pages (2014).

[58] E. O. Kane, *Band structure of indium antimonide*, J. Phys. Chem. Sol. **1**, 249–261 (1957).

[59] X. Lü, L. Schrottke, and H. T. Grahn, *Efficient numerical procedure for the determination of the wave function-independent terms in longitudinal optical phonon scattering rates formulated in the Fourier domain*, J. Comput. Electron. **15**, 1505–1510 (2016).

[60] X. Lü, L. Schrottke, E. Luna, and H. T. Grahn, *Efficient simulation of the impact of interface grading on the optical and transport properties of semiconductor heterostructures*, Appl. Phys. Lett. **104**, 232106, 5 pages (2014).

[61] J. A. Fan, M. A. Belkin, F. Capasso, S. P. Khanna, M. Lachab, A. G. Davies, and E. H. Linfield, *Wide-ridge metal-metal terahertz quantum cascade lasers with high-order lateral mode suppression*, Appl. Phys. Lett. **92**, 031106, 3 pages (2008).

[62] D. Bachmann, M. Rösch, M. J. Süess, M. Beck, K. Unterrainer, J. Darmo, J. Faist, and G. Scalari, *Short pulse generation and mode control of broadband terahertz quantum cascade lasers*, Optica **3**, 1087–1094 (2016).

[63] M. Wienold, A. Tahraoui, L. Schrottke, R. Sharma, X. Lü, K. Biermann, R. Hey, and H. T. Grahn, *Lateral distributed-feedback gratings for single-mode, high-power terahertz quantum-cascade lasers*, Opt. Express **20**, 11207–11217 (2012).

[64] I. Kundu, P. Dean, A. Valavanis, L. Chen, L. Li, J. E. Cunningham, E. H. Linfield, and A. G. Davies, *Discrete Vernier tuning in terahertz quantum cascade lasers using coupled cavities*, Opt. Express **22**, 16595–16605 (2014).

[65] M. Hempel, B. Röben, M. Niehle, L. Schrottke, A. Trampert, and H. T. Grahn, *Continuous tuning of two-section, single-mode terahertz quantum-cascade lasers by fiber-coupled, near-infrared illumination*, AIP Adv. **7**, 055201 (2017).

[66] L. Mahler, A. Tredicucci, F. Beltram, C. Walther, J. Faist, H. E. Beere, D. A. Ritchie, and D. S. Wiersma, *Quasi-periodic distributed feedback laser*, Nat. Photon. **4**, 165, 5 pages (2010).

[67] G. Xu, R. Colombelli, S. P. Khanna, A. Belarouci, X. Letartre, L. Li, E. H. Linfield, A. G. Davies, H. E. Beere, and D. A. Ritchie, *Efficient power extraction in surface-emitting semiconductor lasers using graded photonic heterostructures*, Nat. Commun. **3**, 952, 7 pages (2012).

[68] Y. Chassagneux, J. Palomo, R. Colombelli, S. Dhillon, C. Sirtori, H. Beere, J. Alton, and D. Ritchie, *Terahertz microcavity lasers with subwavelength mode volumes and thresholds in the milliampere range*, Appl. Phys. Lett. **90**, 091113, 3 pages (2007).

[69] E. Mujagić, C. Deutsch, H. Detz, P. Klang, M. Nobile, A. M. Andrews, W. Schrenk, K. Unterrainer, and G. Strasser, *Vertically emitting terahertz quantum cascade ring lasers*, Appl. Phys. Lett. **95**, 011120, 3 pages (2009).

[70] L. Mahler, M. I. Amanti, C. Walther, A. Tredicucci, F. Beltram, J. Faist, H. E. Beere, and D. A. Ritchie, *Distributed feedback ring resonators for vertically emitting terahertz quantum cascade lasers*, Opt. Express **17**, 13031–13039 (2009).

[71] S. Kohen, B. S. Williams, and Q. Hu, *Electromagnetic modeling of terahertz quantum cascade laser waveguides and resonators*, J. Appl. Phys. **97**, 053106, 9 pages (2005).

[72] M. Brandstetter, M. Krall, C. Deutsch, H. Detz, A. M. Andrews, W. Schrenk, G. Strasser, and K. Unterrainer, *Influence of the facet type on the performance of terahertz quantum cascade lasers with double-metal waveguides*, Appl. Phys. Lett. **102**, 231121, 4 pages (2013).

[73] B. S. Williams, S. Kumar, H. Callebaut, Q. Hu, and J. L. Reno, *Terahertz quantum-cascade laser operating up to 137 K*, Appl. Phys. Lett. **83**, 005142, 3 pages (2003).

[74] S. Kumar, B. S. Williams, S. Kohen, Q. Hu, and J. L. Reno, *Continuous-wave operation of terahertz quantum-cascade lasers above liquid-nitrogen temperature*, Appl. Phys. Lett. **84**, 002494, 3 pages (2004).

[75] B. S. Williams, S. Kumar, Q. Hu, and J. L. Reno, *Operation of terahertz quantum-cascade lasers at 164 K in pulsed mode and at 117 K in continuous-wave mode*, Opt. Express **13**, 3331–3339 (2005).

[76] M. A. Belkin, J. A. Fan, S. Hormoz, F. Capasso, S. P. Khanna, M. Lachab, A. G. Davies, and E. H. Linfield, *Terahertz quantum cascade lasers with copper metal-metal waveguides operating up to 178 K*, Opt. Express **16**, 3242–3248 (2008).

[77] S. Kumar, Q. Hu, and J. L. Reno, *186 K operation of terahertz quantum-cascade lasers based on a diagonal design*, Appl. Phys. Lett. **94**, 131105, 3 pages (2009).

[78] R. Eichholz, H. Richter, M. Wienold, L. Schrottke, R. Hey, H. T. Grahn, and H.-W. Hübers, *Frequency modulation spectroscopy with a THz quantum-cascade laser*, Opt. Express **21**, 32199–32206 (2013).

[79] T. Hagelschuer, M. Wienold, H. Richter, L. Schrottke, H. T. Grahn, and H.-W. Hübers, *Real-time gas sensing based on optical feedback in a terahertz quantum-cascade laser*, Opt. Express **25**, 30203–30213 (2017).

[80] M. Fischer, G. Scalari, C. Walther, and J. Faist, *Terahertz quantum cascade lasers based on* $In_{0.53}Ga_{0.47}As/In_{0.52}Al_{0.48}As/InP$, J. Cryst. Growth **311**, 1939–1943 (2009).

[81] A. W. Jackson, P. R. Pinsukanjana, A. C. Gossard, and L. A. Coldren, *In situ monitoring and control for MBE growth of optoelectronic devices*, IEEE J. Sel. Top. Quantum Electron. **3**, 836–844 (1997).

[82] A. Steiger, R. Müller, A. R. Oliva, Y. Deng, Q. Sun, M. White, and J. Lehman, *Terahertz laser power measurement comparison*, IEEE Trans. THz Sci. Technol. **6**, 664–669 (2016).

[83] P. R. Griffiths and J. A. de Haseth, *Fourier transform infrared spectrometry* (Wiley, 2007), 2nd ed.

[84] A. J. L. Adam, I. Kašalynas, J. N. Hovenier, T. O. Klaassen, J. R. Gao, E. E. Orlova, B. S. Williams, S. Kumar, Q. Hu, and J. L. Reno, *Beam patterns of terahertz quantum cascade lasers with subwavelength cavity dimensions*, Appl. Phys. Lett. **88**, 151105, 3 pages (2006).

[85] E. E. Orlova, J. N. Hovenier, T. O. Klaassen, I. Kašalynas, A. J. L. Adam, J. R. Gao, T. Klapwijk, B. S. Williams, S. Kumar, Q. Hu, and J. L. Reno, *Antenna model for wire lasers*, Phys. Rev. Lett. **96**, 173904, 4 pages (2006).

[86] M. Salih, P. Dean, A. Valavanis, S. P. Khanna, L. H. Li, J. E. Cunningham, A. G. Davies, and E. H. Linfield, *Terahertz quantum cascade lasers with thin resonant-phonon depopulation active regions and surface-plasmon waveguides*, J. Appl. Phys. **113**, 113110, 5 pages (2013).

[87] E. Bründermann, M. Havenith, G. Scalari, M. Giovannini, J. Faist, J. Kunsch, L. Mechold, and M. Abraham, *Turn-key compact high temperature terahertz quantum cascade lasers: Imaging and room temperature detection*, Opt. Express **14**, 1829–1841 (2006).

[88] H. Richter, N. Rothbart, and H.-W. Hübers, *Characterizing the beam properties of terahertz quantum-cascade lasers*, J. Infrared Millim. THz Waves **35**, 686–698 (2014).

[89] B. E. A. Saleh and M. C. Teich, *Fundamentals of photonics* (Wiley, 2007), 2nd ed.

[90] S. Barbieri, J. Alton, H. E. Beere, J. Fowler, E. H. Linfield, and D. A. Ritchie, *2.9 THz quantum cascade lasers operating up to 70 K in continuous wave*, Appl. Phys. Lett. **85**, 001674, 3 pages (2004).

[91] M. Giehler, H. Kostial, R. Hey, and H. T. Grahn, *Suppression of longitudinal modes in two-sectioned, coupled-cavity GaAs /(Al,Ga)As terahertz quantum-cascade lasers*, Appl. Phys. Lett. **91**, 161102, 3 pages (2007).

[92] H.-W. Hübers, S. G. Pavlov, H. Richter, A. D. Semenov, L. Mahler, A. Tredicucci, H. E. Beere, and D. A. Ritchie, *High-resolution gas phase spectroscopy with a distributed feedback terahertz quantum cascade laser*, Appl. Phys. Lett. **89**, 061115, 3 pages (2006).

[93] Y. Ren, J. N. Hovenier, R. Higgins, J. R. Gao, T. M. Klapwijk, S. C. Shi, A. Bell, B. Klein, B. S. Williams, S. Kumar, Q. Hu, and J. L. Reno, *Terahertz heterodyne spectrometer using a quantum cascade laser*, Appl. Phys. Lett. **97**, 161105, 3 pages (2010).

[94] R. Eichholz, H. Richter, S. G. Pavlov, M. Wienold, L. Schrottke, R. Hey, H. T. Grahn, and H.-W. Hübers, *Multi-channel terahertz grating spectrometer with quantum-cascade laser and microbolometer array*, Appl. Phys. Lett. **99**, 141112, 3 pages (2011).

[95] L. Consolino, S. Bartalini, H. E. Beere, D. A. Ritchie, M. S. Vitiello, and P. De Natale, *THz QCL-based cryogen-free spectrometer for in situ trace gas sensing*, Sensors **13**, 3331–3340 (2013).

[96] H.-W. Hübers, R. Eichholz, S. G. Pavlov, and H. Richter, *High resolution terahertz spectroscopy with quantum cascade lasers*, J. Infrared Millim. THz Waves **34**, 325–341 (2013).

[97] T. Hagelschuer, N. Rothbart, H. Richter, M. Wienold, L. Schrottke, H. T. Grahn, and H.-W. Hübers, *High-spectral-resolution terahertz imaging with a quantum-cascade laser*, Opt. Express **24**, 13839–13849 (2016).

[98] T. Hagelschuer, M. Wienold, H. Richter, L. Schrottke, K. Biermann, H. T. Grahn, and H.-W. Hübers, *Terahertz gas spectroscopy through self-mixing in a quantum-cascade laser*, Appl. Phys. Lett. **109**, 191101, 4 pages (2016).

[99] M. Wienold, B. Röben, L. Schrottke, and H. T. Grahn, *Evidence for frequency comb emission from a Fabry-Pérot terahertz quantum-cascade laser*, Opt. Express **22**, 30410–30424 (2014).

[100] M. Wienold, B. Röben, L. Schrottke, and H. T. Grahn, *Frequency comb operation of long-cavity terahertz quantum-cascade lasers*, Proc. SPIE **9767**, 97671A, 9 pages (2016).

[101] Y. Yang, D. Burghoff, D. J. Hayton, J.-R. Gao, J. L. Reno, and Q. Hu, *Terahertz multiheterodyne spectroscopy using laser frequency combs*, Optica **3**, 499, 4 pages (2016).

[102] J. J. Degnan, *The waveguide laser: A review*, Appl. Phys. A **11**, 1–33 (1976).

[103] M. Wienold, *Development of terahertz quantum-cascade lasers as sources for heterodyne receivers*, Dissertation, Humboldt-Universität (21.03.2012).

[104] M. Wienold, B. Röben, L. Schrottke, and H. T. Grahn, *Evidence for frequency comb emission from a Fabry-Pérot terahertz quantum-cascade laser*, Opt. Express **22**, 30410–30424 (2014).

[105] E. D. Palik, ed., *Handbook of Optical Constants of Solids* (Academic Press, 1985).

[106] E. D. Palik, ed., *Handbook of Optical Constants of Solids II* (Academic Press, 1995).

[107] M. S. M. Levinshtein, S. Rumyantsev, ed., *Handbook series on semiconductor parameters*, vol. 1 (World Scientific, 1996).

[108] A. Yariv, *Quantum Electronics* (Wiley, 1988), 3rd ed.

[109] L. A. Dunbar, R. Houdré, G. Scalari, L. Sirigu, M. Giovannini, and J. Faist, *Small optical volume terahertz emitting microdisk quantum cascade lasers*, Appl. Phys. Lett. **90**, 141114, 3 pages (2007).

[110] H. Zhang, G. Scalari, J. Faist, L. A. Dunbar, and R. Houdré, *Design and fabrication technology for high performance electrical pumped terahertz photonic crystal band edge lasers with complete photonic band gap*, J. Appl. Phys. **108**, 093104, 6 pages (2010).

[111] J. Faist, *Quantum cascade lasers* (Oxford University Press, 2013).

[112] H. Richter, M. Wienold, L. Schrottke, K. Biermann, H. T. Grahn, and H.-W. Hübers, *4.7-THz Local Oscillator for the GREAT Heterodyne Spectrometer on SOFIA*, IEEE Trans. THz Sci. Technol. **5**, 539–545 (2015).

[113] M. S. Vitiello and A. Tredicucci, *Tunable emission in THz quantum cascade lasers*, IEEE Trans. Terahertz Sci. Technol. **1**, 76–84 (2011).

[114] D. Turčinková, M. I. Amanti, F. Castellano, M. Beck, and J. Faist, *Continuous tuning of terahertz distributed feedback quantum cascade laser by gas condensation and dielectric deposition*, Appl. Phys. Lett. **102**, 181113, 4 pages (2013).

[115] K. Ohtani, M. Beck, and J. Faist, *Electrical laser frequency tuning by three terminal terahertz quantum cascade lasers*, Appl. Phys. Lett. **104**, 011107, 5 pages (2014).

[116] N. Han, A. de Geofroy, D. P. Burghoff, C. W. I. Chan, A. W. M. Lee, J. L. Reno, and Q. Hu, *Broadband all-electronically tunable MEMS terahertz quantum cascade lasers*, Opt. Lett. **39**, 3480–3483 (2014).

[117] D. Turčinková, M. I. Amanti, G. Scalari, M. Beck, and J. Faist, *Electrically tunable terahertz quantum cascade lasers based on a two-sections interdigitated distributed feedback cavity*, Appl. Phys. Lett. **106**, 131107, 4 pages (2015).

[118] F. Castellano, V. Bianchi, L. Li, J. Zhu, A. Tredicucci, E. H. Linfield, A. G. Davies, and M. S. Vitiello, *Tuning a microcavity-coupled terahertz laser*, Appl. Phys. Lett. **107**, 261108, 5 pages (2015).

[119] M. Hempel, B. Röben, L. Schrottke, H.-W. Hübers, and H. T. Grahn, *Fast continuous tuning of terahertz quantum-cascade lasers by rear-facet illumination*, Appl. Phys. Lett. **108**, 191106, 5 pages (2016).

[120] P. Dean, M. Salih, S. P. Khanna, L. H. Li, N. K. Saat, A. Valavanis, A. Burnett, J. E. Cunningham, A. G. Davies, and E. H. Linfield, *Resonant-phonon depopulation terahertz quantum cascade lasers and their application in spectroscopic imaging*, Semicond. Sci. Technol. **27**, 094004, 9 pages (2012).

[121] A. Valavanis, S. Chowdhury, A. D. Burnett, A. R. Clarkson, D. R. Bacon, S. P. Khanna, A. G. Davies, E. H. Linfield, and P. Dean, *Diffuse-reflectance spectroscopy using a frequency-switchable terahertz quantum cascade laser*, IEEE Trans. Terahertz Sci. Technol. **6**, 341–347 (2016).

[122] D. Burghoff, T.-Y. Kao, N. Han, C. W. I. Chan, X. Cai, Y. Yang, D. J. Hayton, J.-R. Gao, J. L. Reno, and Q. Hu, *Terahertz laser frequency combs*, Nat. Photon. **8**, 462–467 (2014).

[123] M. Rösch, G. Scalari, M. Beck, and J. Faist, *Octave-spanning semiconductor laser*, Nat. Photon. **9**, 42–47 (2014).

[124] D. Burghoff, Y. Yang, and Q. Hu, *Computational multiheterodyne spectroscopy*, Sci. Adv. **2**, e1601227, 7 pages (2016).

[125] L. S. Rothman, I. E. Gordon, Y. Babikov, A. Barbe, D. C. Benner, P. Bernath, M. Birk, L. Bizzocchi, V. Boudon, L. R. Brown, A. Campargue, K. Chance, E. A. Cohen, L. H. Coudert, V. M. Devi, B. J. Drouin, A. Fayt, J.-M. Flaud, R. R. Gamache, J. J. Harrison, J.-M. Hartmann, C. Hill, J. T. Hodges, D. Jacquemart, A. Jolly, J. Lamouroux, R. J. L. Roy, G. Li, D. A. Long, O. M. Lyulin, C. J. Mackie, S. T. Massie, S. Mikhailenko, H. S. P. Müller, O. V. Naumenko, A. V. Nikitin, J. Orphal, V. Perevalov, A. Perrin, E. R. Polovtseva, C. Richard, M. A. H. Smith, E. Starikova, K. Sung, S. Tashkun, J. Tennyson, G. C. Toon, V. G. Tyuterev, and G. Wagner, *The HITRAN2012 molecular spectroscopic database*, J. Quant. Spectrosc. Radiat. Transfer **130**, 4–50 (2013).

[126] S. Kumar, B. S. Williams, Q. Qin, A. W. M. Lee, Q. Hu, and J. L. Reno, *Surface-emitting distributed feedback terahertz quantum-cascade lasers in metal-metal waveguides*, Opt. Express **15**, 113–128 (2007).

[127] H. Richter, M. Greiner-Bär, S. G. Pavlov, A. D. Semenov, M. Wienold, L. Schrottke, M. Giehler, R. Hey, H. T. Grahn, and H.-W. Hübers, *A compact, continuous-wave terahertz source based on a quantum-cascade laser and a miniature cryocooler*, Opt. Express **18**, 10177–10187 (2010).

Publications

- B. Röben, X. Lü, M. Hempel, K. Biermann, L. Schrottke, and H. T. Grahn, *Terahertz quantum-cascade lasers as high-power and wideband, gapless sources for spectroscopy*, Opt. Express **25**, 16282–16290 (2017).

- M. Hempel, B. Röben, M. Niehle, L. Schrottke, A. Trampert, and H. T. Grahn, *Continuous tuning of two-section, single-mode terahertz quantum-cascade lasers by fiber-coupled, near-infrared illumination*, AIP Adv. **7**, 055201, 6 pages (2017).

- B. Röben, M. Wienold, L. Schrottke, and H. Grahn, *Multiple lobes in the far-field distribution of terahertz quantum-cascade lasers due to self-interference*, AIP Adv. **6**, 065104, 6 pages (2016).

- M. Hempel, B. Röben, L. Schrottke, H.-W. Hübers, and H. T. Grahn, *Fast continuous tuning of terahertz quantum-cascade lasers by rear-facet illumination*, Appl. Phys. Lett. **108**, 191106, 5 pages (2016).

- M. Wienold, B. Röben, L. Schrottke, and H. T. Grahn, *Frequency comb operation of long-cavity terahertz quantum-cascade lasers*, Proc. SPIE **9767**, 97671A, 9 pages (2016).

- D. Rupp, L. Flückiger, M. Adolph, T. Gorkhover, M. Krikunova, J. P. Müller, M. Müller, T. Oelze, Y. Ovcharenko, B. Röben, M. Sauppe, S. Schorb, D. Wolter, R. Mitzner, M. Wöstmann, S. Roling, M. Harmand, R. Treusch, M. Arbeiter, T. Fennel, C. Bostedt, and T. Möller, *Recombination-enhanced surface expansion of clusters in intense soft x-ray laser pulses*, Phys. Rev. Lett. **117**, 153401, 6 pages (2016).

- M. Wienold, B. Röben, X. Lü, G. Rozas, L. Schrottke, K. Biermann, and H. T. Grahn, *Frequency dependence of the maximum operating temperature for quantum-cascade lasers up to 5.4 THz*, Appl. Phys. Lett. **107**, 202101, 4 pages (2015).

- M. Wienold, B. Röben, L. Schrottke, and H. Grahn, *Evidence for frequency comb emission from a Fabry-Pérot terahertz quantum-cascade laser*, Opt. Express **22**, 30410–30424 (2014).

- M. Wienold, B. Röben, L. Schrottke, R. Sharma, A. Tahraoui, K. Biermann, and H. Grahn, *High-temperature, continuous-wave operation of terahertz quantum-cascade lasers with metal-metal waveguides and third-order distributed feedback*, Opt. Express **22**, 3334–3348 (2014).

Acknowledgments/Danksagung

Zum Gelingen dieser Arbeit haben eine Reihe von Menschen beigetragen, denen ich hiermit meinen Dank aussprechen möchte. Zunächst möchte ich mich bei Prof. H. Riechert und Prof. H. T. Grahn bedanken, die mir die Möglichkeit gegeben haben, am Paul-Drude-Institut zu forschen und meine Doktorarbeit anzufertigen. Besonderer Dank gebührt Prof. H. T. Grahn für die praktische Betreuung meiner Doktorarbeit. Ebenfalls danke ich Prof. U. Woggon für die Bereitschaft, meine Doktorarbeit als Betreuerin an der Technischen Universität Berlin zu begleiten. Ebenso danke ich Prof. M. Helm für die Auskünfte zum Freie-Elektronen-Laser *FELBE*.

Großer Dank gebührt den aktuellen und vormaligen Mitgliedern der Core Research Area *Intersubband emitters* für die Unterstützung, die angenehme Arbeitsatmosphäre und die fruchtbaren Diskussionen. Besonders möchte ich Dr. L. Schrottke für die Hilfestellungen in der Abschlussphase meiner Doktorarbeit danken. Bei Dr. X. Lü, Dr. M. Hempel, Dr. M. Wienold und Dr. G. Rozas möchte ich mich für die Zusammenarbeit im Labor und die vielseitigen Diskussionen bedanken. Die in dieser Arbeit vorgestellten Proben basieren auf der herausragenden Vorarbeit von Prof. H. T. Grahn, Dr. L. Schrottke, Dr. X. Lü und Dr. K. Biermann, ohne die die in dieser Arbeit verwendeten THz QCLs nicht existieren würden. Ferner möchte ich Dr. A. Tahraoui für fruchtbare Diskussionen danken.

Die nicht-wissenschaftlichen Mitarbeiter am Paul-Drude-Institut haben ebenfalls zum Gelingen dieser Arbeit beigetragen. Zunächst möchte ich mich bei S. Krauß und M. Matzeck für ihre große Unterstützung in Bezug auf das mechanische Polieren bedanken. W. Anders danke ich für die Prozessierung und A. Riedel für die Unterstützung beim Aufbau und beim Bonden der Proben. Nicht zuletzt gebührt mein Dank auch F. Henschke, M. Sieg, T.-M. Ferber und J. Pfeiffer aus der Werkstatt. Bedanken möchte ich mich auch bei D. Dormeyer und S. Räther für die Beschaffung von Literatur. Schließlich möchte ich noch A. Hartung für die exzellente administrative Betreuung danken.

Für das Korrekturlesen danke ich Prof. H. T. Grahn, Dr. L. Schrottke, Dr. X. Lü und Dr. M. Hempel.

Meinen Eltern möchte ich für die unermüdliche Unterstützung in schwierigen Zeiten danken.